Development of a clinical head and neck hyperthermia applicator

Maarten Paulides

Development of a Clinical Head and Neck Hyperthermia Applicator

Maarten Paulides

The cover picture beautifully illustrates the complexity of interfering waves, as will also occur during hyperthermia treatments with microwaves. The small figure is an impression of the developed head and neck applicator.

Development of a Clinical Head and Neck Hyperthermia Applicator

Ontwikkeling van een klinische hoofd-hals hyperthermie applicator

Proefschrift

ter verkrijging van de graad van doctor
aan de Erasmus Universiteit Rotterdam
op gezag van de rector magnificus

Prof.dr. S.W.J. Lamberts

en volgens besluit van het College voor Promoties.

De openbare verdediging zal plaatsvinden op
donderdag 18 oktober 2007 om 13.30 uur

door

Margarethus Marius Paulides

geboren te Waalwijk

ERASMUS UNIVERSITEIT ROTTERDAM

Promotiecommissie

Promotoren:	Prof.dr. P.C. Levendag
	Prof.dr. ir. A.P.M. Zwamborn
Overige leden:	Prof.dr. B.J.M. Heijmen
	Prof.dr. P.M.T. Pattynama
	Prof.dr. A.G. Tijhuis
Copromotor:	Dr.ing. G.C. van Rhoon

Address for correspondence:
M.M. Paulides, Department of Radiation Oncology: Unit Hyperthermia, Erasmus MC - Daniel den Hoed Cancer Center, PO box 5201, 3008AE Rotterdam, The Netherlands. (m.paulides@erasmusmc.nl)

"Kleine lichtpuntjes op een slechte dag, zijn dat knipoogjes van God?"
(Visje)

aan Petra

en beide families

Contents

CHAPTER 1

Introduction

1.1 Background

Worldwide, around 3-5% of patients suffering from cancer have tumours in the head and neck (H&N) region[58,65,66]. By definition, the term "head and neck cancers" usually excludes tumours that occur in the eyes, in brain and in skin. The most frequently occurring cancers of the head and neck area are located in the oral cavity and the larynx.
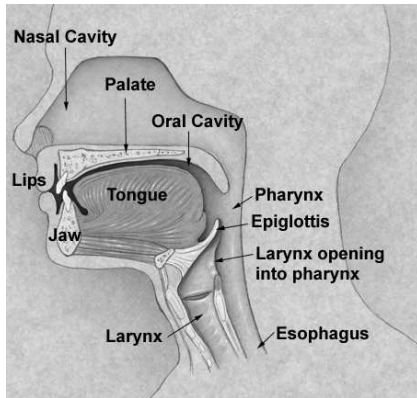
The H&N region is often divided in five regions, each containing different tumour sites:

1. Oral cavity

2. Nasopharynx (area behind the nose)

3. Oropharynx

4. Hypopharynx (bottom part of the throat)

5. Larynx (voice box)

Figure 1.1: Indication of the different regions in the head and neck region.

In the H&N region, treatment of advanced tumours remains complex[12] and loco-regional control poses a major therapeutic challenge[20,79]. The currently standard radiochemotherapy (RCT) generally results in a 5-year survival rate of 20% to 65%[12]. Furthermore, the toxicity related to the RCT treatment remains a major issue[90]. Often occurring early and late side effects are loss of swallowing function and xerostomia (loss of salivary function) leading to difficulties in speaking and eating. Therefore, a considerable effort is directed to improving treatment outcome while minimizing toxicity: some examples of those are described in Section 2.1. Addition of hyperthermia (HT) to current treatment modalities may contribute to the loco-regional control of the tumours and generally the heat treatment has no contribution to the toxicity of the treatment[98].

1.2 Hyperthermia treatment

In a HT treatment, energy is transferred into the patient to accomplish a therapeutic result. In the Erasmus MC - Daniel den Hoed Cancer Center, HT is being applied by inducing tumour temperatures between 40-44°C for 30-60 minutes or longer[98]. Several Phase III trials[10,44,99] have demonstrated the efficacy of the addition of a HT treatment to either radiotherapy (RT) or chemotherapy (ChT) in terms of local tumour control and/or survival rates. Further, these studies showed no clinically relevant extra HT toxicity and, moreover, no enhancement of RT or ChT toxicity: a unique feature of a cancer treatment. The biological rationale for HT, however, is

still not very well established[18,47]. Direct cell kill is not very likely at the 'mild' temperatures that are generally obtained in the clinic during hyperthermia treatments (39-42°C)[18]. Research nowadays focusses, amongst many others, on the effects of HT on tumour oxygenation and vascular damage.

1.2.1 Hyperthermia applicators

Hyperthermia can be applied by whole-body, external or interstitial/intracavitary techniques[87]. External HT applicators use ultrasound (US) or electromagnetic (EM) waves to direct energy to the target region. US provides similar heating options as EM but results in more bone-pain complaints during treatment[6]. For EM-based deep hyperthermia (DHT) there are both commercial and non-commercial devices whereas most devices for superficial HT (SHT) are developed in-house.

Applicators at the Daniel den Hoed Cancer Center

The HT treatment is divided in whole-body, deep-regional and superficial HT[87]. The threshold between deep and superficial HT is commonly considered to be at 4 cm maximum depth of the treatment area. In the Daniel den Hoed Cancer Center, the commercial BSD2000 Sigma-60 and Sigma-eye applicators (BSD Medical, USA) are used for DHT treatments in the pelvic region, and the in-house developed Lucite cone applicator (LCA)-system is used for superficial treatments.

BSD2000 system   LCA system

Figure 1.2: Clinical applicators that are used within the hyperthermia unit.

Treatment planning

In some institutes, DHT treatments are preceded by patient-specific treatment planning. However, treatment planning programs are used more commonly to investigate novel applicator designs or general treatment changes to improve the heat delivery[51].

The first step of HT treatment planning is the generation of a segmentation (patient model) from computerized tomography (CT) or magnetic resonance imaging (MRI) scans. A model of the applicator and this segmentation are used to calculate the power absorption (PA, $[W/m^3]$) or specific absorption rate (SAR, $[W/kg]$) distribution in the patient by EM models. These EM models for treatment planning are commonly based on the finite-element (FE) method or finite-difference time-domain (FDTD) method. A temperature distribution in the patient can be calculated from the power absorption distribution by applying Pennes' bio-heat equation (PBHE[78]), or more elaborate algorithms including the (blood) vessel network, i.e. discrete vasculature (DIVA) models, down to vessel sizes in the millimeter range[51,67]. The main problems with these thermal methods are long time-requirements for the generation of a vessel network and the large, poorly-predictable, variations in thermal properties of tissues. Therefore, for applicator comparisons, developments and quality assurance (QA) purposes, normally PA or SAR distributions are used.

1.2.2   Head and neck hyperthermia

A significant benefit of the addition of a HT treatment for superficially located tumours or metastatic lymph nodes in the H&N region has been reported in literature. Valdagni *et al.*[94,95] demonstrated that with a non-specific HT-applicator already a significant increase in local control (from 24% for RT alone versus 69% for RT plus HT) is achieved for metastatic lymph nodes, without additional toxicity. In a Phase I/II study, Amichetti *et al.*[2] showed improved treatment outcome also for HT in addition to a hyperfractionated radiation schedule and no increase of the toxicity.

In our opinion, a major cause of the loss of interest in the combined treatment of RT+HT for advanced H&N tumours lymph nodes has been the lack of an appropriate HT system to adequately heat these tumours. Further, the use of a specific designed HT applicator consisting of an array of electromagnetic (EM) antenna elements is expected to result in large improvements in the quality of heating arbitrarily-shaped target regions in the H&N region[107].

The head and neck region is characterized by many tissue transitions, small in diameter structures and large cooling vessels (Figure 1.3). Applying an adequate thermal dose to target areas in the entire head and neck region therefore is a challenging task since the anatomy can have a major influence on the power absorption pattern. Further, highly thermo-sensitive tissues are present within the treatment region (myelum = spinal column) or very nearby (brains) and hence there exist a relevant risk of thermally related toxicity[34]. Hyperthermia must therefore be applied with equipment that enables sufficient resolution and degrees of freedom (DOF) to be able to shape the power absorption pattern such that only a limited amount of power is absorbed in myelum and brains during treatment while sufficient power is absorbed in the target region.
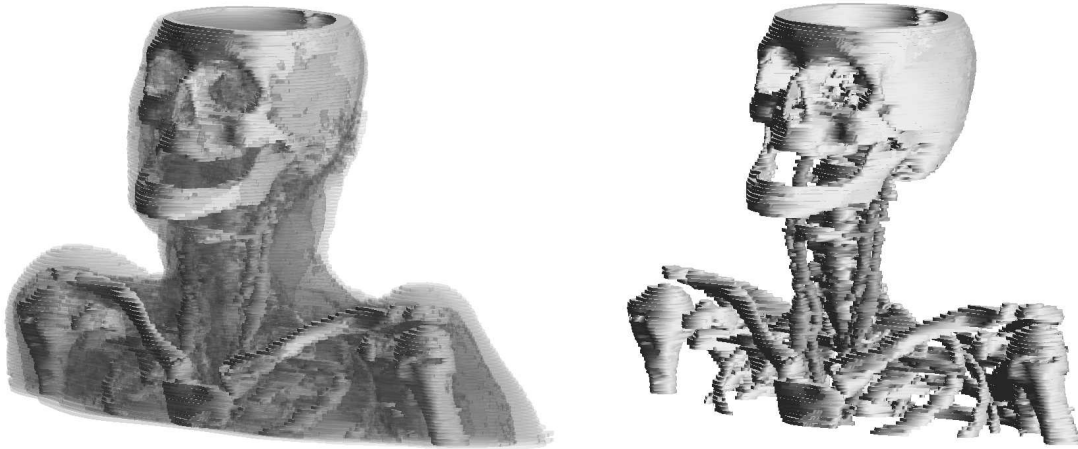
Figure 1.3: Semi-transparent solid model visualization of an example Larynx patient segmentation in the treatment planning program. These figures show that many bony structures (light gray) and many large vessels (darker gray) are present in the head and neck region.

Earlier work on head and neck applicators

Up to now, the application of HT in the H&N region was limited to superficial regions because of the lack of deep-heating equipment for this region. For superficial H&N tumours, already in the 80's, phased-array approaches to apply superficial hyperthermia with EM antennas with planar or conformal arrays were investigated[45,56]. For deeper locations, theoretical work[41] and laboratory measurements[29,30] were conducted to investigate the feasibility of a multi-antenna phased array for heating a neck-mimicking cylinder. However, all preliminary work has never led to a clinical prototype.

1.3 The Dutch Cancer Society project

In 2003, we started the development of the H&N HT applicator. In this project, the general idea was to exploit the latest progress in EM modeling to design the optimum applicator by using simulation studies. The project further included the development of a high-power amplifier system with power and phase control. The requirements for the applicator were defined as follows.

SAR distribution:

- The applicator must have the flexibility to heat advanced lateralized tumours and/or tumours located at the center of the H&N region.

- The hyperthermia field widely covers the macroscopic tumour, e.g. with a minimum margin of 1 cm overlap. The hyperthermia field is defined as the area enclosed by at least the 25% iso-SAR contour[54].

- The applicator should allow SAR pattern adjustment such that no heating of critical organs (myelum, cartilage) above the tolerance limits occurs.

- The SAR distribution can be controlled in both the radial (dorsal-ventral and left-right) and axial (patient-axis: cranial-caudal) direction.

Technology:

- The applicator has the ability to conform to the tissue contour with minimal discomfort to the patient.

- The water bolus and antennas are integrated in a single mechanical construction rendering easy positioning of the applicator around the target area.

- The applicator set-up can be positioned with a reproducibility better than 1 cm in any direction.

- Building the applicator set-up should be simple and fast.

- The applicator has excellent reliability under clinical conditions, e.g. it can operate for long periods at high RF-power outputs and requires only limited time for preventive and scheduled maintenance service.

1.3.1   Approach

The project was started by carrying out a feasibility study into deep heating in the neck with a good control of the SAR pattern. SAR control is highly frequency dependent and requires sufficient resolution (high frequency) but also sufficient penetration of the EM waves (low frequency). Therefore, as a first step we determined the optimum trade-off frequency. Good SAR control is further determined by the amount of DOF (phases and amplitudes), i.e. the number of antennas. Therefore, in subsequent steps we analyzed the required number of antennas and their positioning. These parameter studies were performed by using the most simple antenna, i.e. a dipole. To improve the robustness and predictability of the applicator set-up, we specifically designed a patch antenna to replace the dipoles. Simultaneously, we established that calculated or measured SAR patterns in a simple model are predictive for the SAR pattern in the neck. This simple cylindrical model was then used

to verify the predicted SAR patterns by phantom measurements. As a last step, all parameters were used as input to design a clinical prototype of the applicator: the HYPERcollar.

Simulation of harmonic signals with FDTD

For this project we chose to use the FDTD method for all EM calculations because it: 1) is suited for simulating highly non-homogeneous models, 2) scales well with the resolution increase 3) implicitly incorporates coupling between patient and antennas and 4) can be implemented efficiently in hardware accelerators. The FDTD method is described extensively in[89] and its use for hyperthermia purposes is discussed in[11,38]. The FDTD technique is a time domain technique. An item that is poorly addressed for FDTD is the definition of steady-state for harmonic signals[38]. For harmonic signals (433 MHz), we will assess steady-state by placing voltage sensors at the gap of each antenna and centrally in the domain. Steady-state will be assumed when the difference in maximum value of multiple subsequent periods has decreased to a few percent. For simplicity we will use the dielectric properties pertaining to the operation frequency of 433 MHz for all frequencies that are present in the excitation signal. Using Fourier analysis, we established that a time-harmonic sinusoidal signal, modulated by a one-period ramp, exhibits only a small frequency band (-10dB bandwidth ¡ 100 MHz). This ramp further prevents dc signals to be generated[23] and the FDTD algorithm works as a filter for high frequencies[89]. In addition, the signal is used to excite antennas that work as a good frequency filter. Considering the above mentioned, we have chosen to use FDTD as a designer tool to fast and accurately calculate the EM distributions. Improvements on the algorithm itself are not considered and outside the scope of the research. The validity of our choice is supported by measurements in which the predictive value of the simulations for our application has been shown.

1.4   Outline of this thesis

Chapter 2 contains the results of a theoretical analysis into the feasibility of focussed heating in the head and neck region by a circumferential array of antennas. The analysis was performed by using an electromagnetic solver and a realistic patient model. Parameters of interest in this investigation were antenna positions, number of antennas and operating frequency.

Chapter 3 is dedicated to the distortions on the local SAR distribution of the theoretical set-up (chapter 2) by various major anatomical structures in the neck. The influence on the SAR pattern of major structures was assessed by high resolution 3D FDTD calculations. In this work, the neck was approximated by a semi-3D generic phantom based on average dimensions obtained from CT-derived human data.

Chapter 4 describes the work to converge from the theoretical set-up, as found in chapter 2, towards an actual multi-antenna-ring configuration for the clinical applicator.

Chapter 5 is dedicated to a specifically designed patch antenna and its development process. Further, theoretical work into its behavior under clinical conditions is reported. Finally, the accuracy of the FDTD model is assessed by measurements using an approximated array set-up.

Chapter 6 describes the measurements that were conducted using a cylindrical muscle phantom (chapter 3) and a laboratory prototype consisting of patch antennas (chapter 5) in the optimum arrangement (chapter 4). By these measurements we determined the minimum focus size, the SAR pattern steering possibilities of the set-up and verified the SAR pattern predictions.

Chapter 7 shows the final, clinical, head and neck applicator prototype and all its features. Further, the corresponding treatment planning is explained and its potential shown using an example larynx patient model.

Chapter 8 reports on the session that was applied to the first patient of the clinical feasibility study. In this chapter we present the results of treatment planning, the HT session and the measured temperatures.

Chapter 9 finalizes the scientific content by providing the general conclusions and future perspectives.

CHAPTER 2

Optimization of frequency and sources for a single antenna ring

Abstract

Purpose: *Investigation of the ability to deposit radiofrequency (RF) energy centrally in the neck as a function of antenna positions, number of antennas and operating frequency.* **Materials and methods:** *Power absorption (PA) distributions in a realistic model of the head and neck anatomy are calculated, where the head model is irradiated by an array of dipole antennas. The relative PA distributions corresponding to different set-ups are visualized and analyzed using the ratio of the average PA (aPA) in the target and neck region.* **Results:** *Both the PA distributions and aPA ratios indicate an optimal focussing ability of the set-ups, i.e. the ability to direct energy efficiently into the target region, between 400 and 600 MHz. In this frequency band the focussing ability depends only moderately on the size of the neck. Finally it is found that the focussing ability at 433 MHz is increased significantly by increasing the number of antenna elements.* **Conclusions:** *The optimal frequency is found to be highly dependent on the size of the target volume; thus a single optimum is hard to define. However, future clinical research will focus on 433 MHz based upon the optimal range of frequencies, as found in this study.*

2.1 Introduction

Patients with advanced carcinomas in the head and neck (H&N) have a dismal prognosis. Loco-regional control still poses a major therapeutic challenge. For tumours considered to be unresectable, the traditional treatment has been conventional fractionated radiotherapy (RT) resulting in low 2-year survival rates (30%) for stage III/IV disease[57,60]. Introducing hyperfractionation and/or accelerated radiation treatment schedules have substantially improved the poor treatment outcome[19,37,97]. Similarly, by combining RT with simultaneous chemotherapy an 8% increase of overall 2-year survival was reported in the three meta-analyzes study of Pignon *et al.*[79]. Unfortunately, the improved treatment outcome is at the cost of increased toxicity[90], in particular of the mucosal linings[20], where for older patients this treatment is even too toxic. Consensus exists that the optimal strategy for treatment of advanced unresectable H&N carcinomas remains to be defined and that the identification of a combined modality treatment with equal or better treatment outcome but with a lower toxicity is of high priority.

New strategies currently under investigation, like ARCON, hypoxic cell sensitizers and angiogenesis, focus on killing the radioresistant, hypoxic tumour cell population[7]. Some of these approaches have shown improved treatment outcome but have not gained general acceptance. The unique feature of HT is that it enhances local tumour control but it does not increase radiation toxicity[98]. From the perspective of the focus on the radioresistant hypoxic cell population it is disappointing that

the potential of hyperthermia (HT) to greatly enhance the local control (from 24% for RT alone to 69% for RT + HT) and survival rate (from 0% for RT alone to 50% for RT + HT) for metastatic lymph nodes in Stage IV carcinoma of the H&N without additional toxicity, as was demonstrated in a phase III study by Valdagni *et al.*[94,95], has not been further explored. In 1997 Amichetti *et al.*[2] showed that HT also improves treatment outcome when added to a hyperfractionated radiation schedule, but does not increase toxicity.

In our opinion a major cause of the loss of interest in the combined treatment of RT+HT for advanced H&N tumours has been the lack of a good HT system to adequately heat tumours at this location. HT treatment of H&N tumours involves the heating of tumour tissue extending from the surface to as deep as the center of the neck, e.g. depths from 0 to 7 cm. From our own clinical experience (unpublished data) we know that in general cervical lymph nodes can be heated relatively easy with electromagnetic (EM)-energy, but that it is much more difficult to adequately heat the more deeper located tumours. The latter is confirmed by the experiences of other HT groups. Serin *et al.*[85] reported adequate ability to heat superficial metastatic cervical lymph nodes using a commercial ultrasound (US) system, though nodal volume and depth influence the quality of the heating. Wust *et al.*[107] and Ben-Yosef and Kapp[6] compared the performance of heating of more deeply located H&N tumours, e.g. surrounded by bone and air, using EM or US technology. They reported that HT applied by US was limited by bone pain and showed inferior temperature distributions in comparison to heat applied by single EM applicator systems. Wust *et al.*[107] anticipate that the use of a specific designed HT applicator consisting of an array of EM antenna elements will result in large improvements in the quality of heating advanced H&N tumours.

Overall, the great potential of combined RT+HT for the treatment of advanced H&N tumours in combination with the significant progress in radiofrequency (RF) applicator technology as well as in EM modeling, is a strong stimulant for us to start the development of a site-specific EM applicator system for HT treatment of H&N tumours. In this paper we report on the results of a theoretical study into the feasibility of such an applicator system where the focus is on the arrangement of antenna elements and the optimal frequency for heating tumours located in the neck region. An important criterion for the frequency selection is our demand that the applicator must have the flexibility to heat both advanced laterally located tumours and tumours located at the midline of the H&N region. Hence, the power absorption (PA) distribution must be controlled in both the axial and radial direction for which amplitude and phase steering is essential. Axial PA control requires multiple antenna rings whereas control of the radial PA distribution is obtained by placing multiple antennas in a circular array configuration. The ability to obtain a high PA at the center of the neck will be the most challenging and difficult problem to solve because penetration depth is strongly frequency dependent[56]. Therefore, in this study, we have focussed on investigating the dependence of the PA at the center of the neck as the complex function of number of EM-sources in one ring and frequency.
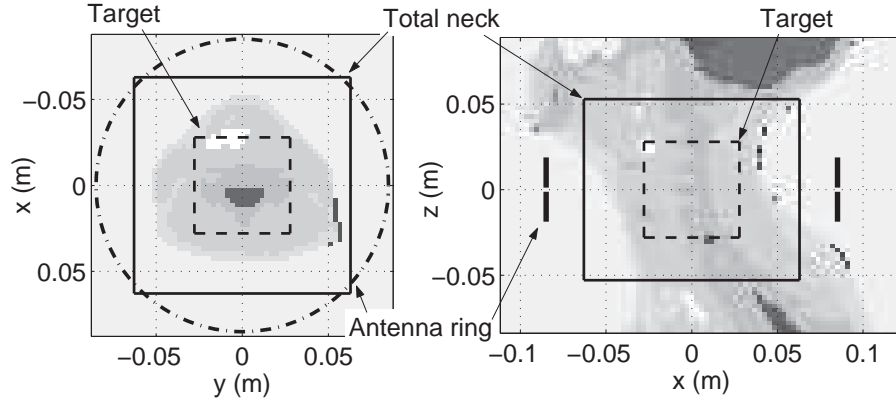
Figure 2.1: Tissue distribution in the neck and positioning of the antennas around the neck at cross-sections through (a) $z = 0$ mm and (b) $y = 14$ mm. The tissue type index (tti) values correspond with those in Table 2.1.

2.2 Materials and methods

Investigation of all parameters and their combined effects requires a huge amount of calculations. Therefore, this numerical investigation is split into three series of calculations. The first series of calculations addresses the influence of the placement and number of antennas for a rough selection of frequencies using one patient. The parameter under investigation for the second series of calculations is the operating frequency while using the number of antenna elements that offers a good discrimination between the results obtained at these frequencies. A single optimal frequency is will be hard to find since the absorbed power is to a large extent dependent on the size of the area that should be treated. Hence, in addition to the frequency investigation for a target volume of 5x5x5 cm we also varied the target size in the analysis. Finally, for the last (third) series of calculations, we scaled the patient anatomy obtaining three set-ups: a small, average (1.24x) and large (1.39x) anatomy, where the diameter of the neck is 9.7, 12 and 13.5 cm, respectively. For these configurations a constant number of antennas is used (eight) and a constant antenna-tissue distance is applied. This part is mainly dedicated to the need for a high penetration depth and focuses on frequencies within the frequencyband, as selected from the second series of calculations.

2.2.1 Anatomy model

The entire volume is divided into a finite number of volume elements, e.g. voxels, for use in numerical calculations with a computer program. Assigning tissues to these voxels results in a head segmentation.

For the first step of the head segmentation process we used a CT-scan of a H&N RT

patient consisting of 69 transverse 2-D CT-slices. A 3-D model of the head and neck region is constructed automatically from these 2-D slices by a dedicated computer program. In this model, four different regions of Hounsfield values are defined and labelled automatically, which leads to a rough head segmentation. Subsequently, organs are assigned manually. For the analysis we introduce a hypothetical target volume with realistic content in the model at the central neck location.

The head model is truncated at the level of the shoulders and nose and no matching at the transition to the water is applied because it is assumed that the distance to the area of interest was sufficient to suppress the influences of reflections. Each voxel measures 2.83, 2.83, 2.50 mm in dimension (x, y and z-axis), where the geometrical dimensions of the head model are 234, 424 and 173 mm, respectively. The diameter of the neck of this particular example patient is found to be relatively small[73] i.e. 9.7 cm. The influence of larger necks is investigated by using two scaled versions of this H&N model. Scaling was carried out to obtain H&N models with neck diameter of 12.0 and 13.5 cm, respectively. Note that this scaling implies multiplication of the voxel sizes with an equal scalar in all Cartesian directions.

Figure 2.1 shows transversal and sagittal cross-sections of the tissue distribution in the model, where the tissue coding is according to Table 2.1. The cross-sections through $z = 0$ mm and $y = 14$ mm have been chosen to visualize the results avoiding inclusion of the trachea where the PA results will be equal to zero since the trachea is a non-conducting material. Note that the single dark spots at the edges of the anatomy represent wet skin (11) and not perfectly electric conducting (PEC) material.

2.2.2 Applicator model

The use of dipole antennas within a clinical environment is common. Consequently, dipoles are used as radiating elements in our study. Calculations are carried out with one, four, six, eight or 16 dipole antennas embedded in de-ionized water. Equal spacings between the antennas are used since according to Henke *et al.*[35] a symmetrical array performs best for a symmetrical set-up, which is approximately the case for the neck region. The operating frequency is chosen from the interval of 100 to 915 MHz which includes the entire region indicated for this site[41], i.e. between 100 and 750 MHz, and the closest ISM* frequencies. The dipole antennas are equally-spaced positioned on a, 170 mm in diameter, circle that surrounds the neck ("Antenna ring": Figure 2.1). The diameter of the antenna ring is increased for the scaled model in order to keep a constant distance between the antennas and the skin of the patient for all set-ups, i.e. the diameters for these set-ups are 193 and 208 mm. The sources are of equal phase and amplitude since this is expected to result in positive interference in the central region. Phase and amplitude optimization has

---

*ISM frequencies: these are frequencies allocated for applications in Industry, Science and Medicine. In most European countries they are: 27.12, 433 and 2450 MHz. In the USA 433 MHz is replaced by 915 MHz.

Table 2.1: Dielectric properties of the tissue types at 100, 433 and 915 MHz (μ_r = 1.0).

Tissue type (index)	100 MHz		433 MHz		915 MHz	
	ϵ_r [-]	σ [S/m]	ϵ_r [-]	σ [S/m]	ϵ_r [-]	σ [S/m]
0. De-ionised water	78	$2*10^{-3}$	78	0.04	78	0.18
1. Trachea	10	0.00	1	0.00	1	0.00
2. Fat	6	0.04	6	0.04	6	0.05
3. Muscle	66	0.71	57	0.81	55	0.95
4. BoneCortical	15	0.06	13	0.09	12	0.15
5. Air bubble	1	0.00	1	0.00	1	0.00
6. Lung	1	0.00	1	0.00	1	0.00
7. Tooth	15	0.06	13	0.09	12	0.15
8. Cartilage	56	0.48	45	0.60	43	0.79
9. BrainGrey matter	80	0.56	57	0.75	53	0.95
10. BrainWhite matter	57	0.32	42	0.45	39	0.60
11. SkinWet	66	0.52	46	0.68	46	0.85
12. Gland	69	0.80	61	0.89	60	1.04
13. PEC	1	$1*10^6$	1	$1*10^6$	1	$1*10^6$

been omitted in the entire study. The length of the dipole antennas (L_{dip}) is chosen such that they are resonant or smaller since this provides equal radiation patterns[5], i.e. 3.75 cm for low frequencies ($f = 433$ MHz) and 1.75 cm for higher frequencies ($f > 433$ MHz) are used. An infinite de-ionized water environment with a relative permittivity of 78.0 is used as waterbolus since the influences of a waterbolus are not subject of this study.

2.2.3   Electromagnetic modelling

A finite-difference time-domain (FDTD) based program[†9] is used to calculate the PA distributions. The FDTD algorithm is widely used and described extensively, e.g. by Taflove[89]. The algorithm calculates the electric (E) and magnetic (H) fields in a discrete space and time frame. The PA value in a certain voxel is obtained from the electric field components at every point:

$$\text{PA} = \frac{\sigma_{eff}|\vec{E}|^2}{2} \ (Wm^{-3}) \tag{2.1}$$

where σ_{eff} is the effective conductivity (S/m). Note that the PA values differ only by the tissue-dependent mass density from the specific absorption rate (SAR) values. As main inputs, the program requires the head model and an applicator model.

[†]FDTD program developed at TNO-FEL, The Hague, The Netherlands.

Mur's second-order absorbing-boundary conditions (ABC)[62] are applied to terminate the borders of the entire computational domain. A uniform rectilinear mesh is used and additional voxels between the head model and ABC are applied to reduce the influence of reflections at the ABC's. For high frequencies ($f \geq 433$ MHz) the computational domain consists of 163, 170 and 89 voxels (= 2.5 million voxels) in the x, y and z-direction respectively, where the dimensions of a voxel are 2.9, 2.9 and 2.5 mm. For low frequencies ($f < 433$ MHz) the domain is extended with 10 voxels in all directions since the penetration depth in water is higher at these frequencies. The dielectric properties of the tissues per frequency are found using an application of IFAC-CNR[69] based on a parametric model by Gabriel *et al.*[26]. As an example the dielectric properties at 100, 433 and 915 MHz are given in Table 1, where isotropic tissues are assumed. The dielectric properties of the trachea and lung are chosen equal to those of air since from the results of Gabriel it was not clear whether the entire lung and trachea were considered or just the organ walls. The properties of de-ionized water (salinity = 0.00 g/l, T = 20°C) and PEC are assumed to be dispersion-free. The dipoles of the applicator are approximated by so called "hard sources"[89], i.e. electric-field point sources, that excite two conducting wires (PEC material, Table 2.1) with a cross-section of 2.89 x 2.89 mm2.

2.2.4 Evaluation

The evaluation of the PA distributions is carried out qualitatively by comparing visualizations of cross-sections trough the PA distribution at $z = 0$ mm and $y = 14$ mm. The distributions are normalized to the average PA value in the neck region ($\text{PA}_{\text{neck volume}}$): $\text{PA}_{\text{norm}}(x,y,z) = \text{PA}(x,y,z)/\text{PA}_{\text{neck volume}}$. Visualization of the PA distribution by color plots is strongly influenced by the choice of the normalization method. This makes it difficult to evaluate the treatment quality from these visualizations alone. As our aim was to assess the ability of a set-up to direct power to the central target region we selected the average power absorption ratio to quantify the relative amount of energy that is absorbed in the target region. It is defined as:

$$\text{aPA ratio} = \frac{\sum_{\text{target volume}} \frac{\text{PA}_{(x,y,z)}}{N_{\text{target volume}}}}{\sum_{\text{neck volume}} \frac{\text{PA}_{(x,y,z)}}{N_{\text{neck volume}}}}$$

where $N_{\text{neck volume}}$ and $N_{\text{target volume}}$ are the total amount of tissue voxels in the neck and target volume, respectively. This ratio is found to depend little on the size of the neck volume but to a large amount on the dimensions of the target volume. The neck volume is defined as the tissue voxels within a 12x12x10 cm brick volume (Figure 2.1). We chose to use a target volume of 5x5x5 cm because the aim is to treat advanced tumours. However, since the aPA ratio is highly dependent on the target size, other target volume dimensions are shown as well. The target volume dimensions range from 2x2x2 cm (8 cm^3) to 8x8x8 cm (512 cm^3) since the aim is on

treating all from a primary tumour up to a combination of a large primary tumour and/or its lymph node metastases.

2.3 Results

2.3.1 Positioning and optimal number of dipoles in a single antenna ring

The first series of calculations are carried out using 1, 4, 6, 8 and 16 antennas at 100, 433 and 915 MHz. Concerning the positioning of applicator sources it is found that the PA distributions are influenced adversely by a region of high PA at the chin, due to the local irregular tissue distribution. Therefore, all set-ups are rotated such that the antenna-chin distance is as large as possible to circumvent this problem, e.g. for eight antennas a 22.5° rotation is applied with respect to the 0° position in front of the chin (Figure 2.2a-c).
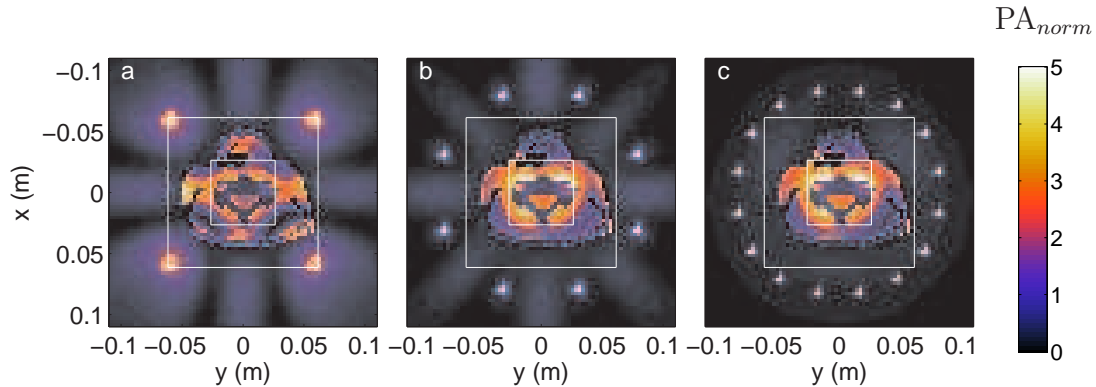
Figure 2.2: PA distributions in the neck at cross-sections through $z = 0$ resulting from FDTD calculations with 433 MHz for a) 4, b) 8 and c) 16 dipole antennas. The PA values are normalized to the average value in the neck volume. The target and neck volume are indicated by the white squares.

Figure 2.2 shows the normalized PA distributions for four, eight and sixteen dipoles around the neck at a cross-section through the sources of the dipoles. The positions of the dipoles are visible by the white spots indicating local very high PA values due to a high imposed electric field. The central target region and neck region are indicated by the white squares. Figure 2.2a shows that the interference pattern at 433 MHz of four dipoles does not fulfill the requirements to direct the energy specifically to the central region. A much more pronounced focal area, i.e. a region of high PA, is obtained when using eight (Figure 2.2b) or sixteen sources (Figure 2.2c), where little difference is visible between eight and sixteen dipoles. Figure 2.3 shows the aPA ratio results at 100, 433 and 915 MHz for the various set-ups with different number
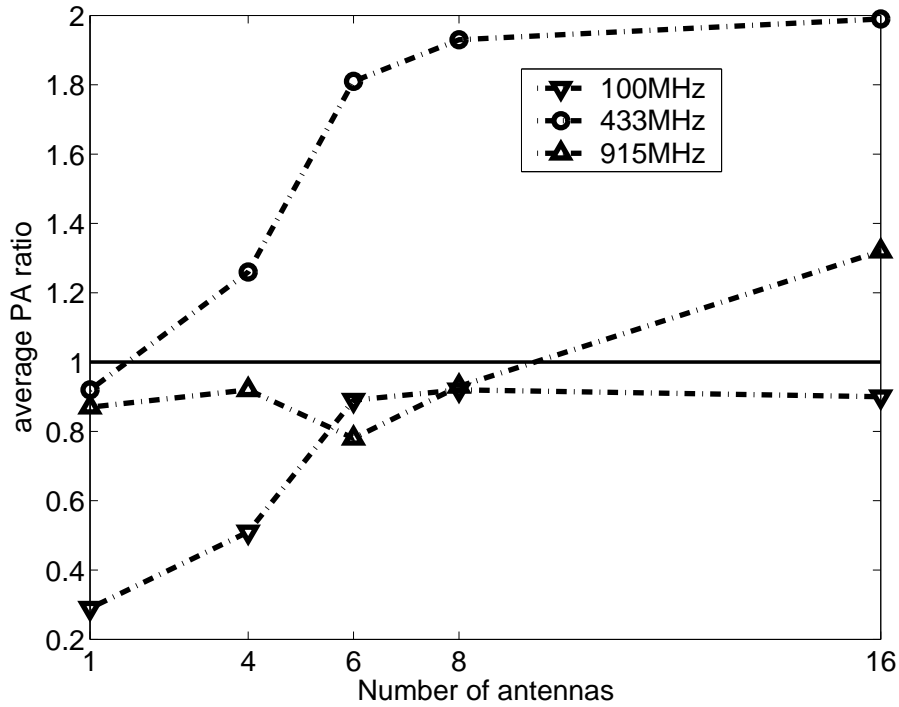
Figure 2.3: aPA ratio values as a function of number of sources for 100 MHz, 433 MHz and 915 MHz. The target volume is 5x5x5 cm and the neck volume 12x12x12 cm.

of radiating elements. It is found that the highest aPA ratio values are obtained using 433 MHz with sixteen dipoles but the plateau starts roughly at eight dipoles. The curves corresponding to 100 and 433 MHz show a similar behavior. The curve belonging to 915 MHz, however, shows a decreased aPA ratio for six antennas. This is the result of secondary foci (foci other than the central focus) that are present in the tissue at this frequency. Based on these results we chose to use eight dipoles since this number of antennas provides the best compromise between the constraint to use as few antennas as possible and best performance in terms of aPA ratio.

2.3.2 Optimum operating frequency

The second series of PA predictions is performed to study the influence of the frequency on the ability to heat centrally located target volumes of various sizes. Figure 2.4 shows the PA distributions for all frequencies under consideration using an eight dipole configuration. It is observed that low frequencies (100 MHz and 144 MHz) result in superficial absorption only, whereas the antenna set-up performs insufficient at high frequencies (700 MHz and 915 MHz) due to secondary in tissue. Multiple foci in the surroundings, besides in the target volume, lead to unwanted high superficial PA. Also, the high frequencies lead to high PA values in the sur-
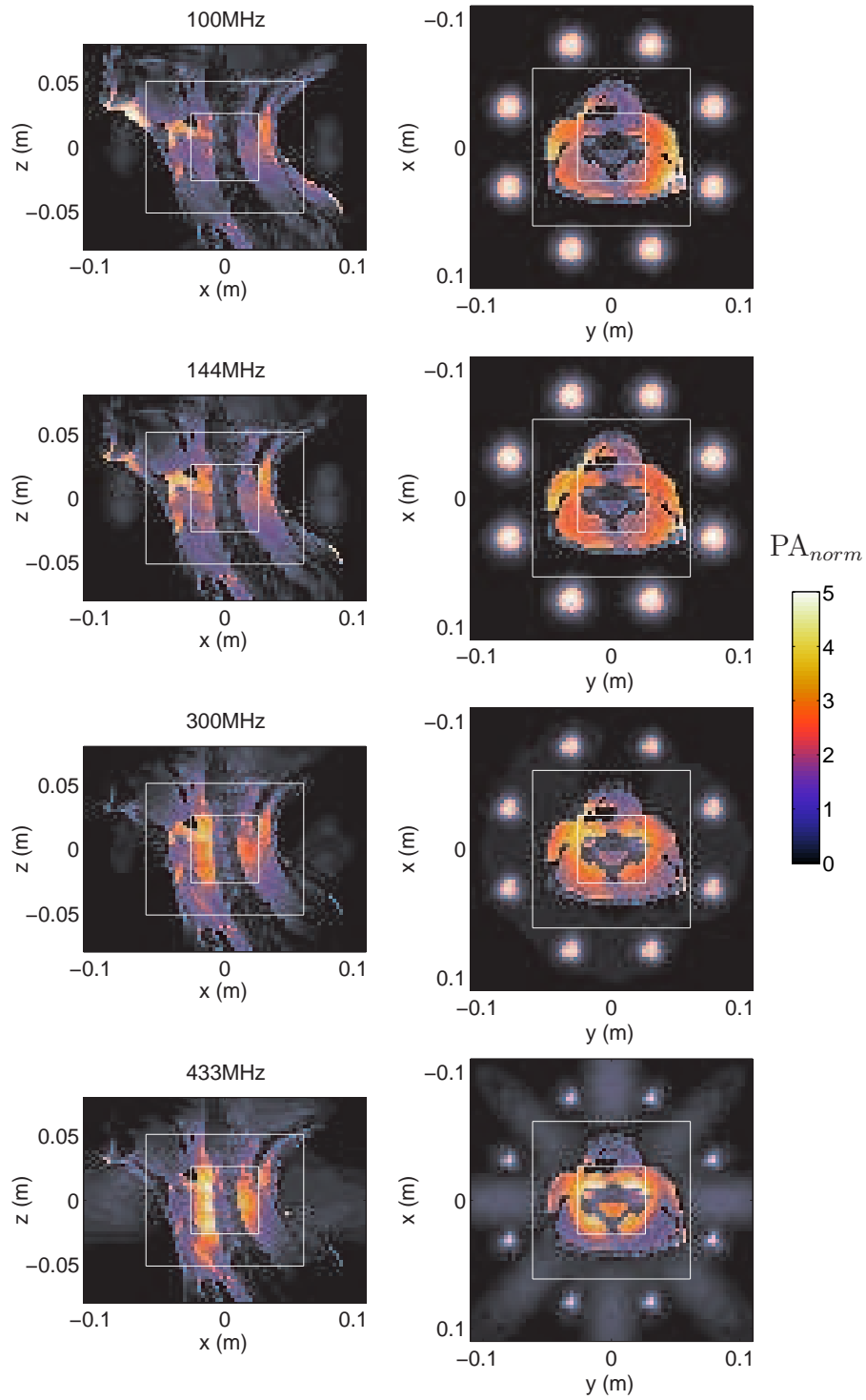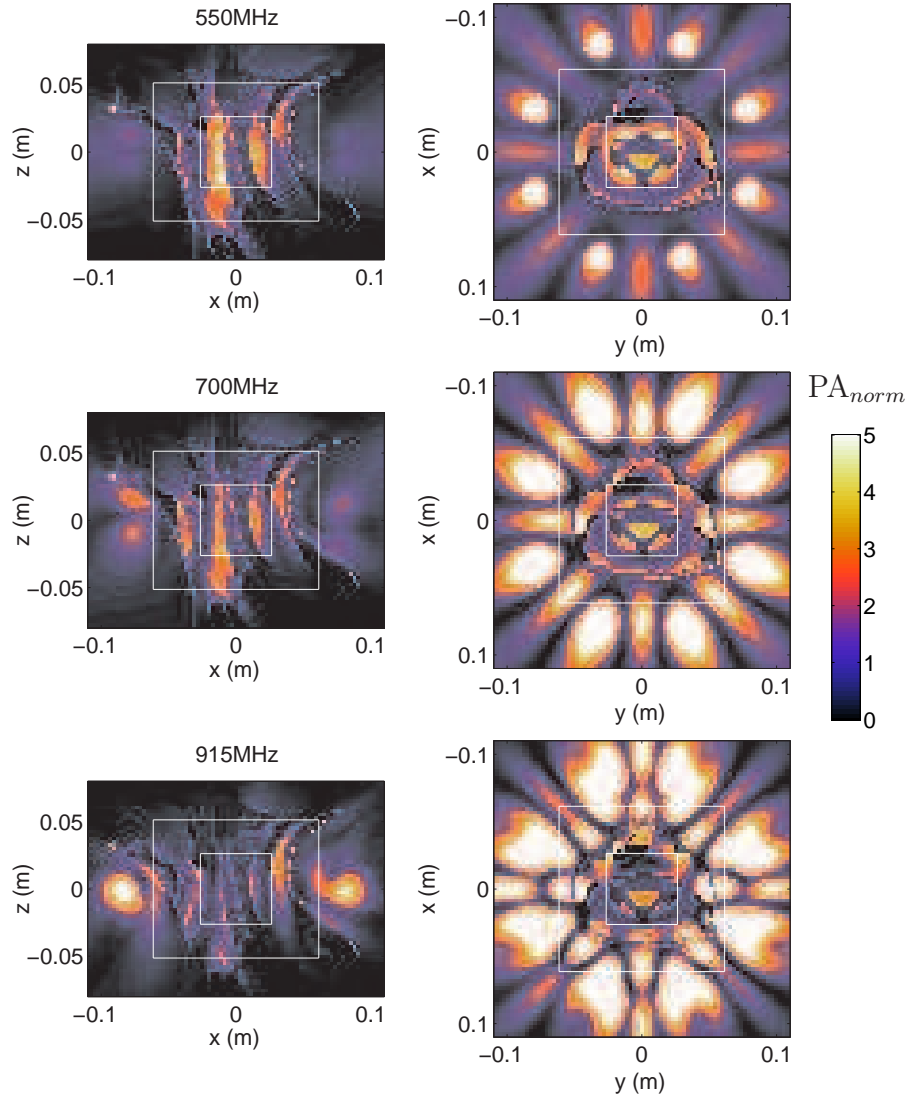
Figure 2.4: PA distributions in the neck at cross-sections through $y = 14$ mm (left) and $z = 0$ mm (right) resulting from FDTD calculations. The PA values are normalized to the average value in the neck volume. The target and neck volume are indicated by the white squares.

rounding water and consequently to high losses which reduces the efficiency of the applicator. Unwanted high PA values are visible in the chin region as well, for high and low frequencies, due to a lower central PA intensity. Note that for high frequencies smaller dipoles are used and thus the antenna-chin distance is larger, which implies that the PA in the chin was expected to be lower. The intermediate frequencies result in a centrally positioned focus covering almost the entire target domain. As expected, the bony structures receive little energy due to their low conductivity.

Figure 2.5 summarizes the PA distributions of Figure 2.4 by displaying the corresponding aPA ratio values: as a function of target volume and frequency. It shows that the antenna set-up performs well in the range of frequencies between 300 MHz and 700 MHz, where the optimum depends on the target size. When we focus towards the most likely target volume sizes (4x4x4 cm to 6x6x6 cm), this range of optimal frequencies decreases to frequencies between 400 MHz and 600 MHz. For the latter frequencies the average PA in the target volume is approximately two-fold the average PA in the neck volume. Note that higher frequencies perform best for small target volumes and lower frequencies perform marginally better for large target volumes. Note further that the sensitivity of the performance of the system as a function of the frequency is high for small, but low for large target volumes.
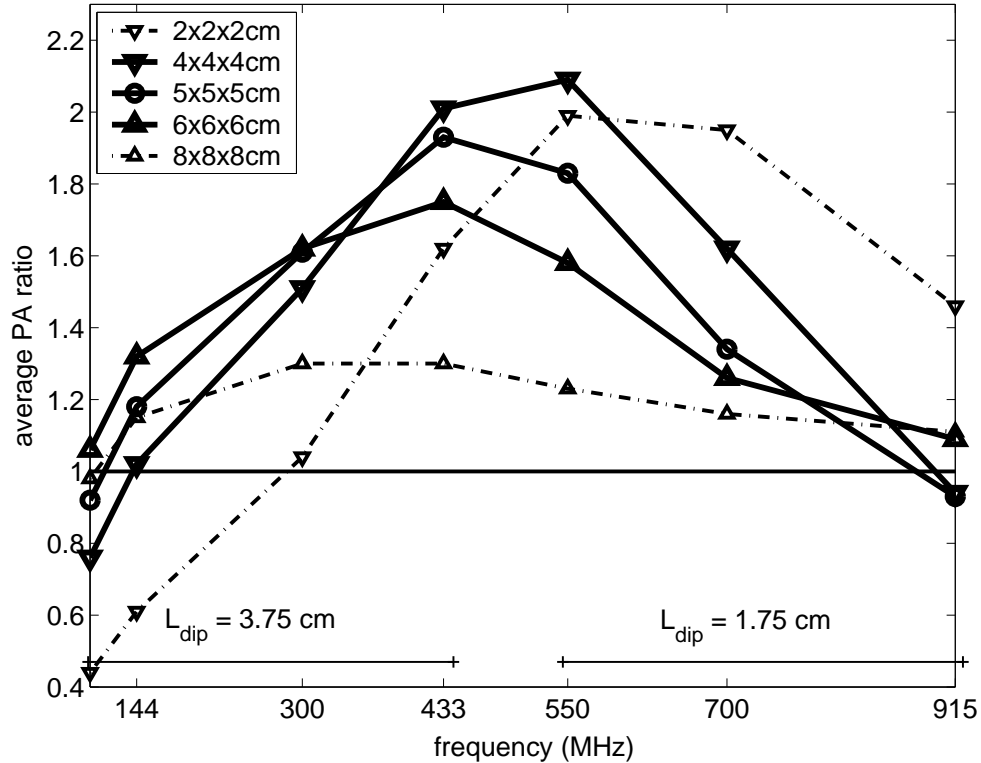
Figure 2.5: aPA ratio values calculated with FDTD as a function of frequency for different target volume sizes. aPA = 1, i.e. the average PA in target and neck volume are equal, is indicated.

2.3.3 Influence of the neck dimensions on the frequency

The third and last series of calculations are carried out to investigate the dependence on the aPA curve of the neck dimensions. Frequencies in the most suitable range for this application are used for this investigation, i.e. 300, 433 and 550 MHz. The distances between the antennas and the skin are constant for all set-ups.
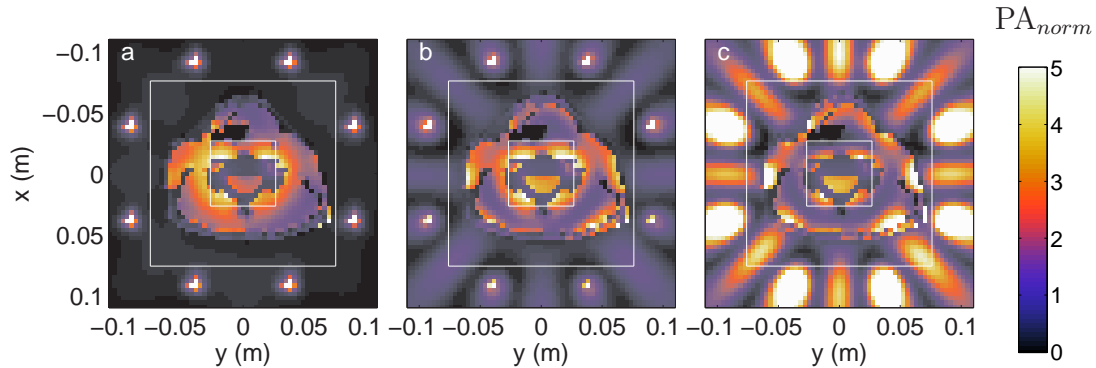
Figure 2.6: PA distributions in the average neck at cross-sections through $z = 0$ resulting from FDTD calculations at a) 300, b) 433 and c) 550 MHz for 8 dipole antennas. The anatomy is scaled with a factor 1.24 (= 12.0 / 9.7) with respect to the original head and neck model. The PA values are normalized to the average value in the neck volume. The target and neck volume are indicated by the white squares.

Figure 2.6 shows the PA distributions for an average anatomy and an eight dipoles configuration operating at 300, 433 and 550 MHz. For comparison reasons the neck and target region (white squares) are equal for all set-ups and equal to the situation for a small neck. Figure 2.6 shows similar distributions, for the average neck, compared to a small patient: comparing this figure to Figure 2.4 (300, 433 and 550 MHz) reveals that the overall pattern remains intact for this larger patient but the superficial absorption increases. This effect is most pronounced at 550 MHz due to the nearby secondary foci.

Figure 2.7 provides a summary in terms of aPA ratio of figure 6 for the small, average and large patient anatomy. It reveals that a large diameter of the neck has a negative influence on the PA pattern at 550 MHz, i.e. the aPA ratio decreases. Further it shows that an increase in anatomy size advocates a lower operating frequency. The analysis shows that 433 MHz from the available frequencies and studied configurations 433 MHz performs best in all cases.

2.4   Discussion

2.4.1   Evaluation of the materials and methods

In work published by Jacobson and Melandsø[41], a possible frequency range of 100 to 750 MHz is indicated for heating H&N tumours. Taking into account the results of their 20 study we selected the frequencies that are used in this study. The three frequencies that are selected for the determination of a suitable number of anten-
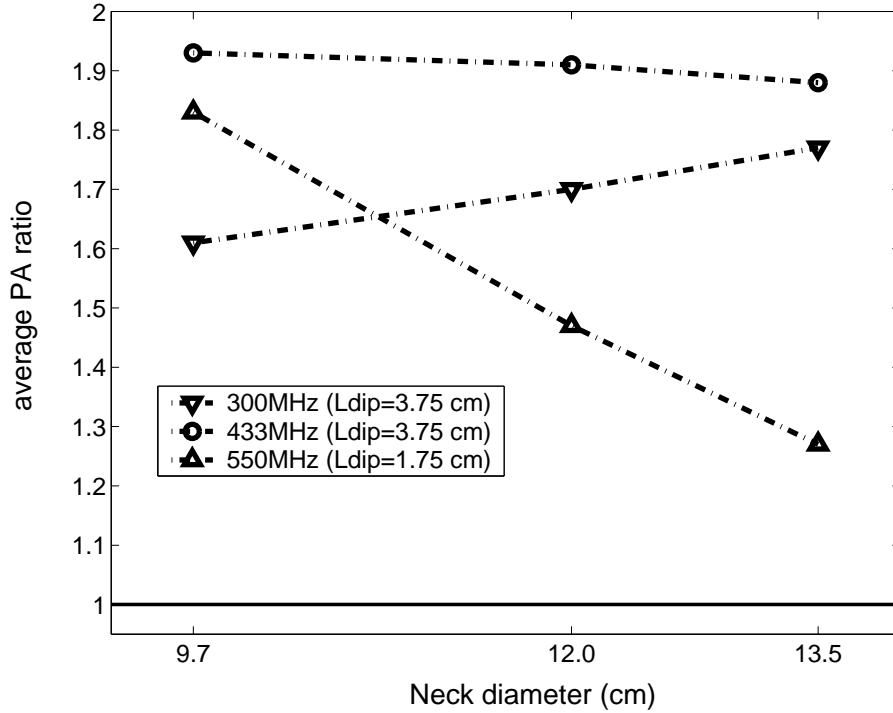
Figure 2.7: aPA ratio values calculated with FDTD as a function of frequency for an anatomy with a small, average and large neck diameter. The target region is 5x5x5 cm and the neck volume is 12x12x10 cm, 14.8x14.8x12.4 cm and 16.7x16.7x14.0 cm for the small, average and large configuration, respectively.

nas, i.e. 100 MHz, 433 MHz and 915 MHz, span the indicated frequency interval and/or conform to ISM frequencies. For the first two frequencies high-power amplifiers are available in our department (Erasmus MC - Daniel den Hoed Cancer Center) enabling future verification PA measurements in phantom models.

The first part of this work is the construction of a (truncated) anatomy segmentation. The truncations have little influence on the PA distribution in the neck volume because the electric field near the transitions is low; thus little power is reflected at the boundaries.

To reduce the number of set-ups to be analyzed, only two different dipole heights are used. The dipoles are resonant ($\lambda/2$) or smaller which has a high influence on the efficiency but a small influence on the radiation pattern[5] of the dipole. For this theoretical study the efficiency is of limited importance since the PA distributions are compared qualitatively.

When evaluating the obtained predictions we faced the common problem of the inability to define the quality of a hyperthermia treatment[70]. From a biological point of view the focus is on thermal dose relationship[14,17]. Such an approach is well validated in a clinical environment although it provides only retrospective information.

For applicator development, the main source of information are data from predicted specific absorption rate (SAR), or PA, distributions (where the PA and SAR values are related through the mass density). As a result, a strong need exists for an objective criterion to express the quality of the SAR distribution. The Effective Field Size (EFS[‡]) and penetration depth as defined within the ESHO quality guidelines[32] provide a general solution for single applicators and SAR distributions in 'semi' homogenous, e.g. layered, phantoms. Other parameters, like the areas enclosed by the 25%, 75% iso-SAR contour and their ratio EFS75%/EFS25%[28,80] have been suggested for superficial hyperthermia. Here again, they are intended for use in simple phantom configurations. In the development of loco-regional (deep) hyperthermia techniques, application of EM-modelling has a longer history and various evaluation procedures have been used[38,77]. As a global indicator the ratio of the SAR50% in the tumour to SAR50% in the total volume is frequently used[107]. The aPA ratio follows an approach similar to that of Paulsen *et al.*[77]. It differs from the index defined by Wust *et al.*[107] in the sense that the quotient of power absorption in the target region and the neck is used, thus the influence of a normalization procedure is excluded. The aPA ratio is strongly dependent on the size of the target volume and thus the choice of its dimensions is of high importance. The size of the target region is chosen to vary from 2x2x2 cm to 8x8x8 cm, where the focus is on sizes between 4x4x4 cm and 6x6x6 cm since the aim is to heat advanced tumours together with lymph node metastases.

In this study, to speed up the analysis, we omitted SAR pattern optimization. Because the set-up under study is fairly symmetrical, we assumed that optimization of the amplitudes and phases would only minimally alter the SAR patterns. Further, we have focussed on the global PA pattern and therefore we have not performed a comparison of the set-ups in terms of (the avoidance of) hotspots in normal tissue. Therefore, we expect that the conclusions will hold when analyzing optimized SAR patterns.

2.4.2 Discussion of the results

For the positioning of the sources, we found that antenna positions close to the chin region should be avoided in order to decrease the influence of the limiting hotspot in the chin region. The optimal amount of antennas of the investigated set-ups is sixteen, where six and eight antennas are found to be highly suitable as well. The good performance with eight antennas as found in this study is in agreement with Jouvie *et al.*[45]. They found that a set-up comprising eight dipoles at 433 MHz for H&N HT is approximately optimal; their approach though was by use of 2D calculations. The number of antennas, however, should be increased when the frequency is increased, for an optimal SAR distribution[77]. More antennas, though, result in a higher complexity. For the clinical practice, a system with low complexity

---

[‡]EFS: the area enclosed by the 50% iso-SAR contour.

is preferable and therefore a low amount of antennas is desired. For the frequency investigation we selected eight antennas since this provides a close to optimal result and is a clinically acceptable amount of elements.

For a set-up of eight antenna elements, it is found that low frequencies (100 MHz and 144 MHz) result in superficial absorbtion only (Figure 2.4). This seems very counter intuitive as lower frequencies generally correspond to higher penetration depths. At these frequencies for our set-up, a difficult complex interaction occurs between tissue and antennas. From the current results we anticipate that the interference pattern suffers from an insufficient distance between the antennas and the center of the anatomy. A small distance in terms of effective wavelength in the media may flatten the maximum and increases patient load influences.

The optimal frequency is amongst others dependent on the number and location of the sources and the target size. Hence, it is difficult to select a single optimal frequency. For target sizes between 4x4x4 cm and 6x6x6 cm optimal frequencies in the range of 400-600 MHz are found. For two out of three target sizes the best performance is obtained at 433 MHz where for the smallest target size at 550 MHz the best performance is achieved by use of the eight antenna set-up. For larger target sizes the optimal frequency range shifts to somewhat lower frequencies, i.e. between 300 MHz and 433 MHz.

This investigation was carried out using a 9.7 cm in diameter neck and scaled versions with neck diameters of 12 and 13.5 cm. The calculations at 300, 433 and 550 MHz indicate the best performance at 433 MHz for all realistic neck dimensions. It should be noted that usually a small neck contains more muscle in comparison to a large (in diameter) neck. A higher percentage of muscle results in a lower penetration depth thus reducing the interference at depth. Therefore a more pronounced focus is anticipated for a large neck with a high fat percentage. Jacobson and Melandsø[41] and Gross *et al.*[29] previously investigated the possibility to heat H&N tumours.

Jacobson and Melandsø predicted and measured a central focus in a cylindrical, muscle equivalent, phantom with four spiral antennas radiating with equal phases at 488 MHz. In the study of Gross *et al.*, four in-phase dielectric loaded circular horn antennas are used to illuminate a muscle phantom. They measured a better focus at 400 MHz compared to 915 MHz in case of a phantom with a diameter of 11 cm. The data as presented in this publication narrows down the range of interesting frequencies indicated by Jacobson and Melandsø but presents a confirmation by 3D FDTD calculations of the measurements by Gross *et al.*.

The influence of using multiple antenna rings is investigated by both Seebass *et al.*[83] and Paulsen *et al.*[77] who found an optimal frequency of approximately 150 MHz for their deep hyperthermia systems consisting of three (Seebass *et al.*) or four (Paulsen *et al.*) rings of antennas. Both studies differ from the present study in the fact that the aim is to heat tumours in the pelvic region where the average diameter of the body is approximately three times larger. Converting the optimal frequency for deep hyperthermia (150 MHz) to our set-up, taking into account the different required penetration depths and assuming a cylindrical approximation in both cases, would

result in an optimal frequency around 450 MHz. This provides some support of an optimum frequency in the range of 400 to 600 MHz for heating head and neck tumours when using multiple antenna rings.

2.5   Conclusion

In this study, we investigated the ability of a multi-element, single antenna ring, H&N HT applicator to deposit RF energy selectively in the center of the neck, while sparing the normal tissue in the neck. It provides a quantitative confirmation of our intuitive applicator design.

It has been found that positioning antennas closely to the chin should be avoided. Further, eight antenna elements is shown to be a suitable number of antennas for frequencies in the investigated frequency band for a set-up of one concentric ring of equally spaced antennas. The optimum frequencies are shown to be in the frequency band between 400 and 600 MHz for the investigated target sizes. This frequency band shifts downwards for larger target volumes.

From the findings of this study and the fact that 433 MHz is an ISM frequency at which high power amplifiers are available in our clinic we feel it is highly justified to continue our investigations at 433 MHz. The actual number of antennas and use of multiple rings of antennas are subject of further research, where an optimum is expected around six to eight antennas per ring.

Acknowledgements

CHAPTER 3

Local SAR distortion by major anatomical structures

Abstract

The objective of this work is to investigate the distortions on the local SAR distribution by various major anatomical structures in the neck. High resolution 3D FDTD calculations based on a variable grid are made for a semi-3D generic phantom based on average dimensions obtained from CT-derived human data and in which simplified structures representing trachea, cartilage, spine and spinal cord are inserted. In addition, phantoms with dimensions equal to maximum and minimum values within the CT-derived data are also studied. In all cases, the phantoms are exposed to a circular coherent array of eight dipoles within a water bolus and driven at 433 MHz. Comparisons of the SAR distributions due to individual structures or a combination of structures are made relative to a cylindrical phantom with muscle properties. The calculations predict a centrally located region of high SAR within all neck phantoms. This focal region, expressed as contours at either 50% or 75% of the peak SAR, changes from a circular cross-section in the case of the muscle phantom to a donut shaped region when the anatomical structures when the anatomical structures are present. The presence of the spine causes the greatest change in the SAR distribution, followed closely by the trachea. Global changes in the mean SAR relative to the uniform phantom are < 11% whilst local changes are as high as 2.7-fold. There is little difference in the focal dimensions between the average and smallest phantoms but a decrease in the focal region is seen in the case of the largest phantom. This study presents a first step towards understanding of the complex influences of the various parameters on the SAR pattern which will facilitate the design of a site-specific head and neck hyperthermia applicator.

3.1   Introduction

Patients with advanced carcinomas in the head and neck (H&N) have a dismal prognosis and loco-regional control for this site still poses a major therapeutic challenge. Combining radiotherapy (RT) with simultaneous chemotherapy improves the treatment outcome but at the cost of increased toxicity. Triggered by the phase III trial of Valdagni *et al.*[94,95], we started the exploration of hyperthermia (HT) applied to the head and neck region. Valdagni demonstrated that with a non-specific HT-applicator already a significant increase in local control (from 24% for RT alone versus 69% for RT plus HT) is achieved for metastatic lymph nodes in Stage IV carcinoma of the H&N, without additional toxicity. However, for an optimal HT treatment of the primary tumour and metastatic lymph nodes a specific H&N HT applicator is warranted. In our opinion such a site-specific designed, multi-element, applicator would also enable a substantial improved control of the specific absorp-

tion rate (SAR) deposition pattern and is expected to result in a higher quality of the HT-treatment (Wust *et al.*[107]).

The head and neck region is characterized by many tissue transitions, small structures and large cooling vessels. Applying an adequate thermal dose to the head and neck region therefore is a challenging task. In the clinical set-up the thermal dose is determined by a huge amount of parameters with separate and combined influences. From a designers point of view the aim is to approach the problem by simplification of the problem since 1) this increases the development progress, 2) provides a better understanding of separate parameter influences, 3) enables verification measurements and 4) links with quality assurance set-ups. As a first step we start this SAR-based investigation with the most simple set-up: an array of eight dipole antennas radiating a centrally positioned muscle equivalent cylinder representing a first approximation of the neck. This simple set-up forms the reference configuration from which the problem is extended to a more and more realistic neck anatomy. The influence on the SAR pattern of various parameters can now be regarded distortions on the local SAR pattern with respect to the reference configuration.

The causes of the perturbations on the SAR distribution in the region of interest are clustered in three groups: 1) anatomy, 2) antenna array and 3) waterbolus related distortions. These parameters can be investigated independently, allowing a better understanding of their - sometimes opposing - effects. In this publication we dedicate our attention to the anatomy related effects, thus a fixed applicator and waterbolus design are chosen, i.e. an array of dipole antennas embedded in an infinite water space. The SAR distribution in the neck is, to a large amount, dictated by the tissue distribution in the H&N region and it is our expectation that a thorough exploration of the anatomy-based distortions will pay off in the applicator design. Exploring all different anatomy-related influences is a vast task and therefore a distinction is made between 2D and 3D anatomical shape-related SAR perturbations. In this work we focus on 2D related effects, while the 3D related distortions are subject of further research. With 2D related distortions we refer to the influences on the SAR pattern caused by differences in tissue in the radial direction, however the assessment is carried out with a 3D FDTD calculation. The investigation is carried out by placing inserts representing major anatomical structures in the muscle cylinder. The distortions on the SAR pattern caused by these major structures are subsequently addressed by comparison of their respective SAR distribution with the SAR pattern in the muscle cylinder.

This investigation is carried out at 433 MHz since it is found to be within the range of promising frequency candidates for a head and neck applicator[41] and equipment for latter verification measurements at this frequency is available at our clinic. The configurations are chosen such that at 433 MHz in a water environment ($\epsilon_r = 78$) the cylindrical phantoms are located in the far-field region of the antenna array. Combined with a contrast-type SAR pattern distortion evaluation parameter, i.e. Relative Differences (RD's), yields an investigation that is only very limitedly dependent on the radiation patterns of the antennas.

Table 3.1: Relative permittivity, effective conductivity and mass density for the selected neck structures and the surrounding water at 433 MHz.

Structure	ϵ_r	σ_{eff} (S/m)	ρ (kg/m^3)
Muscle	57	0.80	1050
Trachea (air)	1	0.00	1
Cartilage*	45	0.60	1100
Spine (Bone, cortical)	13	0.09	1595
Spinal cord (Brain, white matter)	42	0.45	1050
De-ionised water (0.00 g/l NaCl, T = 20°C)	78	0.04	998

* no discrimination is made between dry and wet cartilage

3.2　Materials and methods

3.2.1　Creation of the average neck phantom

A homogeneous muscle cylinder is used to model the anatomy as a starting point. From this base situation the set-up is extended towards a more realistic neck anatomy by inclusion of inserts representing major structures, e.g. trachea and spine. The shapes of the structures in the neck vary strongly in the radial direction and only to a lesser extent in the axial direction. Therefore the shape of these structures is approximated by elementary shapes (Figure 3.1). Extruding these shapes results in semi-3D approximations of the original structures. The dimensions of the shapes are defined using Computerized Tomography (CT)-scans from which the minimum, average and maximum dimensions and locations of the major neck structures are extracted. The neck in this case is defined as the elliptically shaped area between the widening curvatures towards the head and towards the shoulders.

In this parameter study we focus on structures with an expected large influence on the SAR pattern. The selection criteria for inclusion in the model of an anatomical structure are: 1) existence in the neck in the axial plane (from collar bone up to the oropharynx), 2) amount of dielectric contrast with neighbouring tissue (muscle), 3) size of its transverse cross-section, 4) amount of perfusion. It is expected that the amount of perfusion is an issue mainly in areas consisting of cartilage. The SAR in these areas probably will not appear to be dramatic but might, due to the poor perfusion, cause limiting hotspots, i.e. burns. Table 3.1 shows the list of structures that are selected using these criteria. The "cartilage" is the cartilage of the trachea. The skin and oesophagus are not included in the considerations due to their small transverse cross-sections and low dielectric contrast with respect to the neighbouring muscle tissue. No fat is selected since in these patients only a small amount of fatty tissue is present, which is overshadowed by the large muscles that it surrounds. The influence of a small layer of subcutaneous fat is assessed as a side step.

Determination of the elementary shapes

The selected structures (Table 3.1) are fitted by elementary shapes (Figure 3.1b). The dimensions of these shapes are extracted from CT scans of eight patients from a representative patient group, i.e. H&N patients at our radiotherapy department with tumours at various sites (hypopharynx, parotic gland (3x), larynx, oropharynx and nasopharynx (2x)).

The dimension extraction is carried out by calculation of the mean of the Hounsfield Unit (HU) distribution, i.e. averaging the HU's in the CT scans of the 4th down to the 6th cervical vertebra for every patient (14 - 19 slices). An example average HU distribution is shown in Figure 3.1a. Markers are positioned in this average HU distribution at every extent of a structure and subsequently the dimensions of the structures are calculated using their respective locations. For example, a circle is described by four markers defining two radii (in the x and y-direction). These markers are then used to calculate the smallest, average and largest value of each dimension (Figure 3.1b), which are presented in Table 3.2. These dimensions are calculated such that they are symmetrical with respect to the sagittal plane ($x = 0$).

a) Average HU distribution   b) Rounded elementary-shape fit
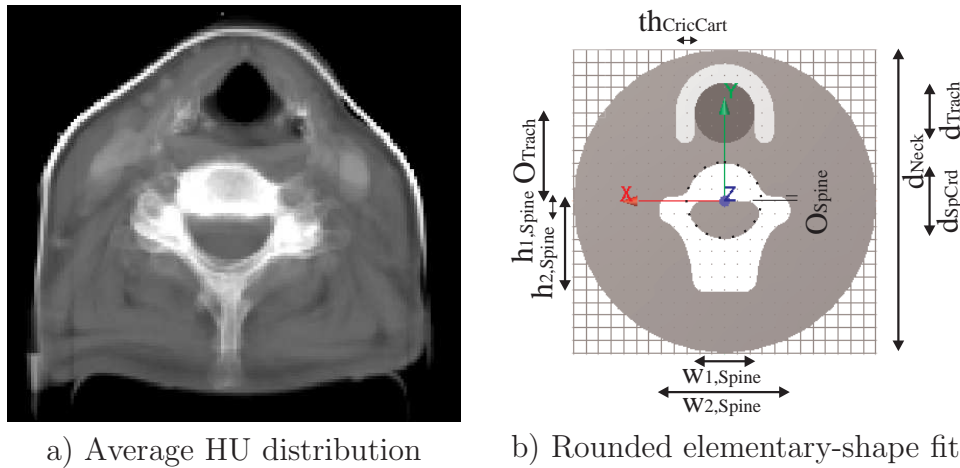
Figure 3.1: a) Example average ($4^{th} \leftrightarrow 6^{th}$ neck vertebra) HU distribution of one patient and b) the rounded elementary-shape fit with 2D shapes (average dimensions of multiple patients). The dimensions of the shapes correspond to those of tabel 3.2 and the distance between the mesh lines is 5 mm. Note that the lower part of the spine seems to have a larger width in b) compared to a) which is the result of (i) the different shapes of the vertebra's and (ii) our focus on the central vertebra, which sometimes consists of two peaks.

The most difficult tissue type to assign is the cartilage surrounding the trachea, due to its low HU contrast with surrounding muscle. Therefore, for guidance of positioning the markers of the trachea surrounding cartilage, an anatomy book is used[61].

Table 3.2: Smallest, average and largest dimensions (mm) of the selected neck structures and the rounding radius per geometry. The abbreviations refer to a d(iameter), th(ickness), O(ff-set), h(eight), w(idth) or r(adius). The off-sets are shifts, with respect to the origin, in the y-direction.

Dimension	Smallest	Average	Largest
d_{Neck}	97	120	135
d_{Trach}	19	25	29
O_{Trach}	28	36	41
th_{Cart}	5	8	9
d_{SpCrd}	27	31	34
O_{SpCrd}	0	0	0
$w_{1,Spine}$	48	52	58
$w_{2,Spine}$	19	25	29
$h_{1,Spine}$	25	37	51
$h_{2,Spine}$	8	10	12
O_{Spine}	2	2	2
$r_{rounding}$	4	5	6

The elementary shapes are subsequently extruded using the solid modelling kernel of SEMCAD[84] to become a 250 mm high cylindrical shape: the "solid model". This solid model is rounded, using rounding radius $r_{rounding}$, to avoid local hotspots due to a sharp model. This rounding is applied because the aim is to study macroscopic influences of anatomical structures and not hotspots due to patient specific sharp edged structures. Further, applying the rounding increases the visual resemblance between the model and the average HU distributions. The neck model is chosen sufficiently high to avoid influences, in the plane of interest, of the upper and lower transitions (tissue $\leftrightarrow$ water). A cross-section of the average solid model is shown in Figure 3.1b. Similar set-ups are conducted using the smallest and largest found dimensions (Table 3.2) forming the "smallest" and "largest" cylindrical neck phantoms.

Creation of a semi-3D neck anatomy for contour verifications

A semi-3D neck anatomy is created to be able to investigate the difference in SAR distribution of an approximation of the neck by 1) a cylindrical neck shape with elementary shaped inserts versus 2) a neck with actual contours. This latter anatomy is constructed from **a single slice**, at the height of the 5th cervical vertebra, of **a single patient**. The patient with neck dimensions close to average (Table 3.2) is selected. Note that this does not mean that every dimension of the patients neck

structures is average. The contours of the neck structures are found by applying a HU-based threshold contour fit procedure. These contours are subsequently extruded to form a semi-3D neck anatomy, where the same structures are selected as for the average neck phantom (Table 3.1). There was little difference in HU value between cartilage and the surrounding muscle, so only a small piece of (probably ossified) cartilage could be selected. It is noted that simulations, with assigning bone and subsequent cartilage to this small piece, have confirmed that its influence is negligible (in the $z = 0$ cm plane) so the small piece of cartilage was excluded for further calculations.

3.2.2 Applicator model

The applicator is modelled by, a close to optimum number of[45], eight dipole antennae, radiating at 433 MHz, that are positioned at equal distances on an imaginary ring surrounding the neck (Figure 3.2a). The dipoles are embedded in an infinite water space because we anticipate the use of a waterbolus. However, the disturbing influences of the waterbolus on the SAR pattern are outside the scope of this study. The diameter of the applicator ring is chosen such that it can enclose a large male neck (diameter = 16 cm) with a sufficient overlap ($> \lambda/2 = 4$ cm) at all sides, i.e. the diameter of the antenna ring is chosen to be 25 cm. Halve-wave dipoles, resonant at 433 MHz, are utilized in the antenna ring. In practice, a somewhat smaller height than $\lambda/2$ must be used for the dipoles to account for their, non-infinitely small (0.25 cm), diameter[5]: the height of the dipoles is 3.25 cm. The radiation pattern of the antennas is not influenced by the phantom because the phantom is located in the far field (~ 4 cm[5]). Therefore, the choice of applicator antennas, and thus their radiation pattern, is in fact of limited importance since a contrast type of evaluation is used.

3.2.3 FDTD modelling

For the calculations of the electromagnetic field and SAR distribution we utilized SEMCAD[84]: a Finite Difference Time Domain (FDTD)[89] algorithm. For the FDTD algorithm, the entire computational domain must be divided in voxels, i.e. small brick shaped elements. The computational domain is truncated using Highdon's 2nd order boundary conditions[89] and steady state is assumed after 10 periods (5% difference from the peak value). The solid model of the applicator and tissue are used to assign a label to each voxel, in this way describing the set-up in voxels. Every label is assigned certain dielectric properties. The dielectric properties of the structures in the neck are found using an application of IFAC-CNR[69] based on a parametric model by Gabriel *et al.*[26] (Table 3.1).

The dielectric properties of the trachea are chosen equal to those of air. The properties of the de-ionized water (salinity = 0.00 g/l, T = 20°C) in the waterbolus are found in both a publication of Stogryn[88] and of the ESHO taskgroup comittee[11].

The properties of a voxel in the x, y and z-direction are identical, so an isotropic tissue distribution is obtained.

SEMCAD provides the possibility of a global grid refinement: the grid lines do not have to be spaced homogeneously. This enables the modelling of fine structures whereas the computational effort is only gradually higher. In literature a maximum of the grid stepping between $\lambda/15$[89] and $\lambda/20$ is indicated for sufficient accuracy for a variable grid. This is most critical in regions with high permittivities, which in this case means in the water environment. For this research the maximum grid step, far from the region of interest, is 5 mm thus the grid steps remains smaller than $\lambda/15$: $\Delta_{max} < \lambda/15$. For the main investigation set-up and the set-up to verify the contour influences the respective grid steps are given below.

Neck phantoms (smallest, average and large) The region of interest, i.e. the neck slice between the antenna elements, of the cylindrical neck phantom is modelled with grid steps of 1 mm in the x and y-direction (see Figure 3.2b), however at the antennas a local refinement is applied. The grid steps in tissue in the z-direction vary from 0.5 to 5 mm, but the maximum grid step in the region of interest is 2 mm.

Semi-3D neck anatomy In the z-direction the grid steps vary from 0.5 to 5 mm but the grid steps are 2.5 mm in the x and y-direction since we only aim to compare global SAR patterns using this geometry.

The source of the dipole antennas is modelled with a hard source[89] at 433 MHz, i.e. no feeding circuits are modelled. It is positioned at the 2.5 mm gap between the two conducting ($\sigma = \infty$) poles. The modelling of the antenna is carried out with space steps down to 0.5 mm which provides accurate results as presented by Hertel et al.[36].

3.2.4   Evaluation

The evaluation of the SAR distributions is carried out using data of the plane at $z = 0$ cm through the phantom, i.e. SAR$(x, y, z{=}0$ cm$)$, since the main influences for the neck phantoms are in the 2D plane. A contrast-type formulation is defined to be able to separately investigate the influences of the geometry thus subtracting the influences of the antenna array. The Relative Difference (RD) function is defined as:

$$\text{RD}(x, y) = \frac{\text{SAR}_{guc}(x, y) - \text{SAR}_{ref}(x, y)}{\text{SAR}_{ref}(x, y)} \cdot 100\%, \tag{3.1}$$

where SAR$_{ref}(x, y)$ is the SAR value in the reference situation, i.e. the homogeneous muscle cylinder, and SAR$_{guc}(x, y)$ is the SAR value in the geometry under consideration (guc). This RD quantifies the positive or negative influence of the anatomy

a) Antenna set-up   b) Average neck model
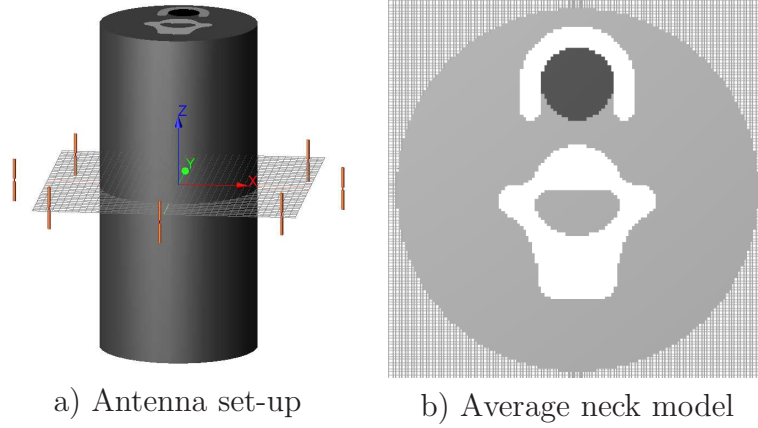
Figure 3.2: Visualization of a) the antenna set-up surrounding the 3D solid model of the average neck phantom, and b) a cross-section at $z = 0$ cm through the FDTD implementation of the average neck phantom, with an overlay of the grid lines. For clarity, the surrounding infinite water space is not visualized in both figures.

on the SAR distribution, i.e. the increase or decrease of the SAR by the anatomy. The minimum, mean, maximum and the standard deviation values of the RD serve as evaluation parameters:

$$\mathrm{RD}_{min} = \min\{\mathrm{RD}(x,y)\}, \tag{3.2}$$

$$\overline{\mathrm{RD}} = \frac{\sum_N w(x,y)\mathrm{RD}(x,y)}{\sum_N w(x,y)}, \quad w(x,y) = \Delta x(x,y)\Delta y(x,y) \tag{3.3}$$

$$\sigma = \sqrt{\frac{1}{N-1}\sum_N (\mathrm{RD}(x,y) - \overline{\mathrm{RD}})^2} \tag{3.4}$$

$$\mathrm{RD}_{max} = \max\{\mathrm{RD}(x,y)\}, \tag{3.5}$$

of the distribution of the relative differences. N is the total amount of voxels in the region under consideration and Δx and Δy are the voxel sizes of every voxel in two directions. For calculation of the mean values the weighting with $w(x,y)$ is applied to account for the variable grid. The importance of this weighting is small since the grid step differs only at the locations of the antennas, where refinement of the grid is applied. RD_{min} and RD_{max} are used to quantify the local SAR influences whereas $\overline{\mathrm{RD}}$ and σ are used to quantify the global SAR (shape) distortion.

The area enclosed by the 50% and 75% iso-SAR contours are investigated to compare inter-geometry results quantitatively in terms of the change in focus size, i.e. the central region of high SAR values.

3.3   Results

3.3.1   Influences per structure

First, a full analysis is carried out on the average geometry with all inserts. This clarifies the way in which all set-ups are evaluated. Each evaluation is a comparison with respect to a muscle cylinder with an identical radius. For clarity of the figures the outer tissue SAR values are not shown unless indicated otherwise.
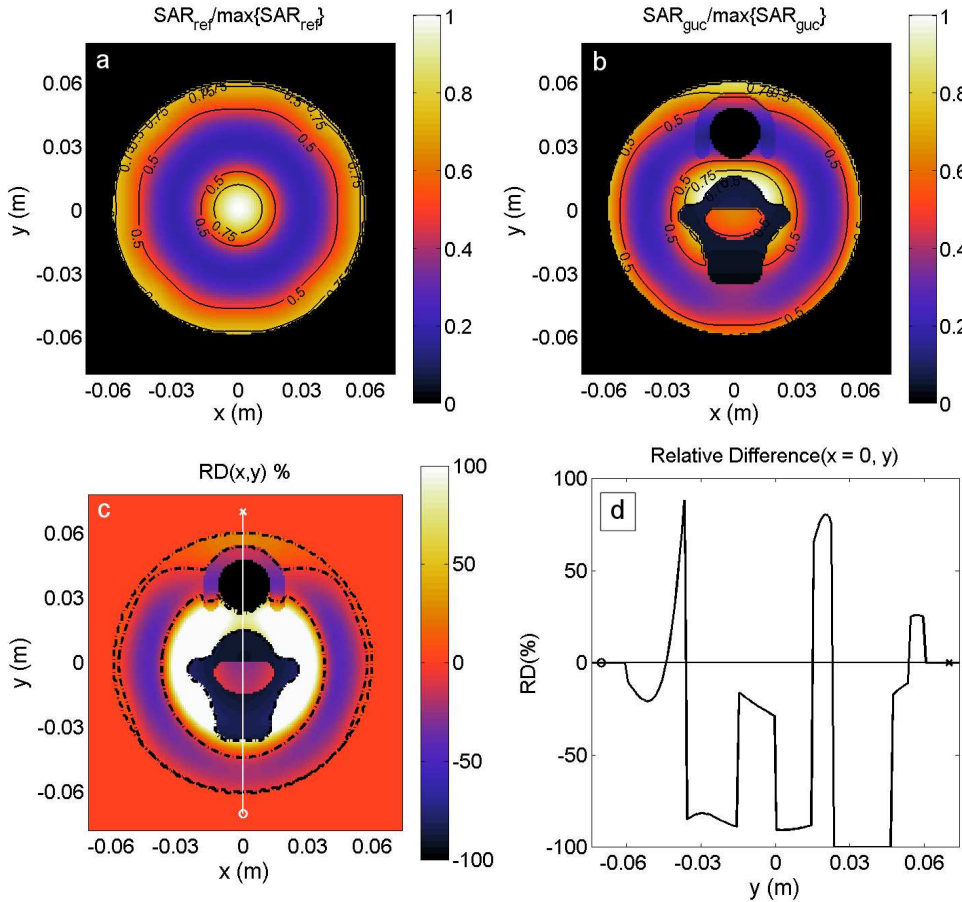
Figure 3.3: a) normalized SAR pattern of the muscle cylinder, b) normalized SAR pattern of the total neck anatomy, c) their RD pattern and d) RD profile at $x = 0$ cm are visualized for the average anatomy set-up at $z = 0$ cm. The 50% and 75% iso-SAR contours are indicated in a) and b), and in c) the RD = 0% contours are visualized (-.-).

Figure 3.3a and 3.3b show the SAR distribution in the average muscle cylinder and average total neck anatomy at a cross-section through $z = 0$ cm. The SAR patterns differ mainly centrally and superficially at and near the trachea. For the total neck anatomy the SAR values are zero at the trachea due to the zero conductiv-

ity. Further, a low conductivity at the spine results in low SAR values. The central hotspot in the muscle cylinder is de-focussed due to reflections at the muscle-bone transition but it remains centrally located. The high SAR values at the location of the spinal cord are lowered due to the anatomical properties. Figure 3.3c and 3.3d visualize the RD distribution and the RD profile at $x = 0$ cm respectively. These images show that the anatomy has a positive influence on the SAR around the spine (RD $\sim 80\%$) and a negative influence at the spine (RD $\sim -80\%$) and trachea (RD $= -100\%$). Regions with a negative RD value ($\sim -25\%$) can also be found approximately 1 cm underneath the "skin". The cross-section at $x = 0$ cm is visualized to show the effect of the conductivity transitions, i.e. all the sharp edges.

Figure 3.4 shows the SAR distribution in the average muscle cylinder and the average muscle cylinder with various clusters of inserts. This figure shows that the high superficial SAR values near the trachea, induced by the insertion of trachea and surrounding cartilage, are reduced by the subsequent insertion of the spine and spinal cord. As a consequence the negative RD values near the trachea in Figure 3.4e are not present in Figure 3.4f and Figure 3.4g. The figure also shows that the global SAR pattern is determined mainly by the cluster containing spine and spinal cord (see SAR and RD distributions).

Table 3.3: $\text{RD}_{min} : \overline{\text{RD}} \pm \sigma : \text{RD}_{max}$ values (%) per geometry for set-ups with smallest, average and largest dimensions (d_{Neck} is 9.7, 12 or 13.5 cm respectively).

Geometry	Smallest	Average	Largest
Musc+cart	-31: 0±6 : 5	-33 : -1 ± 6 : 7	-27 : 5 ± 7 : 16
Musc+trach	-100:-1±23: 44	-100 : -2 ± 23 : 36	-100 : -2 ± 26 : 45
Musc+cart+trach	-100:-2±23: 38	-100 : -3 ± 24 : 36	-100 : -2 ± 27 : 50
Musc+sp.crd	-42: 0±10: 18	-42 : 0 ± 10 : 24	-42 : 0 ± 10 : 29
Musc+sp	-92:11±61: 124	-92 : 2 ± 58 : 157	-92 : 1 ± 61 : 190
Musc+sp.crd+sp	-91:11±70: 149	-91 : 4 ± 69 : 200	-92 : 3 ± 71 : 242
Total neck	-100:11±81: 172	-100 : 2 ± 75 : 224	-100 : -1 ± 76 : 274

Table 3.3 and Table 3.4 are given to quantitatively analyse the RD and SAR patterns. In this section we only refer to the values belonging to the average set-ups. In Table 3.3, the RD_{min}, $\overline{\text{RD}}$, σ and RD_{max} values per geometry are given. From this table, for the average geometry, it can be concluded that the largest local influence is a result from the trachea (low RD_{min}). The largest global distortion is due to the
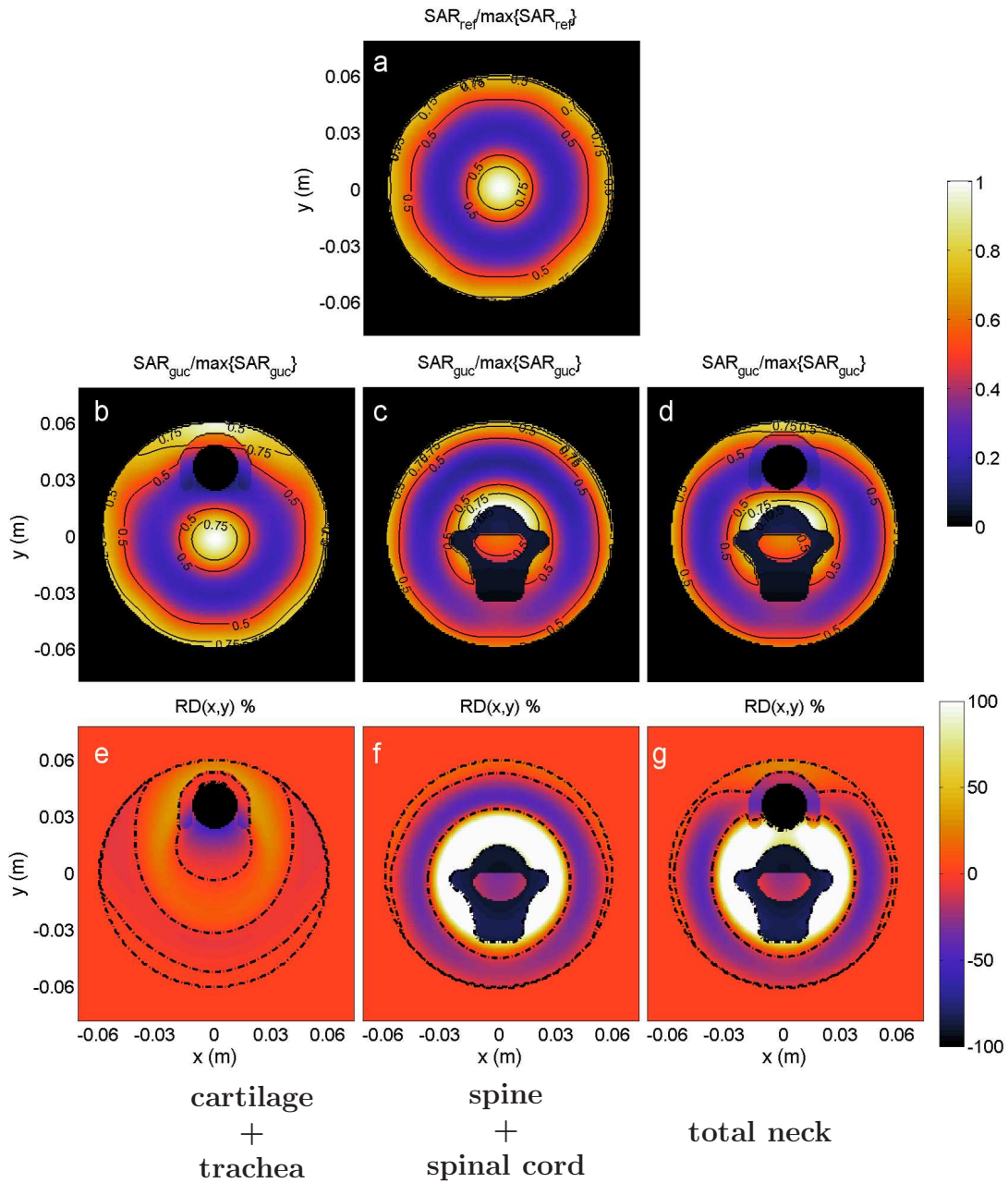
Figure 3.4: The normalized SAR and RD patterns at cross sections through the neck phantom at $z = 0$ are visualized for the muscle cylinder (top), the muscle cylinder with trachea and cartilage insert (left), the muscle cylinder with spine and spinal cord insert (center) and the total neck anatomy set-up (right) for the average set-up (d_{Neck} = 12 cm). The 50% and 75% iso-SAR contours are indicated in the SAR distributions and the zero RD contours are indicated in the RD distribution (-.-).

Table 3.4: The areas (cm^2) enclosed by centrally located 50% and 75% iso-SAR contours per geometry for set-ups with smallest, average and largest dimensions (d_{Neck} is 9.7, 12 or 13.5 cm respectively).

Geometry	Smallest $SAR_{50\%} : SAR_{75\%}$	Average $SAR_{50\%} : SAR_{75\%}$	Largest $SAR_{50\%} : SAR_{75\%}$
Musc	9.6 : 4.0	9.6 : 4.0	5.2 : 0.0
Musc+cart	9.6 : 4.1	9.8 : 4.1	5.2 : 0.0
Musc+trach	9.7 : 4.1	9.7 : 4.1	4.4 : 0.0
Musc+cart+trach	9.8 : 4.0	9.8 : 4.1	3.6 : 0.0
Musc+sp.crd	8.9 : 2.5	8.3 : 2.4	3.6 : 0.3
Musc+sp	10.5 : 4.4	11.0 : 4.7	6.1 : 0.0
Musc+sp.crd+sp	14.0 : 3.7	13.4 : 3.8	4.2 : 0.0
Total neck	14.2 : 4.0	14.2 : 3.5	2.8 : 0.0

inclusion of the spine (high σ). The spinal cord and cartilage cause relatively little distortion.

Table 3.4 provides the areas enclosed by the centrally located 50% and 75% iso-SAR contours per geometry. This table indicates an increased 50% SAR area for the set-ups with inserts, however the area within the 75% iso-SAR contour in some cases slightly decreases (because the normalization point increases). The latter effect is due to the more irregular tissue distribution at the location of the high SAR values, which disturbs the Gaussian shape of the focus.

3.3.2   Influences of structure dimensions

Figure 3.5 visualizes the SAR in the muscle cylinder and total neck set-up and the corresponding RD distribution for the set-ups with the smallest, average and largest dimensions. It shows that the structure dimensions have a low impact on the shape of the central hotspot other than the local structure dimensions. The central SAR however is highly dependent on the radius of the neck, the superficial hotspots even overrule the central hotspot for the largest dimensions set-up. This is mainly due to larger path lengths in the tissue from the antennas to the center of the phantom.

Table 3.3 shows the RD_{min}, $\overline{RD}$, σ and RD_{max} values per geometry for set-ups with smallest, average and largest dimensions. From this table it is concluded that for all set-ups the trachea has the largest local SAR decreasing effect ($RD_{min} = -100\%$) but its global effect is moderate ($\sigma \sim 23\%$). The global influence of the spine is high for all set-ups: $\sigma_{spine} \sim 60\%$. For the smallest dimensions set-up it is found that $\overline{RD} \sim 10\%$ which can be explained by the relatively large area of increased SAR values as a result of the inclusion of the spine (see also Figure 3.5). The analyses presented until now are all carried out by investigating RD's calculated locally. The
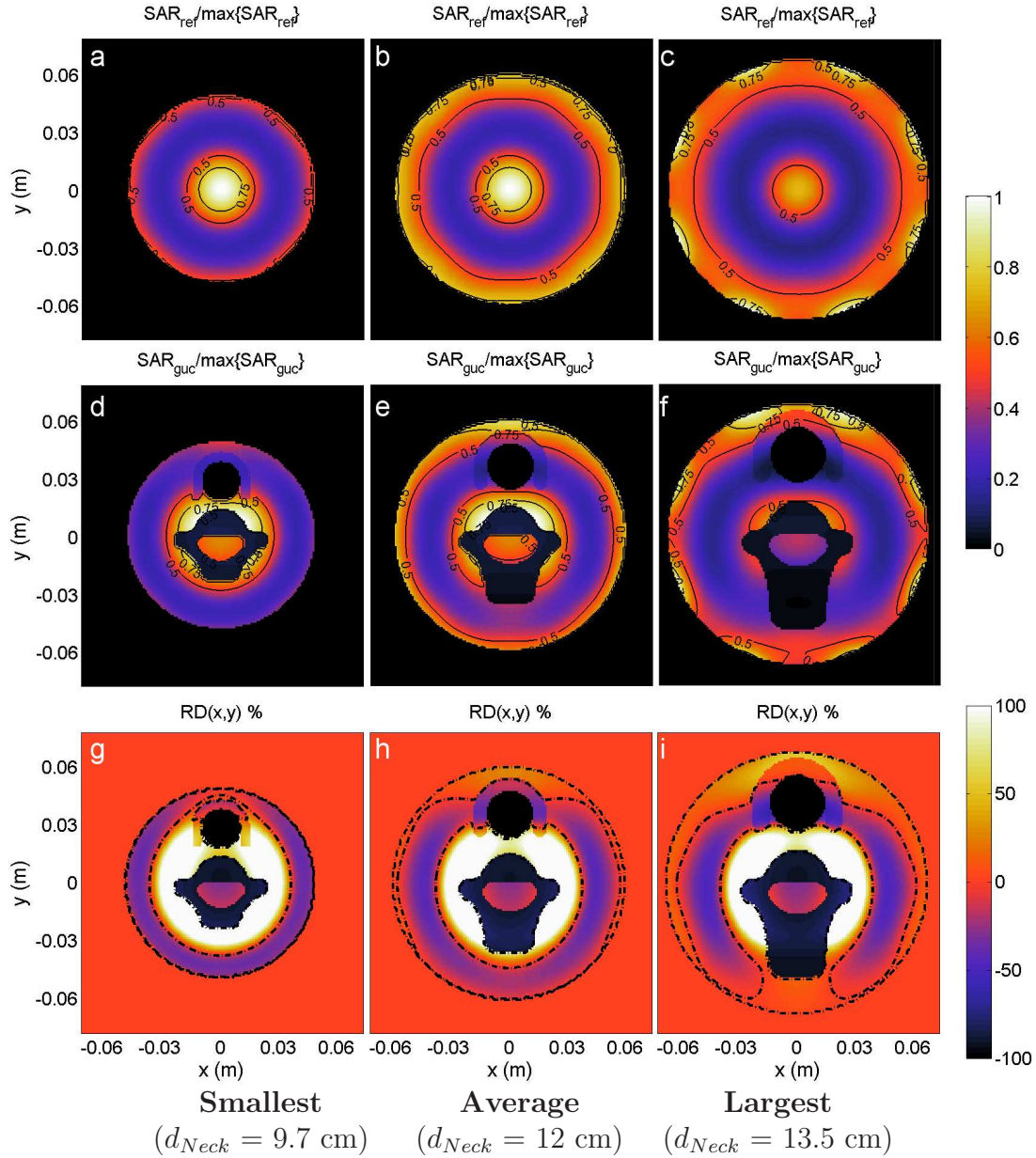
Figure 3.5: The SAR patterns at cross sections through the neck phantom at $z = 0$ cm are visualized for the muscle cylinder (SAR_{ref}), the total neck set-up (SAR_{guc}) and their RD distribution for smallest, average and largest dimensions. The 50% and 75% iso-SAR contours are indicated in the SAR distributions and the zero RD contours are indicated in the RD distribution (-.-).

set-ups can also be compared using a more global approach, i.e. by comparing the mean and maximum SAR of the entire distribution. Figure 3.6a visualizes the ratio of the average SAR levels: $\overline{\mathrm{SAR}}_{guc}/\overline{\mathrm{SAR}}_{ref}$, for the three set-ups. Again, a large
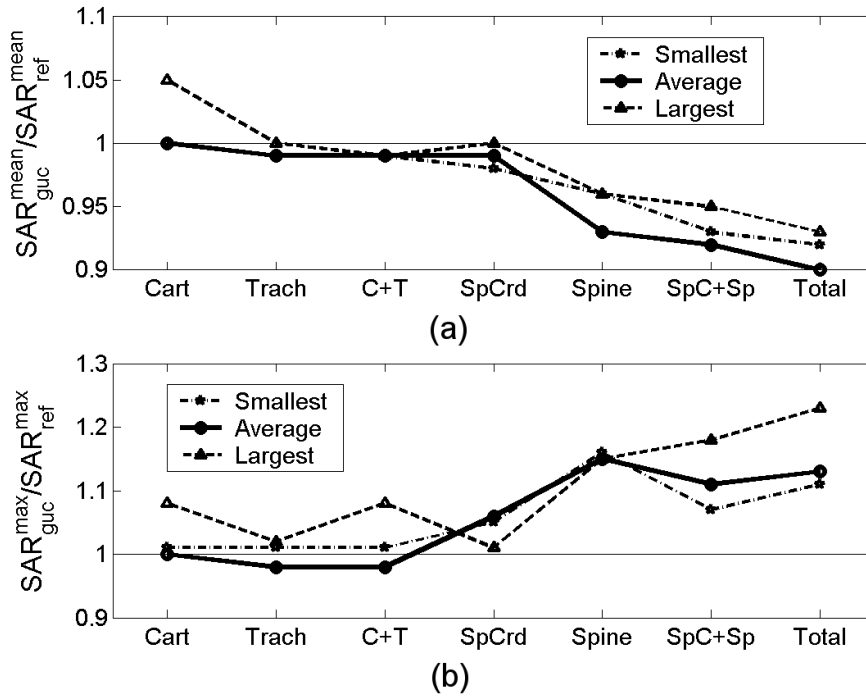
Figure 3.6: Mean (a) and maximum (b) SAR ratios for various structures with respect to the muscle cylinder set-up per geometry for set-ups with smallest, average and largest dimensions

.

global effect of the spine is found: it decreases the overall SAR by $\sim 6\%$. All the inserts together decrease the mean SAR on average by $\sim 7\%$. This influence is almost independent of the dimensions of the set-ups. Figure 3.6b visualizes the ratio of the maximum SAR that can be found in the plane of interest. It is found that the structures increase the maximum SAR value and this increasing influence is most prominent for the set-up with largest dimensions.

3.3.3 Influence of the outer contour approximation

In Figure 3.7 the SAR patterns of the semi-3D cylindrical neck phantom and the semi-3D neck anatomy are visualized. Here again for all set-ups the central hotspot remains at its position but is enlarged by the inclusion of the spine and, to a lesser extent, the spinal cord. The main difference is at the water-muscle transition that is now located closer to one of the antennas. This is in agreement with Figure 3.5, where an increase in radius results in more superficial absorption as well. The comparison between the two set-ups provides some more evidence that the superficial SAR distribution is affected highly by dimensional differences but the central focus remains approximately intact when dimensions are altered.
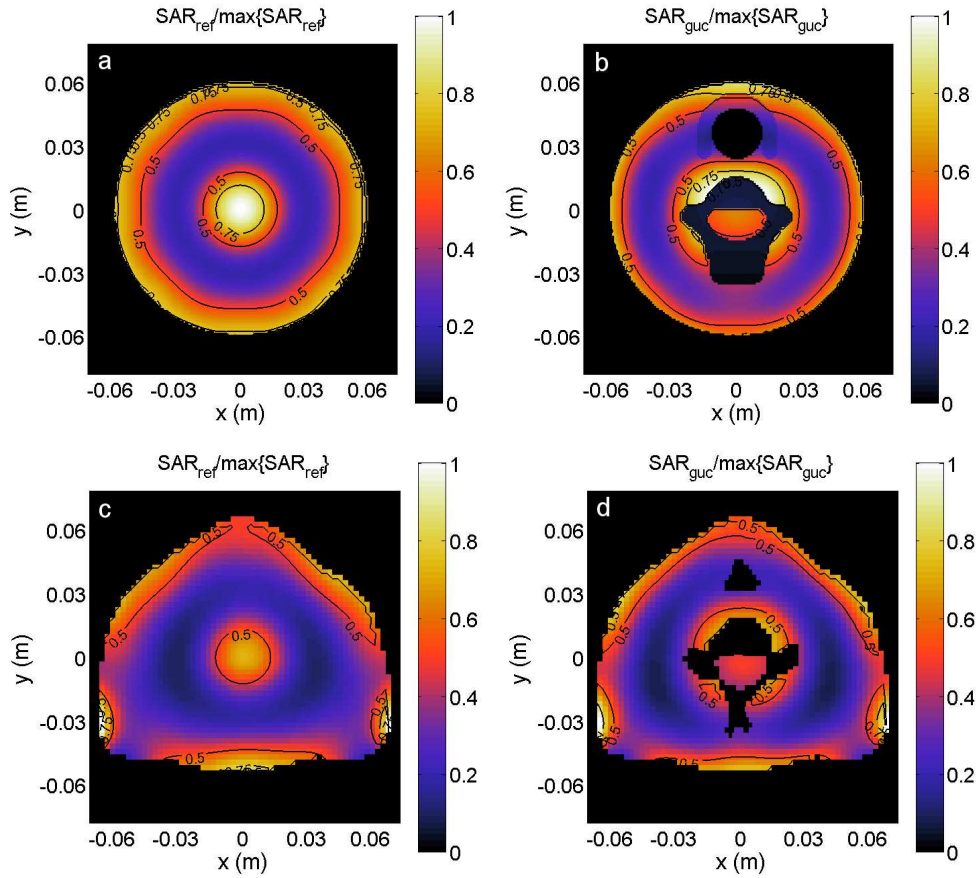
Figure 3.7: The SAR patterns at cross sections through the neck phantom at z = 0 cm are visualized for a) the muscle cylinder and b) the total neck set-up with average dimensions and c) the muscle average anatomy set-up and d) the total average anatomy-neck set-up. The 50% and 75% iso-SAR contours are indicated.

3.4 Discussion

3.4.1 Evaluation of the materials and methods

The main aim of this study is to investigate the influence on the SAR pattern of major structures in the neck, for which a semi-3D average phantom is constructed. The two main approximations for this phantom are the use of extruded 2D shapes instead of 3D shapes and the reduction of real structure contours into elementary shapes.

The influence of the extruded 2D shape approximation is subject of further study; however, some remarks on the accuracy of the SAR distributions can be made. Firstly, the extents of the spine are used for the determination of the average dimensions for the average set-up, i.e. the gaps between the (spinous process of the) cervical vertebras is "filled" with bone material. This is a fair approximation since the fields are axially polarized and because the gaps between the cervical vertebras are approximately 1 cm (= $\lambda/9$ in muscle). Therefore the wave interacts with the independent vertebra's as if it is one solid obstacle (with an effective permittivity and conductivity). Secondly, the trachea and spinal cord are approximately vertical in the region of interest and can therefore be approximated by 2D structures (see Figure 3.1). Other structures, located outside the region of interest could influence the SAR pattern due to field rotations. Most of them, however, are located far from the region under consideration.

The influence of the reduction into elementary shapes, instead of the use of the actual patient contours, on the central SAR focus is small. However from Figure 3.7 it is found that the superficial SAR is increased for a 2D anatomy phantom as a result of the difference in skin contour. Note though that the set-up that is used for the comparison is constructed from one CT slice of one close-to-average patient. The finding, however, is in agreement with the trend from the size investigation, i.e. the SAR in a total neck set-up is increased in areas located just over 6 cm (= $2/3 \lambda$ in muscle) from the center (see the RD distributions in Figure 3.5). From this comparison it is concluded that the shapes of the SAR distributions, and therefore the trends of the findings, only moderately change as a result of the outer contour approximation. This conclusion might also be of importance with respect to quality assurance measurements since these are usually carried out utilizing cylindrical set-ups.

Influence of dielectric properties, voxel sizes and a subcutaneous fat layer

In literature, the variations with respect to the permittivity and conductivity values of Table 3.1 are approximately 25%[22,24,25], where the conductivity has a tendency to be somewhat higher compared to the values in the table. From Van de Kamer *et al.*[96] it is found that the influence on the mean SAR value of these parameters is about 10% in an actual patient anatomy. If, however, accurate dielectric parameters

for fat are utilized this value is about 6%. Since in the neck no fat is modelled we estimate the accuracy of the SAR distribution at this 6%. The worst case estimation for the RD distribution therefore is 12% global difference. This estimation is useful only for global values: it cannot be used for local influences.

Calculations for every structure and average dimensions at a lower resolution (2.5 mm for Δx and Δy and 1 mm - 5 mm for Δz) are carried out in order to assess the influence of the results on the grid size. Comparing the results of the 2.5 mm with the 1 mm resolution we find for the differences: $\Delta\overline{\mathrm{RD}} < 2\%$, $\Delta\mathrm{RD}_{max} < 11\%$ and $\Delta\mathrm{SAR}_{50\%} < 0.2$ cm^2 (1.4%). This means that the 50% iso-SAR pattern is almost independent of this grid size change and that the influence on the RD values is small. The influence of the subcutaneous fat layer is neglected in this study. To investigate the effect of such a layer we carried out calculations with a 3 mm thick fat layer at the transition between the muscle and water environment. The conclusion from these calculations are that, due to increased reflections, the amount of SAR is decreased : $\Delta\overline{\mathrm{RD}} = -12\%$, $\Delta\mathrm{RD}_{max} = -18\%$ and $\Delta\mathrm{SAR}_{50\%} = -0.3$ cm^2, but the pattern remains intact for all structures and thus σ remains approximately equal ($\Delta\sigma = -0.3\%$). The total amount of SAR in the cylinder is reduced $\sim 14\%$ after inclusion of this fat layer.

3.4.2   SAR and RD distributions: trends and clinical translation

With respect to the clinical translation this investigation forms a first step into the systematic investigation of the parameters that influence the quality of an HT treatment of H&N tumours. Subsequent steps will consist of investigations into 3D-anatomy distorting influences and the influences of the applicator, i.e. antenna ring(s) and waterbolus. From these results, the main treatment influencing parameters can be identified and used as an aim for the design of an applicator.

For the muscle calculations it is found that a $\lambda/3$ in diameter central hotspot is created by eight circumferentially placed dipole antennas. This is in agreement with literature values for the central hotspot in muscle[30,105].

The influence of the trachea and spine on the SAR pattern is found to be large. The influence of the trachea is mainly local but the spine has a more global influence, i.e. it spreads the central hotspot from $\lambda/3$ in diameter to approximately $2/3\ \lambda$. This value ($2/3\ \lambda$) is in agreement to calculations, carried out by Guy *et al.*[30], at 915 MHz using an anatomy, which are verified with measurements. The location of the first region of low SAR, seen from the center, is identical to the results of Guy *et al.*[30] as well: $2/3\ \lambda$ for the muscle cylinder, $\lambda/2$ for the layered bone-muscle-fat cylinder. The difference lies in the fact that for this work a plane wave illumination from four sides is used and therefore the superficial absorption by closely positioned antennas is not modelled. The resemblance of the central phenomena does agree

with the finding that the shape of the structures is of moderate importance but that its position in the SAR pattern and its dielectric contrast are of high importance.

433 MHz is used as operating frequency in this study, which has a major effect on the results. The pattern in the neck is highly determined by the wavelength and the dielectric properties of the tissues, thus by the operating frequency. This study indicates that 433 MHz is a suitable choice since its penetration depth is sufficient for large structures but still phase and amplitude steering are possible due to a single central hotspot in all set-ups. This finding is concluded as well from SAR measurements in muscle phantoms at 400 MHz and 915 MHz[29]. This conclusion however needs confirmation by calculations with a 3D anatomy since 1) the influence of fields reflected at higher and lower structures and at oblique transitions are not included in this study and 2) a symmetrical set-up is used for the calculations.

With respect to the design of the future clinical H&N applicator we found little evidence of disturbing effects that would restrict any specific applicator design. We found a minor indication that the only avoidable, undesired, increase of the SAR is located at the trachea. Further, no evidence is found of a limiting change of the SAR in the spinal cord, which is a highly relevant issue because of the potential of neurotoxicity. This study indicates that a cylindrical muscle phantom with a bony spine insert is a suitable configuration for fast and simple inter-antenna performance comparisons and provides good opportunities for experimental verification.

3.5 Conclusions

From this study it is found that the anatomy at 433 MHz, and especially the conductivity distribution, has a major impact on the SAR distribution in the neck: up to $\sim 11\%$ global (mean) relative difference and a standard deviation from the mean of up to ~ 80 % with respect to a muscle cylinder. Central, low in conductivity, structures cause the 50% iso-SAR contour to be widened and have a local influence of up to $\sim 270\%$. The focal region is changed from a circular to a more donut shape following the conductivity distribution in the neck. This effect is almost independent of the dimensions of the neck and the outer contours of the structures. The 50% and 75% iso-SAR contours remain identical for changing dimensions up to a threshold from which the path lengths in tissue from the antennas towards the center of the neck become to large with respect to the penetration depth.

The results in this study are obtained with use of an extruded semi-2D elementary shape-fit phantom. Further study with 3D set-ups is necessary to investigate the influence of 3D structures on the SAR pattern. This study however forms a first step towards the understanding of the complex influences of the various parameters on the SAR pattern in the head and neck and the design of a specific EM-applicator for heating H&N tumours.

Acknowledgements

CHAPTER 4

Optimization of a multi-ring antenna array set-up

Abstract

Purpose: Investigation into the feasibility of a circular array of dipole antennas to deposit RF-energy centrally in the neck as a function of: 1) patient positioning, 2) antenna ring radius, 3) number of antenna rings, 4) number of antennas per ring and 5) distance between antenna rings. **Materials and methods:** *Power absorption (PA) distributions in realistic, head and neck, anatomy models are calculated at 433 MHz. Relative PA distributions corresponding to different set-ups were analysed using the ratio of the average PA (aPA) in the target and neck region.* **Results:** *Enlarging the antenna ring radius from 12.5 cm to 25 cm resulted in a ∼ 21% decrease in aPA. By changing the orientation of the patients with respect to the array an increase by ∼ 11% was obtained. Increase of the amount of antenna rings led to a better focussing of the power (1 → 2 / 3 : ∼ 17%). Increase of the distance between the antenna rings resulted in a smaller (more target region conformal) focus but also a decreased power penetration.* **Conclusions:** *A single optimum array set-up suitable for all patients is difficult to define. Based on the results and practical limitations a set-up consisting of two rings of six antennas with a radius of 20 cm and 6 cm array spacing is considered a good choice providing the ability to heat the majority of patients.*

4.1   Introduction

Hyperthermia (HT) applied to advanced, unresectable, head and neck (H&N) carcinomas, and their lymph node metastases, has a high potential to improve the results of currently existing treatment strategies[20,79,90,94,95]. Hereto equipment is warranted that enables application of an adequate heating pattern to this region. To the best of the authors knowledge, such equipment is available only for heating depths up to 4 cm. Further, these superficial applicators provide only limited possibilities to adjust the specific absorption rate (SAR) pattern. Since we aim at heating both the primary tumour and lymph node metastases, we need to design a specific H&N HT applicator to achieve an optimal treatment. This novel applicator must provide a high degree of control of the SAR deposition pattern that should result in a high quality of the HT-treatment as shown by Wust *et al.*[107].

In earlier work[72,73] we have investigated the dependence of the SAR pattern on a selection of basic design criteria: such as frequency, number of antenna elements and anatomy. In these studies we demonstrated that due to circular symmetry of the neck anatomy a circular array of antenna elements is to be preferred. Further it was shown that the optimal frequency is highly dependent on the target volume to be treated. Based on the expected target volumes for HT in the H&N region, we selected 433 MHz as the most suitable frequency. This frequency provides a

good focussing of the energy and relatively low-priced equipment is available for this frequency. Finally it was demonstrated that six to eight antennas on a circular ring are sufficient to obtain focussed central heating for neck diameters up to 12 cm. For neck diameters larger than 12 cm the focus intensity decreases but in general sufficient energy is deposited at depth.

In this paper we report on the results of a theoretical study that essentially is a follow-up of these earlier studies. In the present theoretical investigation the focus firstly is on selection of a more realistic antenna arrangement, i.e. a single optimal and easily applicable antenna ring radius for all neck anatomies. This is carried out by numerically investigating the SAR focussing as a function of antenna ring radius, i.e. the distance from the antennas to the patient is step-wise increased. Secondly, the aim is to investigate the opportunities that multiple antenna rings provide for axial SAR focussing. The investigation is performed by the calculation of 3D power absorption (PA) distributions in two realistic head models. The goal is to develop an applicator that provides the flexibility to efficiently heat superficial target areas as well as more deeply located target volumes. Further, it should enable steering away from critical organs avoiding toxicity[33]. Again, we assumed that the ability to obtain a high PA at the center of the neck will be the most challenging and difficult problem to solve. As a consequence, we consider that if adequate heating can be obtained for centrally located target volumes then phase and amplitude PA steering can effectively be used to heat lateral target volumes. Therefore, in this theoretical study, we have focussed on investigating the dependence of the PA at the center of the neck as a function of the arrangement of a multi-ring antenna array.

4.2   Materials and methods

The antenna arrangement that provides the optimum PA pattern, and the highest efficiency, varies between patients, tumour locations and tumour volumes. Further, the location and orientation of the patient with respect to the antenna array can have a major influence. Investigating all above mentioned variables and their combined effects is obviously a vast task. To restrict the number of simulations, we split our investigation into two series of calculations with growing complexity. Parameters of interest for each series of investigations were:

- First series:

  - Patient positioning ("RT position" vs "HT position")
  - Antenna ring radius ("R")

- Second series:

  - Number of antenna rings
  - Number of antenna elements per antenna ring
  - Distance between the outer antenna rings ("D")

The aim of the first series of calculations was to explore the influence of the antenna ring radius, aiming to find a single diameter for all anatomy sizes. Hereto we started with a set-up of eight antenna elements that are equally spaced on an imaginary ring around the neck, and investigated the influence of the radius of the antenna ring on the PA pattern. Simultaneously, we investigated the effect of patient positioning. From the first series of calculations we selected the antenna ring radius and patient positioning for further investigations. The second series of calculations was dedicated to the number of antenna rings, the amount of antennas per ring and the distance between these antenna rings.

4.2.1   Anatomy and antenna arrangements

Previously, we examined CT-scans of eight patients that underwent radiotherapy (RT) at various locations in the head and neck region and we determined the minimum and maximum diameter of the neck[73]. These results where used to select two patients with respectively the smallest (radius $\sim$ 4.95 cm: "small patient model") and largest neck (radius $\sim$ 6.75 cm: "large patient model") from this subgroup. Further, these patient can be regarded as the "most easy" and "most difficult" patient anatomy since they were a skinny patient with a long neck ("small patient model") and a fatty patient with a short neck ("large patient model"). The small patient had a carcinoma in the larynx and the large patient a nasopharynx carcinoma. A CT-scan of these patients was used to segment two head and neck tissue models. These patients are assumed to represent the extents of the group of patients in terms of heating in the neck, i.e. results are expected to be representative for the entire group of patients. Both models contain over ten tissue types (Table 4.1). The CT-scans contained anatomy information from the shoulders up to the nose for the small patient and from the shoulders up to the crest for the large patient. By comparing the PA patterns in patient models with and without an artificial extension we found that the truncations affect only the PA values within $\sim$2 cm from the truncation. Figure 4.1 shows the tissue distributions of both anatomy models.
In [72] we found that 433 MHz is within the optimum range of frequencies for an eight dipole antenna set-up and that the array should be rotated 22.5° with respect to the

a) Small patient model
(3D view)

b) Small patient model
(Sagittal cut, x=0)

c) Large patient model
(3D view)

d) Large patient model
(Sagittal cut, x=0)
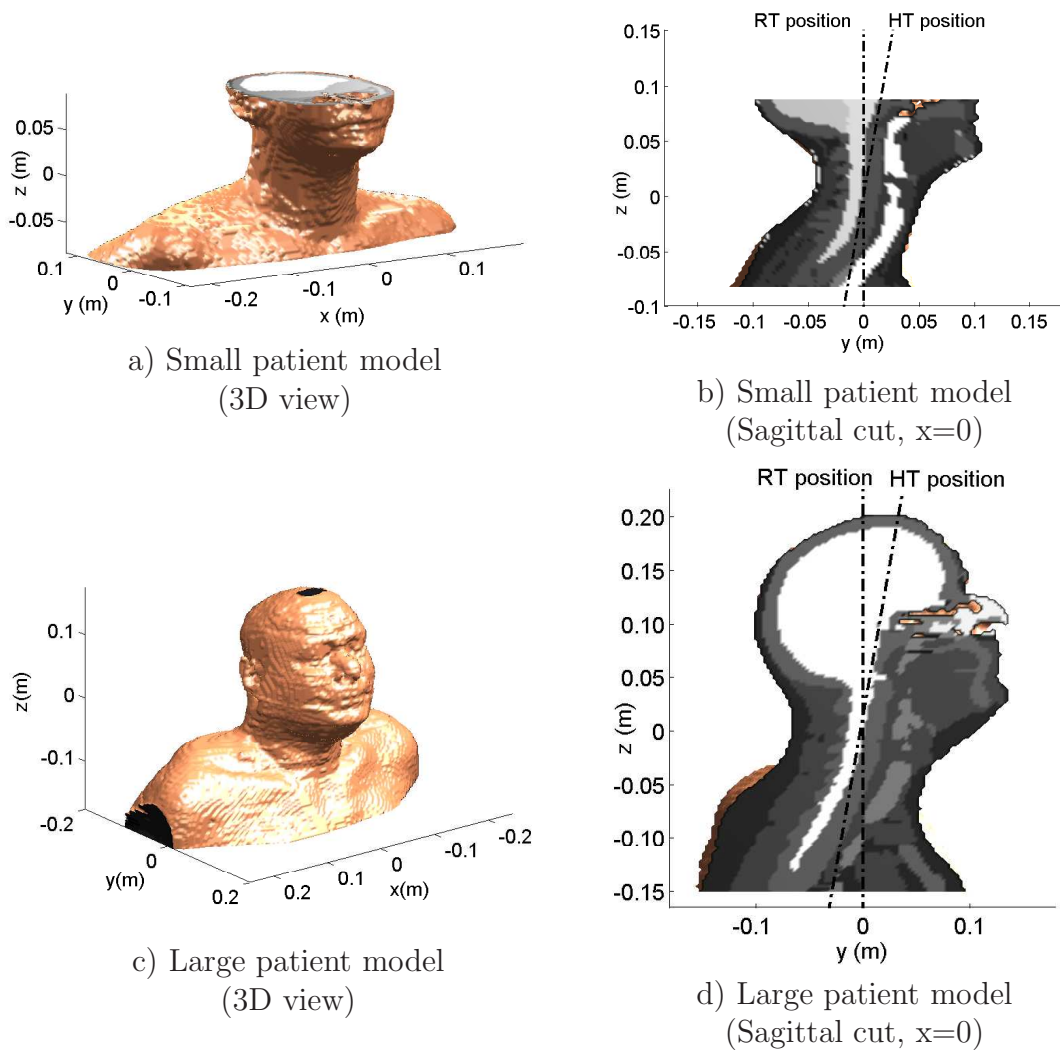
Figure 4.1: 3D view (a,c) and sagittal cuts (b,d) of the tissue distribution of the two head models. b) and d) show the RT position and an indication of the HT position (10° rotation).

Table 4.1: Dielectric properties at 433 MHz of the tissues types corresponding to the two head models ($\mu_r = 1.0$).

Tissue type	ϵ_r [-]	σ_{eff} [S/m]
Demineralized water	78	0.04
Trachea	1	0.00
Fat	6	0.04
Muscle	57	0.81
Bone$_{Cortical}$	13	0.09
Air bubble	1	0.00
Lung	1	0.00
Tooth	13	0.09
Cartilage	45	0.60
Brain$_{Grey}$	57	0.75
Brain$_{White}$	42	0.45
Skin$_{Wet}$	46	0.68
Gland	61	0.89
Eye	58	1.01
PEC	1	$1*10^6$

chin to avoid hotspots at the chin. In Figure 4.4a we present the set-up to investigate the influence of variation of the antenna ring radius R on the absorption pattern in the neck. A minimum radius of 12.5 cm was used to ensure that both anatomies are located in the far field of the dipoles ($\sim \lambda/2$). This radius was enlarged to 25 cm in steps of 2.5 cm to obtain the required minimum distance between the tissue surface and the antenna elements. Simultaneously, we investigated the effect of a ten degrees rotation of the array with respect to the patient around the x-axis (left→right): **"RT position"** vs **"HT position"** (see Figure 4.1 and 4.2). The RT position conforms to the RT treatment position and the HT position is considered optimal for a HT treatment. We chose a ten degrees rotation (around the x-axis) because this leads to a smaller neck cross-section and aligns the spinal column of the patient with the central axis of the applicator.

Using the selected antenna ring radius and anatomy rotation angle, the second series of calculations addressed the potential of multiple antenna rings. As a starting point we used set-ups with six and eight antennas and investigated the benefit of set-ups consisting of two or three antenna rings. We further changed the distance between the outer antenna rings (D in Figure 4.2) stepwise from 0 to 10 cm. With multiple rings at a suitable distance we expected to obtain a more axially focussed absorption pattern and axial steering possibilities. In practice, the maximum amount of antennas is restricted to twelve since this amount of 150 Watt amplifiers, operating at 433 MHz, is available in our unit. This leads to set-ups of two rings of four ("2x4")
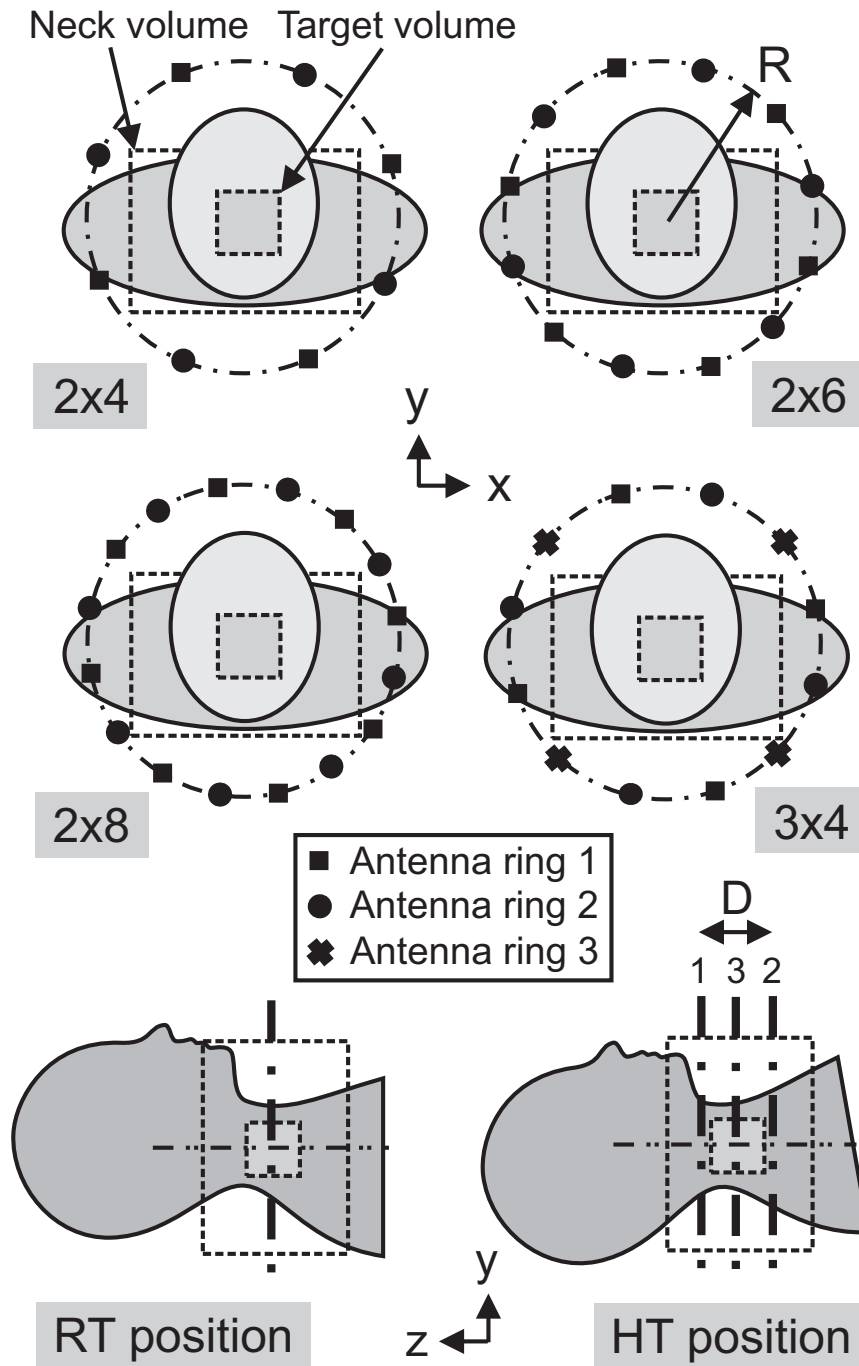
Figure 4.2: Schematic representation of the antenna ring arrangements (2x4, 2x6, 2x8 and 3x4) and schematic sagittal cross-sections of the RT position and the 10° rotated (around the x-axis) HT position.

and six ("2x6") antennas and three rings of four antennas ("3x4"). Nevertheless, two rings of eight antennas ("2x8") arrangement was investigated as well to quantify the relevance of a possible extension to more antennas and amplifiers. The arrangements are schematically shown in Figure 4.2. Note that we applied a symmetrical rotation of the set-ups around the z-axis with respect to the chin. Further note that the 2x4 arrangement with 0 cm distance is equal to a 1x8 arrangement.

4.2.2 Electromagnetic modelling

We predicted PA distributions in both patient models by computing the electromagnetic field using a finite-difference time-domain (FDTD) based program[*]. PA was defined as:

$$\text{PA} = \frac{\sigma_{eff} \, |\overrightarrow{E}|^2}{2}, \quad (W/m^3) \tag{4.1}$$

where σ_{eff} is the effective electrical conductivity (S/m) and $\overrightarrow{E}$ is the complex electric field vector. Note that the PA values differ only by the tissue-dependent mass density from specific absorption rate (SAR) values. Mur's second-order absorbing-boundary conditions (ABC) and additional extra voxels of exterior are applied to eliminate the influence of reflections at the boundaries of the computational domain. The dimensions of the, in total 2.5M, voxels were 2.9, 2.9 and 2.5 mm ($\Delta < \lambda/25$). The dielectric properties of the tissues (Table 4.1) were assumed isotropic and were found using a parametric model by Gabriel *et al.*[26]. The dielectric properties of the trachea are chosen equal to those of air. The properties of the de-mineralized water (salinity = 0 g/l, T = 20°C) in the waterbolus are found in a publication of Stogryn[88] and one of the ESHO taskgroup comittee[11]. Dipoles were approximated by two straight conducting wires (PEC material, Table 4.1) with a cross-section of one voxel (2.9 mm x 2.9 mm). The length of the dipole antennas (L_{dip}) was chosen such that they are resonant at 433 MHz in water, i.e. 3.75 cm. Excitation was obtained by a suppressed electric field at the gap between both wires. For the investigations we always excited the sources with equal phases and amplitudes since this is expected to result in a central absorption focus. In the entire study, phase and amplitude optimization has been omitted because little improvements are expected for this symmetrical antenna arrangement and almost symmetrical patient anatomy in the axial plane[73]. For the set-up with three rings this approach introduced a small error of 9 degrees phase mismatch between the middle and outer rings for central steering. The result of such a small phase difference, however, has a minor impact on the aPA ratio as it only slightly affects the focus at its axial extents that are not within the target area. The waterbolus is modelled by an infinite de-mineralized water environment since investigation of the effects of the waterbolus was beyond the scope of this investigation.

---

[*]FDTD program developed at TNO, The Hague, The Netherlands.[9,101]

4.2.3   Evaluation

Simulated PA patterns were analysed qualitatively by comparing visualizations of cross-sections through the origin of the applicator, i.e. through the planes $x = 0$, $y = 0$ and $z = 0$. These plots visualize PA values that are normalized to the average value in the neck region. For quantitative evaluation we defined the average PA ratio that quantifies the average amount of power that is absorbed in the target region with respect to the average amount in the neck:

$$\text{aPA ratio} = \frac{\overline{PA}_{tgt}}{\overline{PA}_{nck}}, \tag{4.2}$$

where $\overline{PA}_{tgt}$ is the mean power absorption value in the target region and $\overline{PA}_{nck}$ is the mean power absorption value in the neck region. The aPA ratio effectively quantifies the global shape of the PA pattern. For this analysis we introduced a centrally located hypothetical target volume with realistic content in both anatomies as shown in Figure 4.2. Target volumes of 4 cm x 4 cm x 4 cm (0.064 dm^3), 5 cm x 5 cm x 5 cm (0.125 dm^3) and 6 cm x 6 cm x 6 cm (0.216 dm^3) are investigated because the aim is to treat advanced tumours. Results are shown only for 5 cm x 5 cm x 5 cm since observed phenomena were similar for all three target volume sizes. The height of the neck volume was 16 cm (small anatomy) or 20 cm (large anatomy) to incorporate the PA values up to the chin and shoulders. High local PA values ("PA hotspots") were found at these sites in the previous investigation[72] and these effects are potentially decreased by a proper set-up with multiple antenna rings. This larger neck volume means that the aPA values will be higher than in previous publication since more low values are included in the neck volume and as a consequence the average PA in the neck volume will be lower.

4.3   Results

4.3.1   First series: ring radius and patient model orientation

Figure 4.3 shows a sagittal, transversal and coronal cross-section of the PA distribution in the large patient model corresponding to two set-ups: 1) one ring of eight dipoles ("1x8") and 2) two rings of six dipoles ("2x6"), both with a radius of 20 cm.

The transversal cross-section of the 1x8 set-up clearly shows a central region of high PA: the central focus. This central focus quite nicely fits in the inner white square: the target region. The sagittal and coronal view confirm this central focus but reveal that the axial focus length extends to the outside of the target volume. Further it shows regions of high PA in tissue outside the target region ("PA hotspots") at the
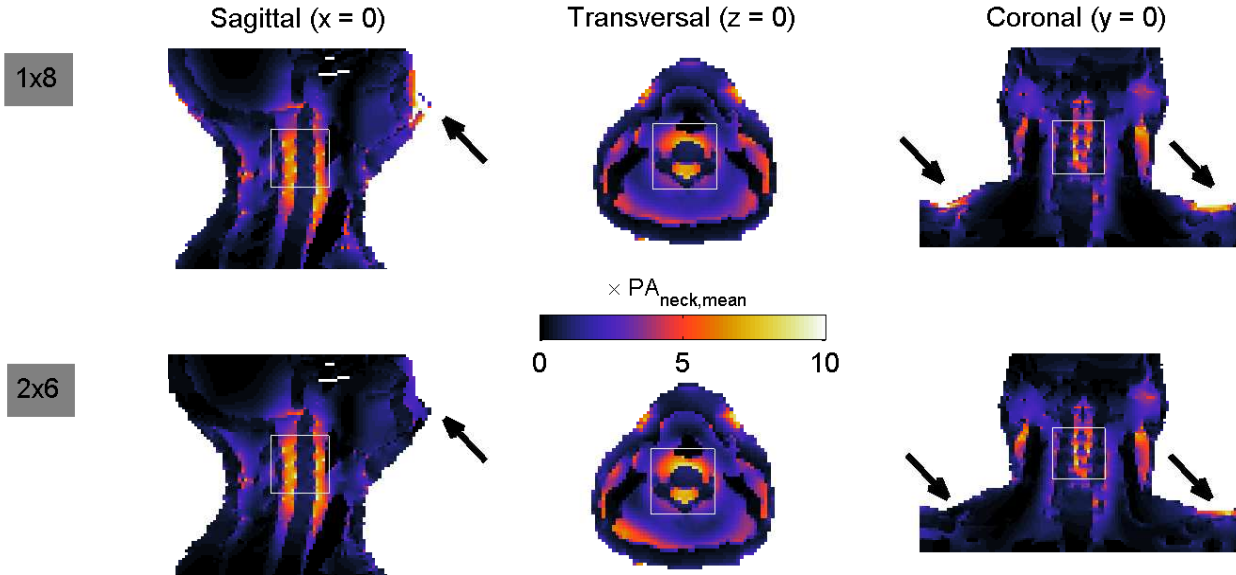
Figure 4.3: Cross-sections of the PA distributions in the large patient model in HT position for one ring of eight dipoles (1x8, R = 20 cm) and two rings of six dipoles (2x6, R = 20 cm, D = 6 cm). Black arrows indicate the locations of PA hotspots (1x8) or corresponding locations where these hotspots are reduced (2x6).

chin and shoulders. The locations of these hotspots are indicated because they are poorly visible.

Figure 4.4 visualizes aPA ratios as a function of applicator ring radius (1x8 set-up) for a small and large patient model in RT and HT position. The aPA ratio is found to decrease about 21% for arrangements with increasing radii. An increasing radius leads to a larger focus length (z-direction) so relatively less power is deposited within the 5 cm of the target region. The slopes of the curves depend on the choice of the neck volume, but the shape is comparable for different volumes. A radius of 20 cm is selected for the clinical applicator so all antennas are sufficiently far away for all patients and for ease of patient positioning. The figure also shows that the HT position leads to favourable aPA ratios compared to the RT position for the small (+5%) and large (+18%) patient model. Hence, a PA pattern is obtained with a more pronounced central focus and a lower sensitivity to the neck diameter. This more intense focus is the result of a smaller neck cross-section in HT positioning (perpendicular to the spine, see Figure 4.1). From these results we chose the HT position as optimum and hence used the HT position and a radius of 20 cm for further calculations.
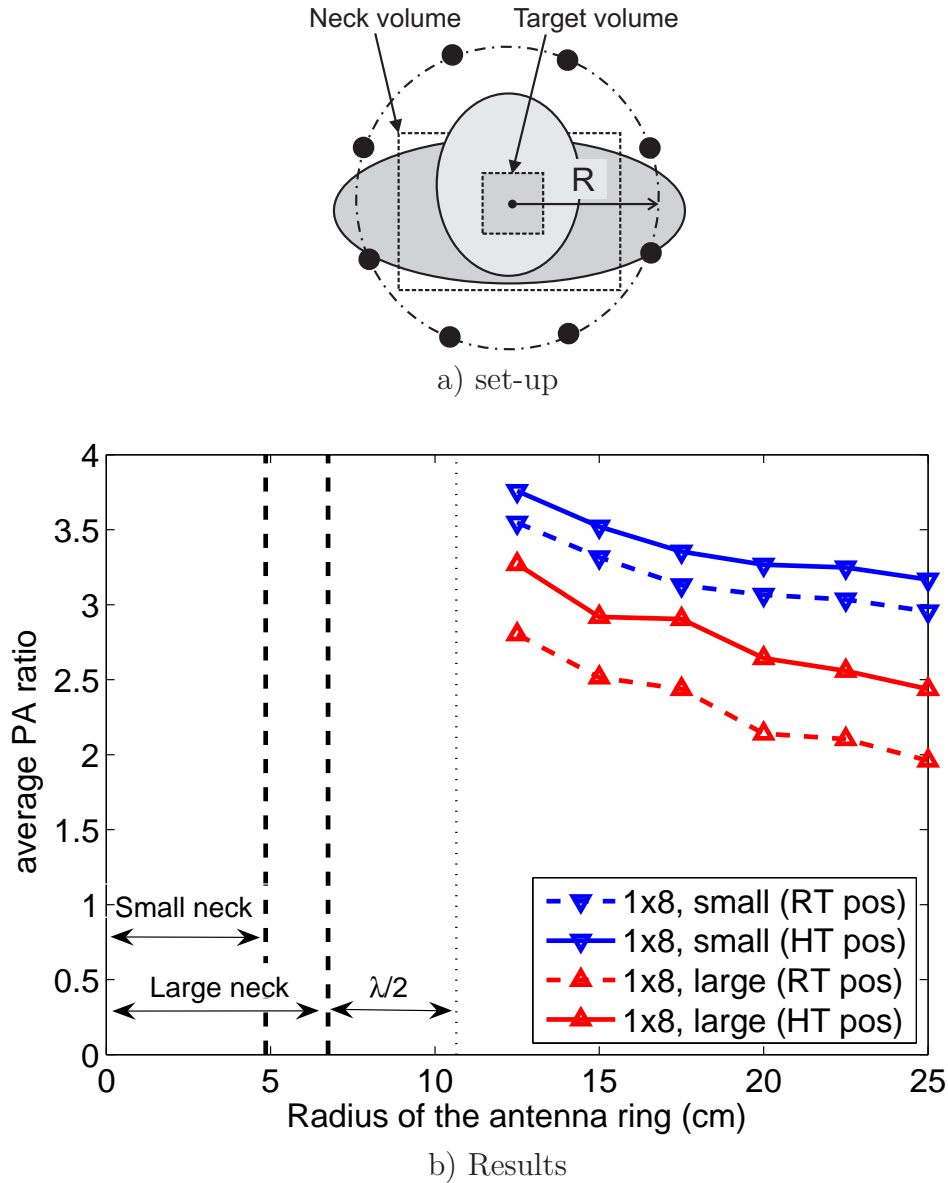
a) set-up

b) Results

Figure 4.4: Average PA ratios as a function of antenna ring radius for a set-up of
eight antennas: set-up a) and results b). Curves correspond to results
for a small and a large patient model in RT and HT (10° rotation
around the x-axis) position. The average radius of these models and
the near-field distance ($\lambda/2$), where the dipole antennas should not
be placed, are indicated.

4.3.2 Second series: number of rings, amount of antennas per ring and ring distance

When enlarging D we found for all array arrangements that the central focus becomes smaller in the axial direction and more and more conforms to the target region. When the distance D becomes too large, the intensity of the focus is hampered by insufficient penetration of the electromagnetic waves due to an increasing path length. Further, the PA hotspots at both shoulders reduce for all arrangements when D is enlarged up to a maximum of 8 cm. These effects are exemplified by Figure 4.3, which shows PA distributions for 1x8 and 2x6 configurations. The main difference between the PA patterns of both set-ups are the PA hotspots at the chin and shoulders for the 1x8 set-up that are reduced in the 2x6 set-up: this effect is indicated by the arrows. For both set-ups we found a central focus that is modulated by the anatomy distribution. The PA pattern, however, is somewhat more focussed by using two rings, however, it is difficult to notice this effect on the base of PA visualizations.

Figure 4.5 visualizes the aPA ratios for all antenna arrangements, all distances and both anatomy models. For an increased antenna outer ring distance, it quantifies the previously mentioned effects: an increase of focus but a decrease of intensity at the target region. The figure shows that extending the amount of antenna rings from one to two or three results in ∼15% (small patient) to ∼19% (large patient) more power absorption at depth. Three out of four aPA ratio curves show their highest values for the set-ups with D=0 cm. The aPA of these curves, however, is relatively stable until a certain threshold distance where the decrease becomes much steeper. This effect is less prominent for a 3x4 set-up but in this case the third central ring is not moved (see Figure 4.2). For a 2x8 set-up, maximum focussing is not obtained at D=0 cm because each ring of eight antennas provides optimum PA intensity at the target region on its own but the focus in z-direction conforms best to the target region for ring distances around 4–6 cm. All curves are positively correlated with the total amount of antennas. For small distances (< 6 cm) the aPA values indicate a 20% increase in focussing from eight to twelve antennas and an additional 10% increase for a 16 antenna set-up.

4.4 Discussion

As we explained earlier[73], the causes of the perturbations on the SAR distribution of a phased array hyperthermia applicator device can be clustered into three groups. From inside to outside these are: 1) anatomy, 2) antenna array and 3) waterbolus related distortions. We chose to investigate these parameters independently to gain more understanding of their, sometimes opposing, effects on the PA pattern. In the present study we dedicated our attention to extending earlier work that has been done on the second step[72]. Of course, it is difficult to separate waterbolus related

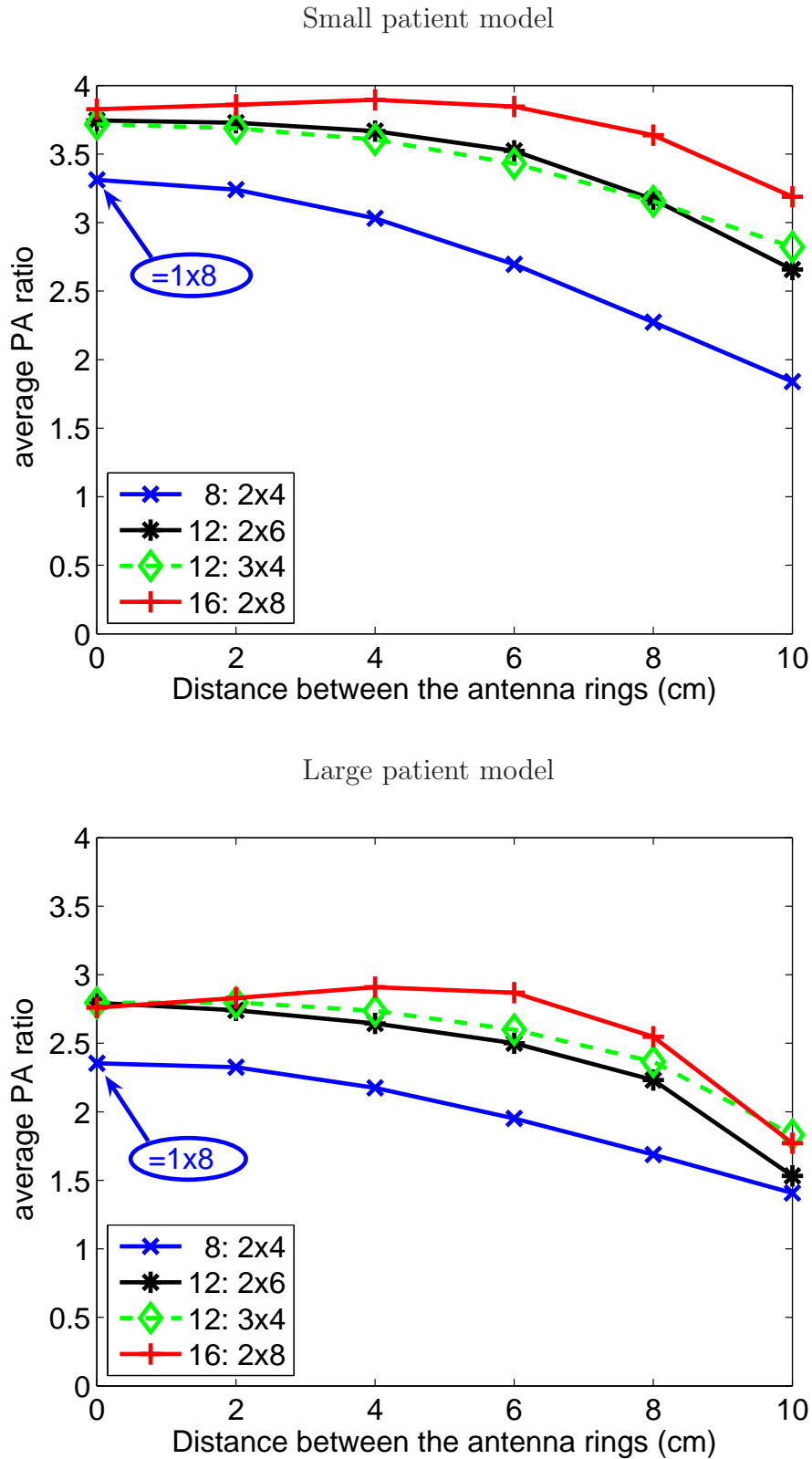Small patient model

Large patient model

Figure 4.5: aPA ratios for different distances between the outer rings. Curves are shown corresponding to the 2x4, 2x6, 2x8 and 3x4 arrangements.

influences from array related influences, especially at bolus-air transitions[16,38]. However, waterbolus shapes are difficult to prescribe clinically and they highly depend on practical limitations. Further, effects from waterbolus edges that are present in many calculations due to straight edged models are expected to reduce due to more round shapes in the clinical practice. Therefore we chose to investigate antenna array effects and postpone studying effects of the waterbolus edges.

To perform the study within an acceptable period and to avoid an enormous amount of calculations, we simplified the problem by investigating only the ability of a circularly symmetric antenna arrangement to adequately heat a centrally located target region. Exploiting the high amount of symmetry of this set-up it was reasonable to use central phase and amplitude settings. Further, we assumed that the variation in aPA due to different patient anatomy locations is much larger than the variation due to suboptimal phase and amplitude settings. In a previous study[72] we have investigated the influence of the choice of frequency on the PA pattern by using a single anatomy model. The frequency has a huge effect on the PA pattern (two fold increase in focussing) and, for that study, one anatomy model and scaled versions were sufficient to represent the entire group of H&N patients that apply for RT. In this study we expected smaller differences and we therefore used two anatomy models that represented the extremes of the subgroup of H&N RT patients, i.e. a small patient and a large patient. The simplifications to the phase and amplitude optimization and anatomy models led to a considerably reduced computational effort while still a high predictive value for the optimum set-up for this group of patients can be expected. Phase and amplitude optimization, however, is expected to be inevitable to effectively steer the central focus to a non-central target region and is useful to further reduce hotspots per individual patient. These effects will be the subject of a subsequent study when the applicator is routinely used for clinical treatments giving us the opportunity to perform patient specific treatment planning. For this study we analyzed CT scans of eight patients and selected the "most easy" and "most difficult" patient anatomy, i.e. a skinny patient with a long neck ("small patient model") and a fatty patient with a short neck ("large patient model"). We faced some difficulties to determine the optimum axial location of the array around the large patient's neck while trying to keep sufficient distance between all antennas and patient model's skin. In the first attempt large PA hotspots were visible, especially at the shoulders for set-ups with D > 6 cm. These hotspots where also reflected in steeper and less straightforward aPA curves. These problems, however, were less prominent in HT position compared to RT position. An improved placement, i.e. a shift in cranial direction, led to less hotspots and more predictable aPA curves.

This investigation is a follow-up of the study reported in a previous paper[72] and forms the step from that theoretical parameter study to an actual applicator antenna array set-up. In that study we selected an array of six to eight antennas operating at 433 MHz as optimum arrangement for a single ring, H&N, HT applicator. In the present study we found that more than eight antennas yields better focussing, thus

better aPA values. The reason for this different result is that by increasing the neck volume we now also incorporate the effects of PA hotspots at chin and shoulders that are reduced by the increased amount of antennas in the current study.

Earlier investigations used phased-array approaches to apply superficial hyperthermia with planar or conformal arrays[45,56]. Experimental work by Gross et al.[29] showed the potential of cylindrical phased arrays for heating tumours in the neck using four waveguide horn antennas applied to a neck-sized cylindrical muscle-phantom. However, to the best of the authors' knowledge, no clinical phased-array based applicator for applying hyperthermia to deep-seated head and neck tumours exists. Moreover, this is the first attempt to use 3D calculations for a parameter optimization of a (circular) phased-array applicator specifically designed for deep heating in the H&N region.

For deep hyperthermia (DHT), the use of circular phased-array applicators has a long history[91,100] and the application is to a certain extent comparable. A prominent difference that hampers comparison is the concave shape of the neck whereas the pelvis is more convex shaped. This concave shape results in more strict limitations on the distance between outer rings ($\sim$8 cm as found in this study) where for DHT that dilemma is not that an important issue. Further, the neck has the advantage that it is more cylindrically symmetrical. As a consequence, SAR pattern optimization by phase steering is expected to be more straightforward.

The influence of multiple antenna rings for DHT was previously investigated theoretically by Seebass et al.[83], Paulsen et al.[77] and Kroeze et al.[50] for their deep hyperthermia systems consisting of three[50,83] or four[77] rings of antennas at predefined positions. Paulsen et al.[77] conclude from their results (power based optimization) that increasing the number of antennas per ring in many cases is more favourable than increasing the number of antenna rings. A similar conclusion is drawn by Seebass et al.[83] for their power based optimization, but they found the reverse effect for the temperature based optimization. They explain this phenomenon by deviating between obtaining a proper focus at the target region with positive interference (power optimization) and the decrease of hotspots by negative interference (temperature optimization). Seebass et al[83] further conclude that a large amount of antennas per ring should be avoided because this results in a high sensitivity of the PA pattern to small amplitude and phase shifts. Kroeze et al.[50] compared a set-ups of multiple waveguide slot antennas for heating in the pelvic region. For this convex region they conclude that a 3x4 arrangement outperforms a 2x6 arrangement. Together these three studies agree with the current results that twelve antennas are sufficient for SAR pattern steering and that it is difficult to discriminate between a 3x4 and a 2x6 set-up.

The influence of the distance between two arrays for deep HT is previously experimentally instigated by Crezee et al.[13]. They started with their AMC-4 set-up, consisting of one ring of four waveguide antennas, and added an extra ring ("AMC-8") and varied the inner-ring distance. In contrast to our findings, they found by phantom measurements that the effective length ($L_{50\%}$: axial dimension of the 50%

iso-SAR volume) increased for an increased ring distance. The reason for this difference is the much smaller relative distance between the antennas and the patient for the AMC-8 system ($\sim 0.25\lambda$) compared to our set-up ($\sim 1.5\lambda$). In a separate study in cylindrical phantoms (results not reported) we found that a small distance between the patient and the antennas results in a small $L_{50\%}$ and thus a poor interference between the two antenna rings. In the extreme case of exposure of a muscle cylinder by a circumferential plane field, $L_{50\%}$ will reach ∞, providing the waves have sufficient penetration depth.

4.5   Conclusions

In this theoretical study we have focussed on investigating the dependence of the PA at the center of the neck as function of the arrangement of a multi-ring antenna array. Parameters of interest were: 1) patient positioning 2) antenna ring radius 3) number of antenna rings 4) number of antenna elements per antenna ring 5) distance between the outer antenna rings.

We found that a rotation of ten degrees of the antenna array with respect to the patient results in a better heating at depth ($\sim 11\%$). This rotation further aligns the spinal column to the central antenna array axis, thus steering the central focus away from the spinal column by means of phase and amplitude adjustments is more straightforward. aPA values decreased ($\sim 21\%$) when increasing the antenna radius of a 1x8 set-up. Mechanically, a radius of around 20 cm was experimentally found to fit best around the neck: thus we chose this smallest, practical, radius.

Investigations into an array with over eight antennas for this H&N heating application revealed an increase of around 17% in aPA for D = 0 cm. It is difficult to choose the best performing set-up (2x6 or 3x4) that matches our twelve, clinically available, amplifiers since only small differences in power focussing at depth are found. Furthermore, results are modulated by the array distance. Globally, the increase in penetration at depth of multiple rings diminished when the antenna rings where positioned at distances over 6 cm. We chose to use two rings of six antennas because of its high intuitive steering (compared to a 3x4 set-up) and an inner-ring distance of 6 cm for maximum axial (z-direction) SAR steering possibilities. Increasing our clinically available amount of amplifiers to 16 (2x8 set-up) would result in a 10% increase in focussing at depth when D = 6 cm.

Acknowledgements

CHAPTER 5

Design of the patch antenna

Abstract

In this paper we describe a specifically designed patch antenna that can be used as the basis antenna element of a clinical phased-array head and neck hyperthermia applicator. Secondly, we theoretically assessed its electrical properties under clinical conditions. Using electromagnetic simulations we optimized the dimensions of a probe-fed patch antenna design for operation at 433 MHz. By several optimization steps we could converge to a theoretical reflection of -38dB and a bandwidth (-15dB) of 20 MHz (4.6%). Theoretically, the electrical performance of the antenna was satisfactory over a temperature range of 15-35°C, and stable for patient-antenna distances to as low as 4 cm. In an experimental cylindrical set-up using six elements of the final patch design, we measured the impedance characteristics of the antenna 1) to establish its performance in the applicator and 2) to validate the simulations. For this experimental set-up we simulated and measured comparable values: -21dB reflection at 433 MHz and a bandwidth of 18.5 MHz. On the basis of this study, we anticipate good central interference of the fields of multiple antennas and conclude that this patch antenna design is very suitable for the clinical antenna array. In future research we will verify the electrical performance in a prototype applicator.

5.1 Introduction

In previous publications[72,73] we have explained the need for a site-specific design of an applicator that will adequately heat head and neck (H&N) tumours. In an exploratory theoretical study[72] we demonstrated that such a site-specific applicator must consist of multiple antenna elements to provide adequate control of the specific absorption rate (SAR) deposition pattern. We also showed that 433 MHz (ISM frequency in Europe: a frequency allocated for Industry, Science and Medicine) is a suitable frequency for heating H&N tumours with a multi-antenna applicator. In this paper we will address the first step of the applicator design, i.e. the design of a single antenna element.

The problems involved with hyperthermia antenna design are very different from the design of antennas in free space and should not be underestimated[87]. Firstly, the antenna radiates into a lossy medium, which has a considerable influence on the impedance, bandwidth and antenna losses[31,48]. For this reason, the antenna design procedures described in the literature could not be used, since these were developed for a lossless environment (usually air) and simulations have to be verified by measurements. Secondly, the presence of a patient in the near field can also have considerable impact on the reflection characteristics. For deep hyperthermia (DHT), the most common array set-up is a circular or elliptical array of multiple

antennas that are matched to the patient by means of a waterbolus filled with (demineralized) water. The use of a waterbolus requires an antenna design that enables efficient radiation from the substrate material of the patch antenna into the bolus water. In the antenna design proposed in this paper, this problem is solved by using water as substrate material, whereby the patch antenna is submerged in the water. This water can be circulated to cool the antenna, thereby increasing the stability of the antenna characteristics at high power. Another advantage is that a water substrate considerably decreases the optimal size of the antenna compared to that of a configuration with a solid substrate ($\epsilon_r < 20$). The drawback of this approach, however, is that the substrate is lossy and its permittivity will vary with the waterbolus temperature, which is determined depending on the skin-cooling strategy required.

Most DHT[99] applicator designs consist of an array of waveguide antennas ("guide fed slot") or dipole antennas[87]. The first designs utilized water-filled waveguides because they are rigid and require no external matching. Despite the utilization of water-filling, these antennas have a very narrow bandwidth and are relatively large and heavy. Another disadvantage of water-filled waveguides is their relatively strong near-field components[68,102]. These fields extend to the outside of the waterbolus, especially for low frequencies (<433 MHz), leading to hotspots in superficial tissue effectively reducing penetration depth[68]. The problems with high near-fields were solved by a subsequent design utilizing dipole antennas, which are simpler and have a larger bandwidth. Dipoles, however, require an RF-matching network containing a balun[5] to obtain a symmetric radiation field and stable electrical performance. This matching network absorbs a substantial amount of power and thus decreases the efficiency of the antenna.

The need for such a matching network can be circumvented by using a properly designed probe-fed patch antenna operating within the waterbolus. Since the 1970s, patch antennas have received a lot of attention[27] because they are inexpensive, lightweight, easy to construct and can be made to conform to curved structures. They have also been investigated extensively within the hyperthermia community[31,59,93], but mainly for purposes of superficial hyperthermia (SHT) (heating depth ≤ 4 cm). For SHT the most important drawback was the patch antennas' small bandwidth, and the correspondingly large influence of tissue loadings in the close vicinity of the skin on the antenna's reflection characteristics. For DHT, when a minimal patient-antenna distance can be assured, this influence of tissue loadings is restricted. Further, a highly appealing feature of patch antennas is that they can be fed with a simple coaxial cable, requiring no special matching network between antenna and transmission line. When used for a clinical treatment, antennas in which an RF matching network can be avoided have a clear advantage in terms of reliability and reproducibility. The build-up of heat in the matching network, associated with large mismatches of the antenna load, may cause an unpredictable[63,108] and unstable behaviour of the system.

In this work we designed and analyzed a patch antenna for use in a head and neck applicator, where the main parameter under investigation was its reflection characteristic. The resulting patch antenna design was analyzed by extensively exploiting 3D electromagnetic (EM) simulations of various patch antenna set-ups and measurements. The analysis focussed on the sensitivity of the design to the influences of dimensions (length, width, height, feeding position) and to influences under clinical conditions (water temperature, patient, neighbouring patch antennas). The amount of cross-coupling was also estimated using a flat set-up. The antenna design was built in an array setting, and its reflection was optimized by fine-tuning its length. Finally, we conducted measurements on multiple versions of these patches to verify the practical feasibility of the design and to check the accuracy of the simulations.

5.2 Materials and methods

5.2.1 Design requirements

The use of an antenna design within an hyperthermia (HT) applicator leads to some application-specific requirements. The antenna will be embedded in a movable applicator system, hence the antenna should be light, small and robust. Because E-field components perpendicular to the patient skin lead to high power absorption values at fat-muscle transitions[73], a high $E_{///}/E_{\perp}$ ratio at the patient's skin is desired. Furthermore, constructive interference would be optimal for axial electric field components[21]. To reduce power losses in the water bolus ($\sigma_{eff,water} \neq 0$[88]), the antennas should be positioned as close as possible to the patient skin. On the other hand, the distance to the skin has to be large enough to minimize the patient's influence on the reflection characteristics. Further, to avoid an additional matching circuit (extra power losses) which would destroy the initial advantage of the patch antenna, a matched and efficient antenna design was desired. This efficient operation should be possible in the entire range of waterbolus temperatures, which is anticipated to be between 20 and 30°C for this semi-deep HT treatment. For the initial design process we anticipated that optimizing the -15dB bandwidth would result in a design with a low sensitivity of the reflection coefficient to different tissue loadings and sufficient room to cope with the change in resonance frequency due to the changes in waterbolus temperature. We aimed to achieve little cross-coupling because it would increase "reflected power" at other antennas, thus virtually decreasing efficiency.

5.2.2 Application specific configuration

The patch antenna configuration and its most important dimensions are shown in Figure 5.1. The configuration consists of a conducting groundplane with a conducting patch of length L and width W at distance h from the groundplane. The patch is connected, at distance x_f from the width of the patch, to the extending conducting

rod of a C-female receptacle connector. The diameter of the extending rod is 3 mm and the diameter of the surrounding teflon dielectric is 10 mm.
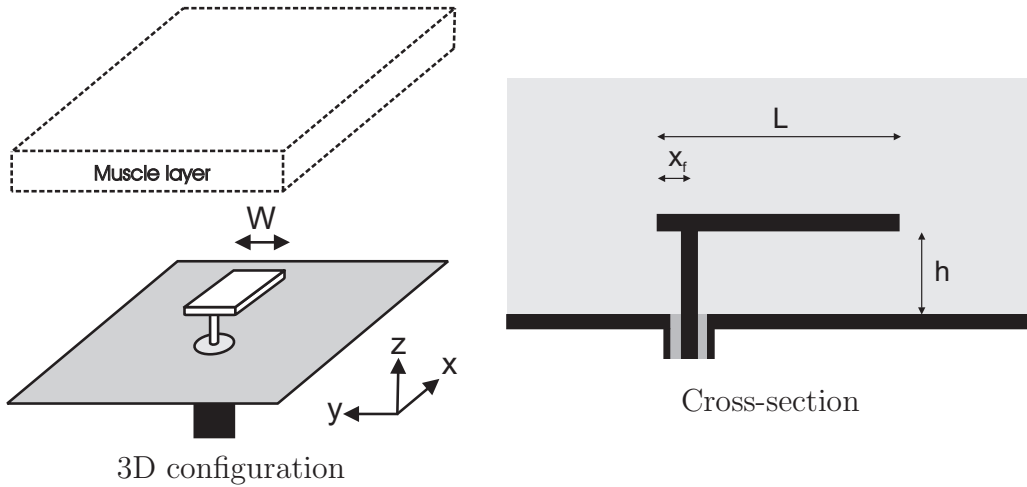
Figure 5.1: Schematic visualization of the patch antenna configuration and a cross-section, with the dimensions that are varied. The "Muscle layer" was present only in the set-ups that were used to investigate influence of a patient on the reflection characteristics.

In this configuration, efficient radiation into the waterbolus is obtained by using water as substrate material, i.e. the patch is submerged in the water. The water will be circulated to cool the patient's skin and, at the same time, this circulating water provides cooling of the antenna's self-heating effects at high power ($\sim$100W). Cross-coupling between antennas is expected to be low in this design because no dielectric transition is present that may enable surface waves. For the first design we used dielectric properties of demineralized water at 433 MHz and 25°C, i.e. ϵ_r (relative permittivity) = 78 and σ_{eff} (effective conductivity) = 0.04 S/m.

5.2.3 EM modelling

Ansoft Designer

The design process was initiated by using Ansoft Designer v2.1[3], a layered 2D method of moment (MoM) based program. The program makes it possible to define infinitely thin Perfectly Electrically Conducting (PEC) and finite dielectric layers; definition of non-infinite PEC structures and a feed of finite size can also be modelled (Figure 5.2). A constrained gradient optimization algorithm was used to optimize the length L, width W and distance of the feed to the edge of the patch x_f for different heights h. To simulate the waterbolus, Layer1 and Layer2 where assigned dielectric properties of demineralized water at 433 MHz[11,88]. For Layer3, we used dielectric properties of muscle at 433 MHz[26]: ϵ_r = 56, σ_{eff} = 0.8 S/m, to simulate
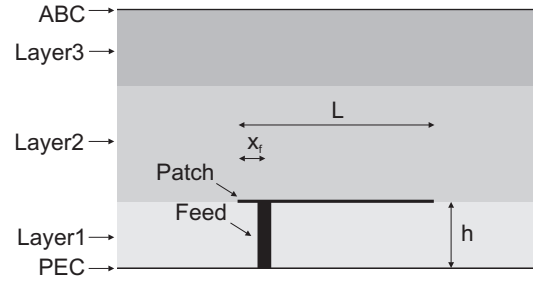
Figure 5.2: Schematic visualization of the layered patch set-up implementation in Designer. "Patch" is infinitely thin and "Feed" has a diameter of 3.0 mm, both are PEC.

the influence of a patient in the design. We further assumed frequency-independent material properties. Layer3 was positioned 50 mm from the patch, i.e. the thickness of Layer2 was 50 mm.

SEMCAD X

The initial design created with Ansoft Designer was further investigated using SEM-CAD X v11.0[84], a commercial finite-difference time-domain (FDTD)[89] based program. For the FDTD algorithm, the entire computational domain must be divided into voxels, i.e. small brick-shaped elements. As SEMCAD X supports a variable grid stepping, grid refinements at small structures can be used to increase the accuracy of the model while retaining acceptable computational times.

The single-patch set-up in SEMCAD X is an implementation of the set-up of Figure 5.1. The combination of connector and connected coaxial cable was modelled using an 8 cm coax with the dimensions of the connector: central conductor (PEC, diameter=3mm) teflon dielectric (ϵ_r=2.08, σ_{eff}=0.46 mS/m). Because modelling of this connection had a considerable impact on the results, we used the most accurate model. Four voltage sources were positioned in the coax, each in a different quadrant, 4 cm beneath the ground plane. These sources were excited with a Gaussian pulse modulated with a 433 MHz sinusoid containing frequencies between 350 and 500 MHz. The resulting E-field pattern in the coax was investigated to ensure that the correct mode was propagating towards the patch. An infinite water environment was modelled by using four or eight layers of Berenger's Perfect Matched Layers (PML)[89] as Absorbing Boundary Conditions (ABC). To extract the energy propagating away from the antenna, eight layers of PML were used at the truncation of the coaxial cable. The size of the computational domain was 20 cm x 20 cm x 22 cm (length x width x height), i.e. the distance from the patch to the ABC was always more than 8.8 cm ($> \lambda_{water}$). The set-up was modelled with gridsteps from 3.2 mm down to 0.06 mm. Refinement down to 0.06 mm at the patch and feed proved necessary because the model appeared quite sensitive to accurate modelling of the coaxial cable. Further the grid-steps at the patch were always smaller than 0.5 mm. This

resulted in a total amount of 3.6 million voxels. Voltages and currents were recorded in the coaxial cable at the location of the ground plane from which the S-parameters were calculated. Transient simulations were terminated after $\sim$ 55ns when signals had sufficiently decayed ($< 0.01\%$), while for harmonic simulations (f=433 MHz) 10 periods were simulated.

As in Designer, the water of the waterbolus was modelled by using dielectric properties of water at 25°C and muscle (ϵ_r=57, σ_{eff}=0.8 S/m) at 433 MHz for all frequencies. The influence of a different waterbolus temperatures was investigated by using dielectric properties of water between 20 and 30°C[11,88]. Variations of the reflection coefficient due to patient distance was investigated by positioning the muscle layer (Figure 5.1) at various distances from the patch antenna. The dielectric properties of this layer were varied as well in addition to investigate the influence of different patients.

Multiple antenna set-up

To investigate the influence of neighbour antennas and the amount of cross-coupling, we created set-ups with two antennas that were always oriented in the same direction. Three arrangements of two antennas were investigated, i.e. horizontal (H-plane), diagonal and vertical (E-plane). The distance between the antennas was always 10 cm, since this is the worst-case distance of the anticipated twelve antennas on a 40 cm diameter ring[75]. The combined influence of a patient was investigated by positioning a muscle layer at infinity (muscle layer absent), 10 cm or 5 cm for all arrangements. The set-ups were also used to determine the amount of cross-coupling (S_{12}) between two neighbours. Hereto we recorded voltages and currents simultaneously at both primary and secondary antenna to be able to calculate S_{11} and S_{12} parameters.

5.2.4 Clinical antenna set-up: measurements and simulation

In previous publications[72,75] we have shown that the optimum set-up for an H&N hyperthermia applicator is a circular array (diameter=40 cm) of two rings of six antennas (spacing between rings=6 cm). We constructed such a set-up to measure the reflection characteristics of the patch antenna design within the applicator, and as such validate our theoretical analysis. Figure 5.3 shows the measurement set-up, which consisted of a PEC cylindrical backplane (diameter=40 cm, height=15 cm) that formed the groundplane of the patch design. To decrease the influence of a water-air transition, this cylinder was positioned on top of an absorbing flat muscle phantom, which was filled with demineralized water (25°C) to model the waterbolus. A cylinder (diameter=88 mm) filled with a 10g/l saline solution was used to model the patient. The theoretical patch design was adapted somewhat to increase its robustness under clinical conditions. In particular, we added a low-dielectric support which was only 10 mm in the x-direction and was positioned
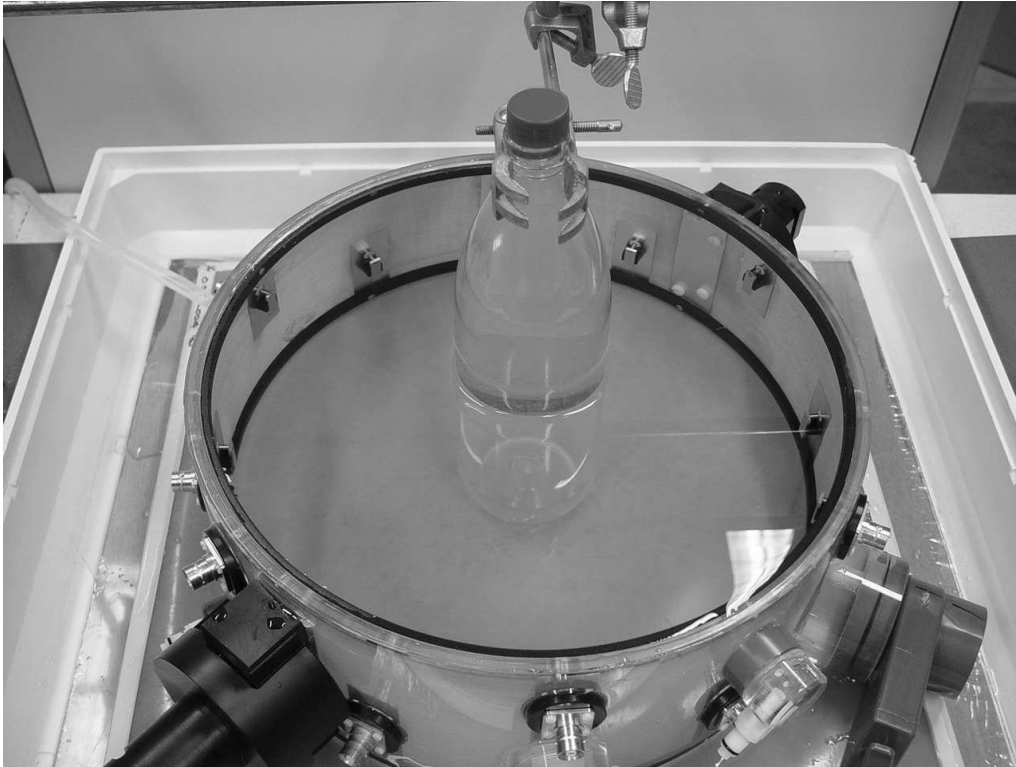
Figure 5.3: Picture of the measurement set-up with twelve antennas at staggered
locations in two rings[75]. Further visible are 1) the centrally placed
bottle containing saline water, 2) the gauze that forms the conduct-
ing backplane (limitedly visible) and separate conducting backplanes
per antenna and 3) the flat muscle phantom on which the antena ring
is positioned. The reflection characteristics of the lower six antennas
were measured for validation of the model.

centrally under the patch to avoid influences on radiation pattern and reflection
coefficient. By simulations we found that a support that is both centrally placed
and sufficiently small has a negligible influence on the resonance frequency. For the
measurements we used the six antennas of the lower ring (4.5 cm above the flat
muscle phantom), since these are affected the least by the water-air transition that
1) in practice is further away due to bulging of the waterbolus and 2) decreases
the reproducibility and predictability of the set-up. Reflection measurements were
performed using a 8751A network analyzer (Agilent Technologies, USA). As a result
of these measurements, the lengths of the patches were adapted one final time.

Figure 5.4 shows the corresponding solid model implementation for one antenna
of the measurement set-up in SEMCAD X. By using the model settings described
earlier, a model that consisted of 6 million cells was obtained, and total simulation
time was 25 hours using a special hardware accelerator (aXware[84]). Due to memory
limitations, we modelled only one antenna.
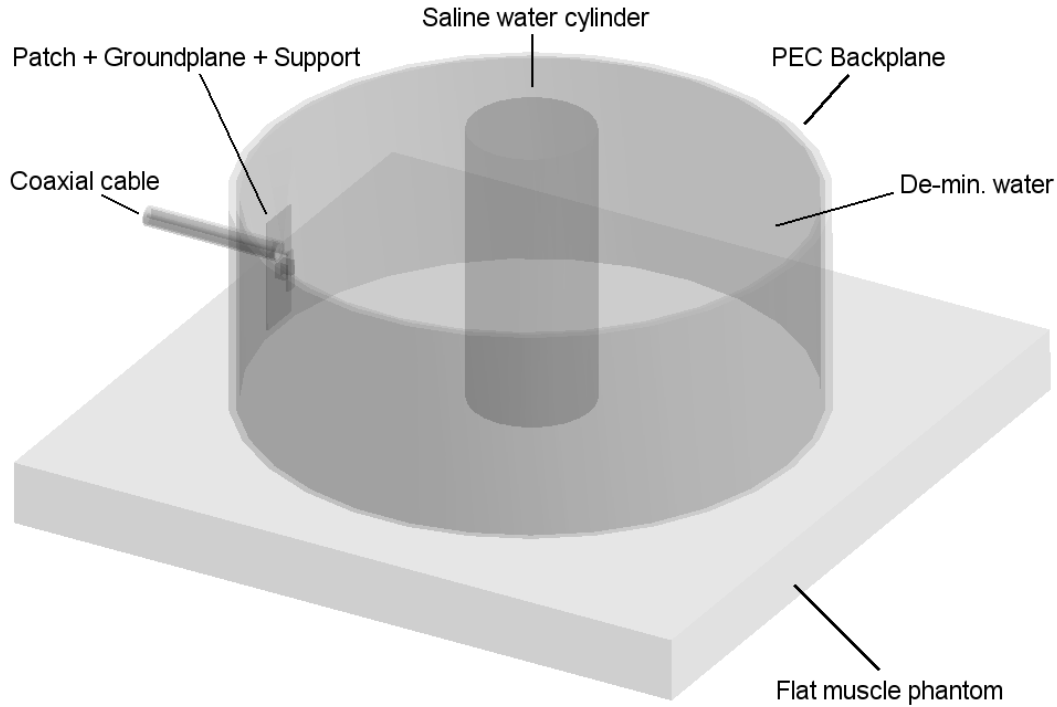
Figure 5.4: Solid model in SEMCAD X of the measurement set-up.

5.3 Results

5.3.1 Antenna design

Using Designer we found that a resonant antenna was obtained only at heights (h: substrate thickness) over 5 mm and lengths much smaller than $\lambda_{water}/2$. Using Designer's gradient optimizer, we optimized the patch dimensions for substrate thicknesses between 5 and 10 mm. The optimization procedure provided best results for set-ups with patch heights between approximately 8 and 9 mm. However, all minimum reflection values were well beneath -20dB, and the -15dB bandwidth was $\sim$ 28 MHz (6.5%), and thus sufficient for our purposes. The influence of the presence of a muscle layer (Figure 5.2: "Layer3") at a minimum distance of 4 cm from the antenna's groundplane was found to be negligible, i.e. it resulted in the same optimal dimensions as in the optimization without the muscle layer. We chose to continue our investigations using a set-up of: L=27.8 mm, W=10 mm, h=9 mm, x_f=1.75 mm.
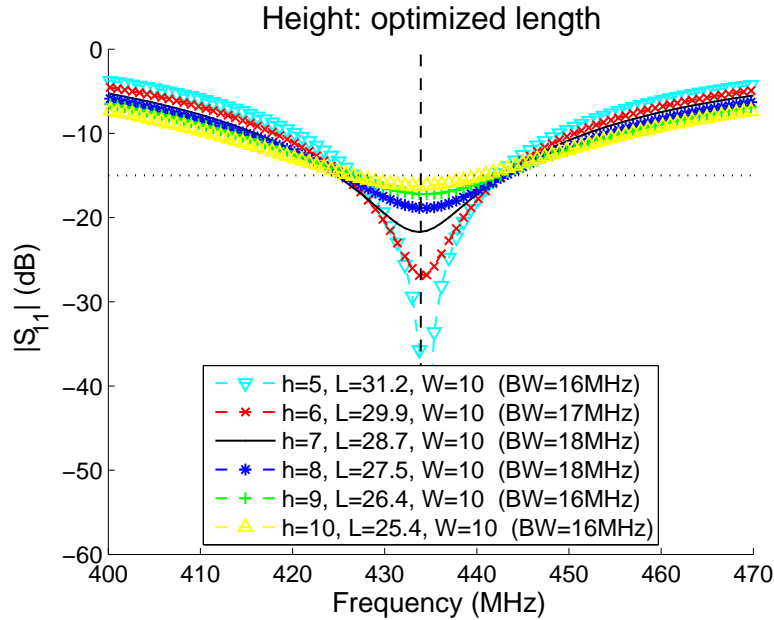
Figure 5.5: Reflection characteristics calculated with SEMCAD X for various
patch heights and optimized lengths.

SEMCAD X

When implementing the Ansoft Designer (2D-model) optimized set-up (h=9 mm)
in SEMCAD X v10.0 (3D-model), we found that Designer overestimated the per-
formance in terms of reflection characteristics. Using SEMCAD X, we fine-tuned
the set-up for better reflection characteristics. Hereto we investigated set-ups with
heights around h=9 mm, and scaled the lengths L of these set-ups to find a resonant
antenna at 433 MHz (W=10 mm, x_f=1.75 mm). The results of this optimization
are shown in Figure 5.5. Here, we selected the set-up with h=7 mm as optimum,
since this yielded the highest bandwidth (18 MHz=4.2%).
Subsequently, we analyzed the sensitivity of the design to its design parameters.
This is useful in assessing the influence of construction errors and for selecting the
best dimension for fine-tuning the clinical antenna. Figure 5.6 shows the sensitiv-
ity of the selection to all four design parameters. This figure shows that variations
in height and length are of great importance: the resonance frequency changes in
a rather linear fashion by approximately 12 MHz/mm (length) and 15 MHz/mm
(height). Small realistic errors in the location of the feed had little influence. Chang-
ing the width only scaled the real part of the antenna's impedance, i.e. the resonance
frequency remained unchanged. Therefore, we could further improve the design by
using the width that corresponded with a real part of the impedance closest to 50Ω
at 433 MHz. The final theoretical design was thus set at L=28.7 mm, W=8 mm,
h=7 mm, x_f=1.75 mm.
The electric field for this optimized set-up without ("all water") or with ("muscle
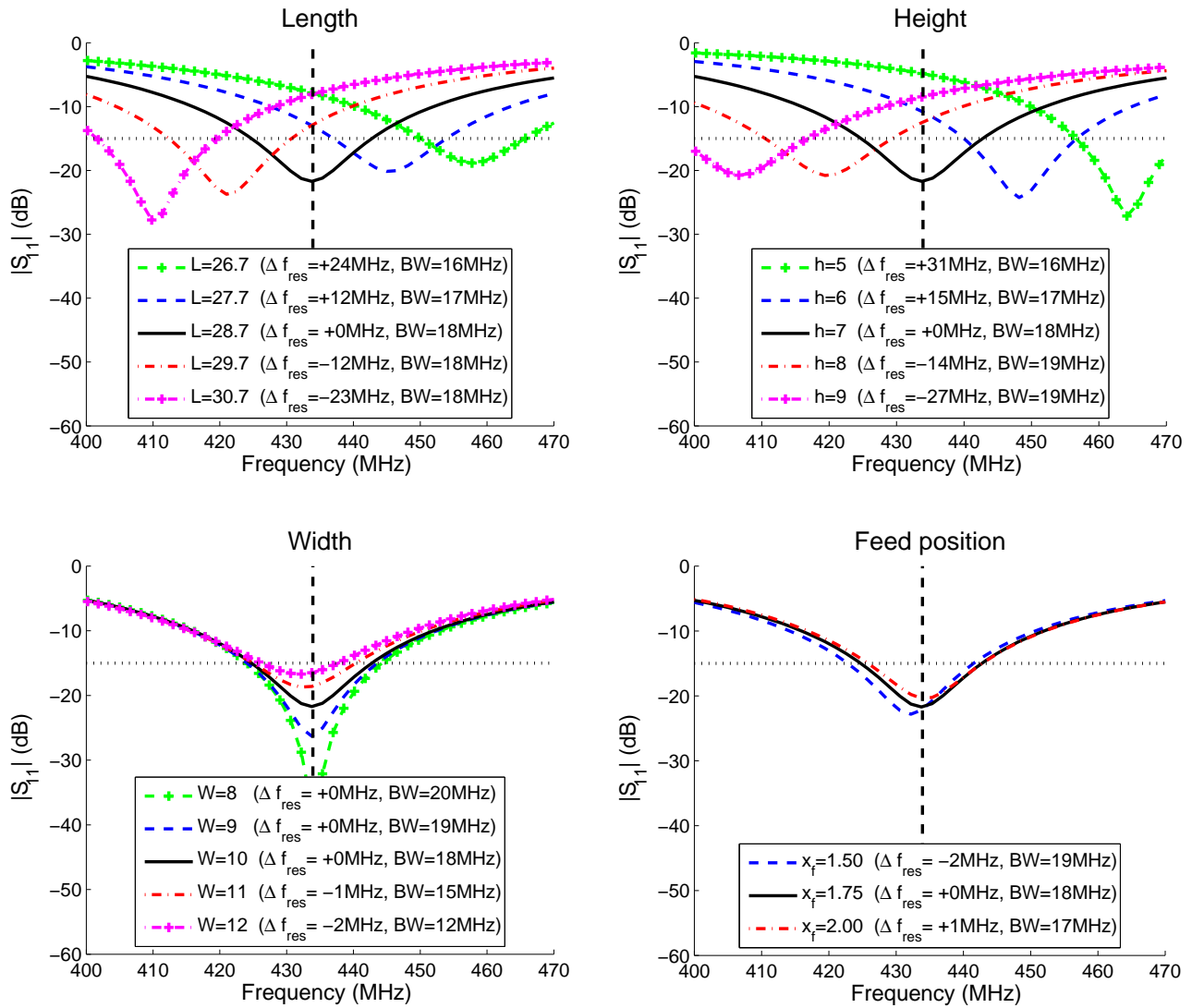
Figure 5.6: Sensitivity of the antenna design (L=28.7 mm, W=10.0 mm, h=7.0 mm and x_f=1.75 mm) to antenna dimensions, i.e. length, height, width and feed position (x_f), calculated by SEMCAD X.
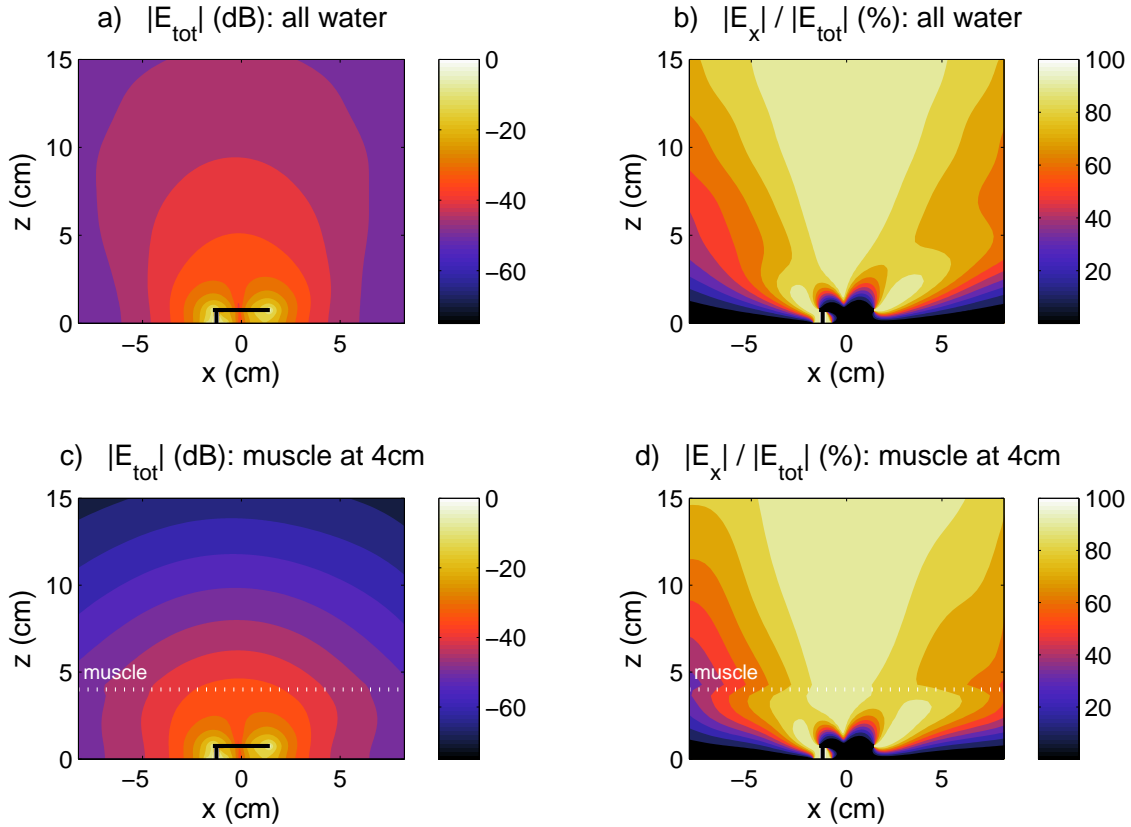
Figure 5.7: Rms value of the electric field (a, c) and respective amount of co-polarization (b, d) corresponding to a patch in water without (a, b) or with (c, d) a muscle layer. Cross-sections through $y=0$ are shown and the water-muscle transition is indicated by a white dotted line.

at 4 cm") a patient is shown in Figure 5.7. In this figure we visualize the rms value of the electric field and the amount of co-polarization, both with and without a patient. The figures show that the electric field decay is faster in muscle (a, c). The amount of co-polarization, however, is high (-5 cm $< x <$ 5 cm : >80%) for both the set-ups investigated (b, d).

5.3.2 Characteristics of the design under clinical conditions

To assess the performance of the design under clinical conditions, we theoretically analyzed its reflection characteristics for 1) waterbolus temperature changes, 2) the presence of a patient, and 3) the presence of a neighbour antenna. Figure 5.8 shows the reflection curves corresponding to water temperatures between 15°C and 35°C. For increasing temperatures, these curves show that the shape of the reflection curve remains intact, but that the increase in resonance frequency was linear at
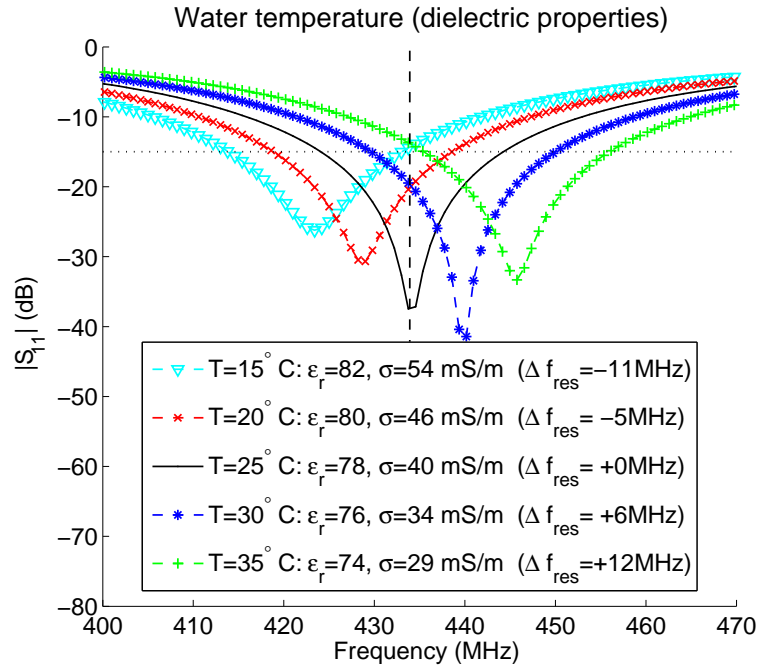
Figure 5.8: Sensitivity of the reflection coefficient to changes in waterbolus temperature.
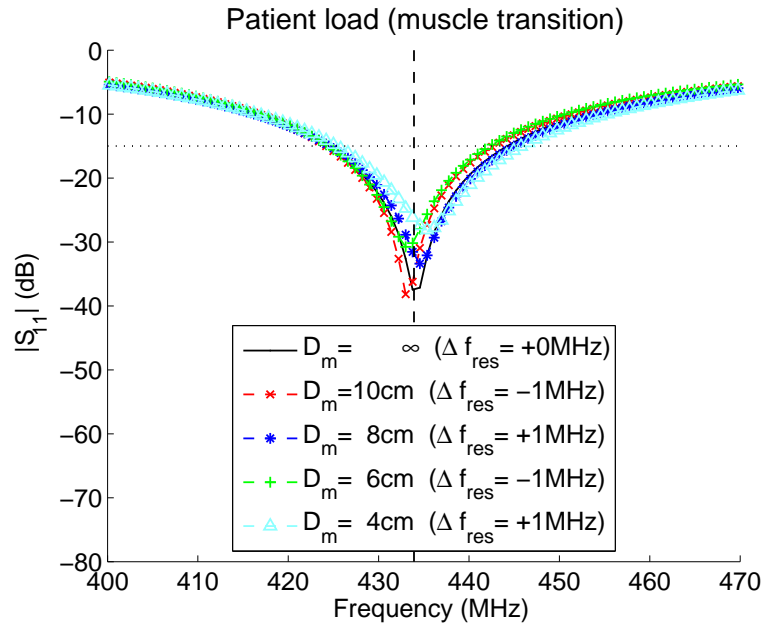
Figure 5.9: Sensitivity of the reflection coefficient to an approaching muscle layer. D_m is the distance between groundplane and muscle transition.

around 1 MHz/°C. Figure 5.9 shows the reflection curves corresponding to decreasing patient-antenna distances, i.e. decreasing muscle-layer heights. Different patient-antenna distances ($D_m > 4$ cm) showed little influence, i.e. an almost stable (<1 MHz) reflection pattern. An extreme (50%) decrease and increase of the dielectric properties of the muscle layer ($D_m = 5$ cm) resulted only in a very small additional alteration of maximum 1 MHz in resonance frequency. The combined influence of a patient and a neighbour antenna was investigated for three set-ups: 1) without a muscle-layer, 2) with a muscle-layer at 10 cm, and 3) with a muscle-layer at 5 cm. The predictions show 1 MHz maximum, uncorrelated, differences in resonance frequency with respect to the reference situation: a set-up with no muscle layer and no neighbour antenna. All orientations (vertical, horizontal and diagonal) and all muscle distances (∞, 10 cm and 5 cm) show little cross-coupling between neighbours: $S_{21} <$ -27dB.

5.3.3   Clinical antenna set-up: measurements and simulation
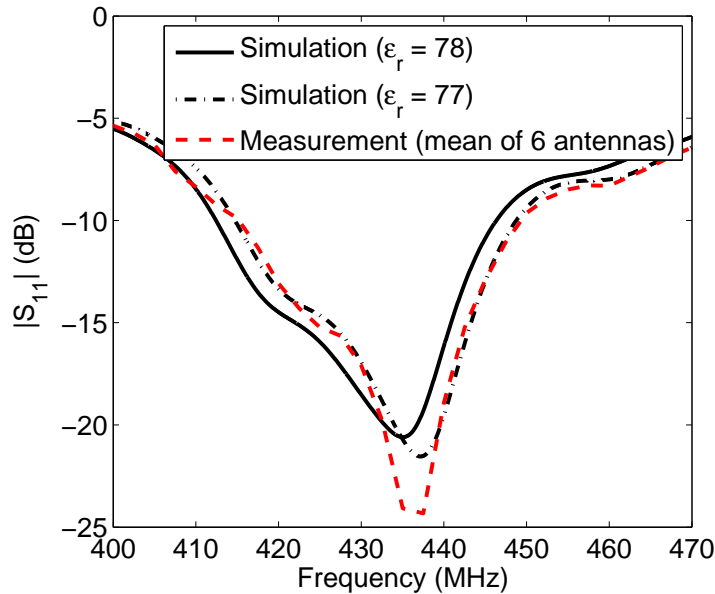
Figure 5.10: Mean of reflection measurements of 6 patches in the applicator ring and corresponding FDTD simulation results for two values for the permittivity of the water in the waterbolus.

Utilizing measurements of patch antennas in the applicator set-up (see Figure 5.4), we made a final amendment to the theoretical design, i.e. we reduced the length: L=28.2 mm, W=8 mm, h=7 mm, x_f=1.75 mm. Figure 5.10 shows the curves of the average measured reflection characteristics of six of such patch antennas, while the water temperature was 24.8°C. The figure indicates that, on average, the patches had

the following characteristics: S_{11}(433 MHz)=-21dB and BW=18.5 MHz (4.3%). This figure also shows a good agreement between simulated values and measurements. For these calculations we used as permittivity both ϵ_r=78 and ϵ_r=77, to illustrate the slight better agreement at this lower value. The figure also shows that the model can be used to predict the location of the resonance frequency with reasonable accuracy but the predicted bandwidth is somewhat lower (BW=17.1 MHz). Since the depth of the peak depends on the conductivity of the water, this might explain the discrepancy in depth of the resonance peak remaining ($\sim$4dB). We expect that, in the more predictable flat set-up that we used for the analysis, differences will be even less than in this applicator set-up with its more cavity-like behaviour.

5.4 Discussion and conclusions

In this study we have designed a patch antenna and when we examine its characteristics against the design criteria formulated at the start, we can draw the following conclusions: 1) the patch antenna design has a high amount ($>$80%) of co-polarization in broadside direction, 2) while the dependence of the resonance frequency is linearly dependent on the temperature, it can be chosen to allow water-bolus temperatures between 15 and 35°C, 3) the influence of a patient at a distance as close as 4 cm from the groundplane is a maximum resonance frequency shift of 1 MHz, 4) cross-coupling with neighbour-antennas in all investigated realistic set-ups was predicted to be lower than -27dB. Although these low cross-coupling values indicate that it will be of no concern in the clinical applicator, this aspect will be investigated further; we are specifically interested in the combined cross-coupling when all twelve antennas are operating coherently.

A clinical version of the patch antenna was constructed, and modifications were made for better mechanical robustness and to conform it within an array of antennas. The simulations of the theoretical set-up were validated by performing measurements with six of these patch antennas. These measurements show a very good agreement for the resonance frequencies obtained, and a good agreement for the obtained bandwidths. We found that the length of the patch antenna for resonance in an infinite water halfspace (L_{res}=28.7 mm) could be slightly reduced for resonant behaviour within the applicator (L_{res}=28.2 mm). The situation in the applicator differs from the theoretical situation because 1) the groundplane was curved, 2) a low-permittivity support was added for stability, and 3) the patch was placed in the waterbolus, which acts to some extent as a cylindrical resonant cavity. Although the contribution of each effect to this decrease in required length is unclear to us, the adapted patch length was accurately predicted by SEMCAD X. We further found that the bandwidth obtained with the infinite layered set-up (20 MHz, 4.6%) is somewhat larger than that in the applicator set-up, i.e. simulation: 17.1 MHz (3.9%) and measurement: 18.5 MHz (4.3%). This -15dB bandwidth is similar compared to a probe-fed patch design radiating into air as reported by Garg *et al.*[27].

For simulations throughout this paper, we used properties of muscle and water at 433 MHz for all frequencies. Theoretically, in our entire frequency range (400-470 MHz), the variation in permittivity values is small: -0.01% for demineralized water[88] and -0.9% for muscle[26]. The variation in conductivity, however, is much greater: +28% for demineralized water[88] and +2.3% for muscle[26]. On the basis of our own measurements with saline water (unpublished data), we know that the conductivity of the water has an effect on the depth of the S_{11} curve of a patch antenna, i.e. increasing conductivity leads to a flatter curve, but not on the resonance frequency. By comparing the measurements with the simulations (Figure 5.10), we also show that the main difference is indeed the depth of the resonance peak, but that the estimation of the resonance frequency is fairly accurate ($\Delta f_{res} \sim 2$ MHz). We have investigated the application of a probe-fed patch antenna design in a phased-array H&N hyperthermia applicator. If we convert the results of our analysis to the situation for DHT, this design has several advantages over the designs currently used. The main advantage of this design is the direct feeding with a coaxial cable, i.e. no matching circuit is required. As we explained before, this leads to easier and more accurate modelling, and also to greater robustness and higher efficiency. A main drawback of the design for a more broadband application (multiple frequencies) is its relatively small bandwidth. However, in this application this is not a problem, as we use only a single frequency.

Acknowledgements

CHAPTER 6

Experimental SAR verification with a laboratory prototype

Abstract

Purpose *Experimental verification of the feasibility of focussed heating in the neck region by an array of two rings of six electromagnetic antennas. We further measured the dynamic specific absorption rate (SAR) steering possibilities of this set-up and compared these SAR patterns to simulations.* **Materials and methods:** *By a specially constructed laboratory prototype head and neck applicator, including a neck mimicking cylindrical muscle phantom, we performed SAR measurements by electric-field Schottky-diode sheet measurements and, using the power-pulse technique, by fiberoptic thermometry and infra-red (IR) thermography. Using phase-steering, we also steered the SAR distribution in radial and axial directions. All measured distributions where compared to predictions by a finite-difference time-domain (FDTD)-based electromagnetic simulator.* **Results:** *A central 50% iso-SAR focus of 35 mm (±3 mm) in diameter and around 100 mm (±15 mm) in length are obtained for all investigated settings. Further, this SAR focus can be steered towards the desired location in radial and axial direction with an accuracy of ∼5 mm. SAR distributions as measured by all three experimental methods are well predicted by the simulations.* **Conclusions:** *We conclude that focussed heating in the neck is feasible and that this focus can effectively be steered in both radial and axial direction. For quality assurance (QA) measurements we conclude that the Schottky-diode sheet provides the best compromise between effort, speed and accuracy, although a more specific and improved design is warranted.*

6.1 Introduction

Loco-regional control of advanced carcinomas in the head and neck (H&N) region still poses a major therapeutic challenge[20,79] and treatment related toxicity remains a major issue in this region[90]. Combining hyperthermia (HT) with the current treatment modalities has a high potential to increase treatment outcome without increasing toxicity[39]. Recent phase III trials have shown the benefit of the addition of HT to current treatment modalities for various tumour sites[10,44,99]. Valdagni *et al.*[94,95] have demonstrated that with a non-site-specific HT-applicator already a significant increase in local control (from 24% for radiotherapy (RT) alone versus 69% for RT plus HT) is achieved for metastatic lymph nodes in stage IV carcinoma of the H&N. Extension of the hyperthermia application to deeper located tumours is cumbersome with the available applicators and therefore requires a specific designed applicator that is also expected to contribute to a better treatment quality for this site[87,107]. In recent years, we have investigated the ability of a multi-element circumferential H&N HT applicator to deposit radiofrequency (RF) energy selectively in the center of the neck[72]. Suitable frequencies were shown to be in the frequency band between

300 and 600 MHz for all realistic target sizes therefore we selected 433 MHz* as operating frequency. Further, we found that eight antenna elements provide sufficient focussing for selective heating. Building on these findings, we analyzed the influences of the anatomy on the SAR pattern[73]. In this study we found that the SAR patterns in a homogeneous muscle cylinder are predictive for the SAR pattern in inhomogeneous neck structures. Therefore muscle phantom measurements will be predictive for the SAR pattern that can be obtained in the middle of the neck. Due to the spine, the central SAR focus changes from a circular to a more donut shape but the central focus remains at its central position. Subsequently, research was conducted into possibilities of further improving the power absorption pattern by going from one to two or three antenna rings[75], which provides also axial steering possibilities. We established that heating at depth is highly correlated with the number of antennas arranged in multiple rings. Multiple rings enable steering in the direction of the patient axis, which is well validated for deep hyperthermia[77,83] but needs confirmation for the head and neck application. This work resulted in a final set-up design: a set-up with two rings of six antennas each operating at 433 MHz. As radiators, we selected a patch antenna set-up that is simple, low-cost, efficient and small and we designed it specific for the head and neck applicator[76]. Another major advantage of this antenna design is that no matching network is required, which facilitates a better control of the input parameters of the set-up and hence provides better possibilities to create a representative model. Subsequently, the latter improves the reliability and accuracy of numerical predictions.

The aim of the present study was to experimentally verify the feasibility of focussed heating in the head and neck region using an array of two rings of six antennas by the split-phantom technique. Simultaneously, we established the accuracy of the predictions of our electromagnetic simulation model. Finally, we explored the dynamic SAR steering behavior of the antenna array. Hereto we constructed a laboratory prototype applicator consisting of twelve patch antenna elements and a muscle-equivalent neck phantom. We performed measurements with this set-up and compared them to predicted SAR patterns.

6.2   Materials and methods

6.2.1   Prototype design

Figure 6.1 shows a picture of the bottom half of the prototype applicator and Figure 6.2 visualizes an exploded view of its two parts. These parts can be separated to allow 2D IR measurements or positioning of measurement devices: glass fiber probes or electric (E)-field Schottky-diode sheet. Both parts of the applicator consist of a semi-circular PVC backplane (diameter = 30 cm, length = 60 cm: Figure 6.3) and PVC shields at both ends. Both half backplanes are covered, waterproof, with a

---

*433 MHz is an ISM frequency: a frequency available for Industry Science and Medicine

50μm thick ABS copolymer sheet that is glued on a frame that can be mounted on the backplanes (see Figure 6.2). Twelve antenna elements are mounted on the PVC backplanes in a 2x6 arrangement[75], i.e. two rings (distance = 8 cm, ring-radius = 30 cm: see Figure 6.3) of six equally spaced patch antennas. We defined the origin of the applicator between the rings so the antennas in these rings are located at z = -4 cm and z = 4 cm. The water in the prototype was circulated and temperature controlled by two E4850 refrigerated recirculators (Bio-Rad, Microscience Division).

Every patch antenna[76] consists of a, resonant, 2mm-thick brass patch (width = 12 mm, length = 25 mm) that is asymmetrically (the distance from the rod to the side of the patch is 0.5 mm) mounted on the extending conducting rod of a C-female receptacle connector. Coaxial cables are used to transfer the 433.92 MHz signal from PG70.150.2 power generators (SSB Electronic, Germany) to the applicator. The conducting backplane required for the patch antenna design is formed by soft copper tape (thickness: 35 μm + 25 μm adhesive) that covers the inner side of both PVC backplanes (see Figure 6.1).

Two PVC semi-cylinders (muscle cylinder diameter = 11.6 cm, PVC thickness = 1.5 mm) [†] filled with muscle equivalent material, representing the neck of a patient, are positioned at the center of the prototype. The muscle-equivalent material was created using a recipe described by Ito *et al.*[40] and had properties in accordance with Gabriel *et al.*[26] (see Table 6.1).
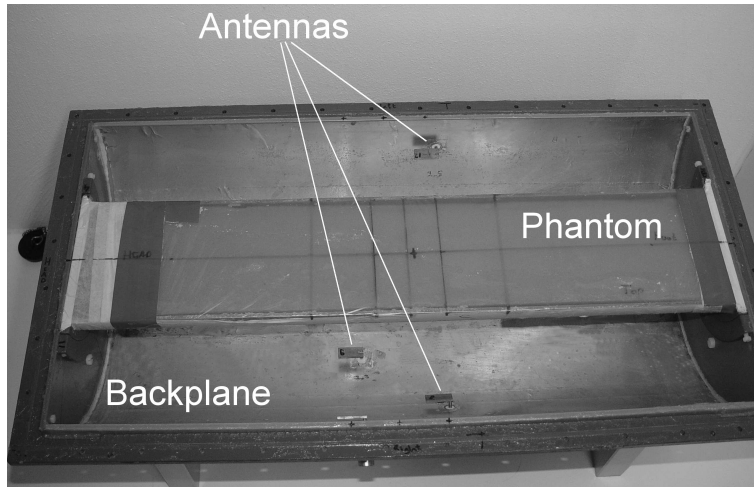
Figure 6.1: Picture of the bottom half of the prototype with the sheet and its frame excluded. Visible are the copper tape that covers the backplane, one half of the muscle phantom and multiple patch antennas

---

[†]The dimensions of the phantom approximately equal an average neck[73]
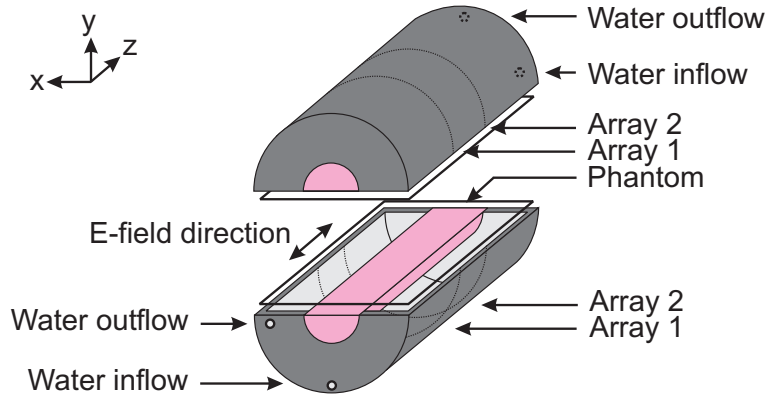
Figure 6.2: Exploded view of the prototype that is constructed in two parts for measurements (T-probes, E-field sheet, IR pictures). Visible are the phantom semi-cylinders (pink/light grey), the two frames spanning the sheet, the PVC backplanes (dark grey) and the copper tape on the inside of the backplanes (light grey).

6.2.2 EM modelling

We predicted the SAR distributions in the prototype applicator using SEMCAD[84]. SEMCAD has a FDTD kernel that can be used for dosimetric simulations. It includes a solid modeling kernel in which we created a full 3-D model using the exact dimensions of the applicator prototype and muscle phantom. The sheets between the semi-cylinders could be neglected for calculations since they were very thin. Further, instead of modeling the complete connector and the transmission line, we used the commonly accepted approach to apply a voltage source at the gap between the conducting backplane and the rod of the patch antenna[81], which provides accurate field distributions[15]. This solid model was converted automatically into a grid implementation with maximum gridsteps of $\lambda/15$ and grid refinements at the locations of the antennas ($\lambda/250 < \Delta < \lambda/80$), i.e. a total of $\sim$5 million cells. The grid refinements at the antennas were required to accurately model the (important) small dimensions of the antenna and the non-orthogonal placement in the grid, at the location of the feeding rod. Table 6.1 lists the properties of all the materials used in the simulation. Properties of demineralized water (salinity = 0.04 g/l, T = 25°C) were found in a publication of Stogryn[88]. We exited the voltage sources at all gaps at 433 MHz and steady state was obtained after 10 periods (1% variation).

6.2.3 Measurements

Three SAR pattern measurement methods were used because they all have their own features: their major strengths are either accuracy (fiberoptic thermometry),
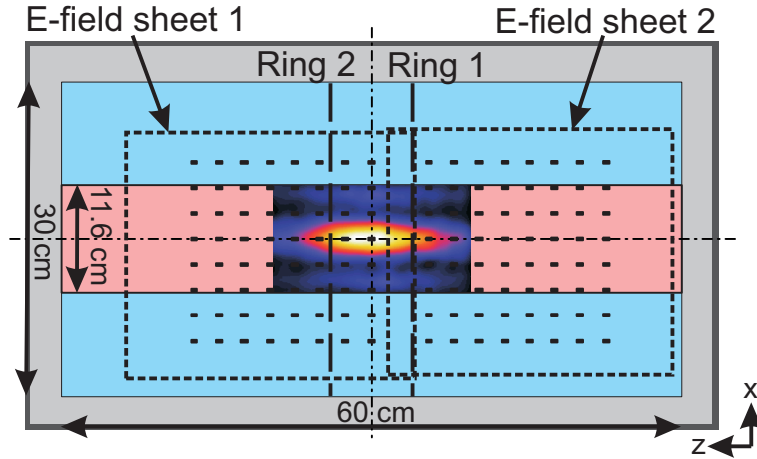
(a)
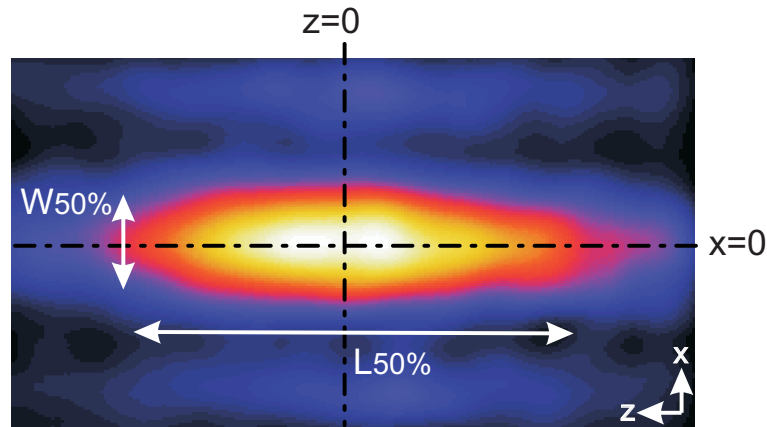
(b)

Figure 6.3: Cross-section through the prototype at $y = 0$ cm with a SAR distri-
bution obtained from two IR pictures (before and after heating) for
central settings (a) and a zoomed version of this SAR distribution
(b). In (a), the location of the Schottky diodes (E-field sheet 1 and
2) is indicated by the black rectangles and the boundaries of the
sheets by the dotted lines. Further, the location of the antenna rings
and the main dimensions of prototype and phantom are indicated.
T-probe measurements are taken at locations on the lines indicated
by "x=0" and "z=0". In (b) the colorscale is from black (0%) to
white (100%) and the length ($L_{50\%}$) and width ($W_{50\%}$) of the focus,
i.e. the 50% iso-SAR contour, are indicated.

Table 6.1: Properties of the materials at 433 MHz

Material	ρ (kg/m^3)	ϵ_r (-)	σ_{eff} (S/m)
Muscle phantom	900	56	0.8
PVC	1350	2.2	0.004
Demineralized water	1000	78	0.04

resolution (IR thermography) or speed (E-field Schottky diode sheet). These measurement methods and their results were compared to establish the optimum method for quality assurance. Waterbolus temperatures where chosen such that mean temperatures in the prototype were around 22°C, at which the phantom properties are reported, i.e. the waterbolus temperatures was 18-19°C for the power-pulse measurements (T-probes and IR) and 22°C for the E-field measurements. Figure 6.3 shows a cross-section through the applicator at $y = 0$ cm and a zoomed version of the SAR distribution obtained by taking IR pictures before and after heating.

Fiberoptic thermometry

Temperatures were measured with 24 Takaoka FTP1 standard sensor probes (accuracy = 0.1°C, precision = 0.1°C), which are read with a Takaoka FT1310 fiber thermometer (Takaoka Electric MFG Co. Ltd., Japan) with a refresh rate of 3s. These non-metallic probes were positioned at the main axes between both halves of the prototype. The local SAR was measured using the power pulse method: the change of temperature (3-10°C) in a phantom is measured while applying a high power (300-600W) for a short time (90-300s) at the antennas of the applicator[82] (see Figure 6.5). To reduce influences of heat conductivity a short heating time is required, therefore we used a high power to obtain accurately measurable temperature changes. The local SAR is calculated from the temperature rise via:

$$\text{SAR}(x, y = 0, z) = c \cdot \frac{\Delta T(x, y = 0, z)}{\Delta t}, \tag{6.1}$$

where c is the specific heat capacity of the muscle phantom material (3.63 kJ kg^{-1} K^{-1}), ΔT is the local temperature rise [K] and Δt is the corresponding heating time [s]. We assumed no electric field disturbing effect of the fiber probes.

IR thermography

We used IR thermography to visualize the temperature (rise) pattern at a high resolution (320x236 pixels). Pixel size was determined by taking an IR picture of a hot object with known dimensions: for our set-up the dimensions were 0.5x0.5 mm^2. After application of power, the top half was removed and IR pictures were taken using a TVS-600 infrared camera (Nippon Avionics Co. Ltd., Japan) that was

mounted on a solid framework. From the IR picture before and after heating we calculated the SAR pattern using equation 6.1. The inevitable time between end of heating and first IR picture was kept as short as possible (typically $\sim 10s$) in an attempt to reduce influences of heat conduction.

E-field Schottky-diode sheet

For fast measurements, which also enables studying the prototypes dynamic behavior, we performed SAR measurements also with the E-field Schottky diode sheet, that is described in Kaatee *et al.*[46] and Van Rhoon *et al.*[104]. Hereto, two diode sheets were positioned between both halves of the prototype (Figure 6.3). To avoid a decrease in sensitivity caused by overlapping sheets at the location of the diodes[105], we used a distance between both sheets such that one row of measurement points was absent. SAR values can be calculated from the amplitude of the measured E-field values, using the effective conductivity (σ_{eff}) and mass-density (ρ), according to:

$$SAR(x, y = 0, z) = \sigma_{eff} \cdot \frac{|E(x, y = 0, z)|^2}{2\rho}.$$ (6.2)

The E-field sheet directly measures real-time the axial (z) component of the E-field. Also, variations in dielectric properties of the phantom materials are much lower because measurements can be performed at low power (120W). Further, no manipulation of the set-up is required for multiple measurements, i.e. all distributions can be measured using one single disposition of the experimental set-up. Without calibration the accuracy of the sheets is 6%[104], however when airgaps are present close to the diodes this accuracy is reduced due to lower sensitivity. A main disadvantage of the current design of the sheet is its poor spatial resolution for measurements at 433 MHz, i.e. the distance between two diodes is 2.5 cm ($\sim \lambda/4$).

Measurement procedures and phase settings

As a first step we measured impedance characteristics of the antennas using an 8751A network analyzer (Agilent Technologies, USA) to verify that they were sufficiently resonant. As a side step we also assessed the amount of cross-coupling using the network analyzer. Fiberoptic and IR measurements were conducted simultaneously. Hereto we positioned an IR camera above the prototype and positioned the probes between both halves of the prototype. High power was applied and simultaneously we measured temperatures with the fiber probes (see Figure 6.5). After the required maximum temperature change was obtained, we opened the applicator and took IR pictures. We used a cooling time of typically 2 hours between subsequent measurements to obtain a homogeneous thermal distribution. E-field sheet measurements were performed separately at low power to avoid variations in dielectric properties of the phantom due to temperature differences. To check for measurement errors,

all measurements were conducted multiple times in a time period of a year and the muscle phantom was newly constructed two times.

To obtain a central focus for each antenna (i) on each ring (j) we used central power (P) and phase (φ) settings ($P_{j,i} = 25$ W and $\varphi_{j,i} = 0$). Subsequently, we investigated the possibilities of SAR steering in radial and axial direction by using a phase-steering method in analogy to the method that is used in the BSD2000 Sigma-60 system[1,92]. For each antenna, we analytically calculated the required phase delays ($\varphi_{i,j}$), using the difference in wave velocity in muscle and water, such that maximum interference occurs at the desired Target Center Point (TCP). For this analytical model we assumed a muscle cylinder (radius is 5.8 cm) and two circumferential arrays (radius = 14.15 cm) of six point sources at z = -4 cm and z = +4 cm and we neglected the PVC phantom-shell.

6.3   Results

6.3.1   Reflection and cross-coupling

After one year, reflection coefficients had increased due to degradation (oxidation) of the set-up (mainly the copper tape of the groundplane). Figure 6.4 shows the typical reflection coefficients of all antennas in the array at 23°C and 25°C halfway during our measurement period. This figure clearly shows that the reflection coefficient is influenced by the temperature of the water in the waterbolus. For both temperatures these reflection coefficients are all beneath -10dB ($\sim$6% reflection on average) so efficiency of the antennas was sufficient for the purposes of our measurements. For the clinical applicator, however, we constructed a redesign that has somewhat improved reflection characteristics[76]. For this qualitative analysis we neglected the influences of the variations in efficiency ($\sim$6%) for the antennas of the prototype. We further found low cross-coupling between the antennas: maximum -22dB (0.6%) and on average -27dB (0.2%). The lowest values where obtained for neighboring antennas while the highest values where found for antenna pairs with around one quadrant inner antenna spacing. This effect is related to the radiation pattern of the antennas combined with the distance through a lossy medium.

6.3.2   SAR tracks

Figure 6.5 visualizes an example of the measured temperatures with the fiber probes and the corresponding measured powers and phases. It shows the length of the power pulse and the corresponding temperature rise from which we calculated the local SAR values. In this example case, the upper halve of the prototype was removed approximately 160s after Power On and 10s later the IR picture was taken. The corrections by the control loop that are required to keep the power at the set value (25W) are clearly visible in the power curves. At the start of the power
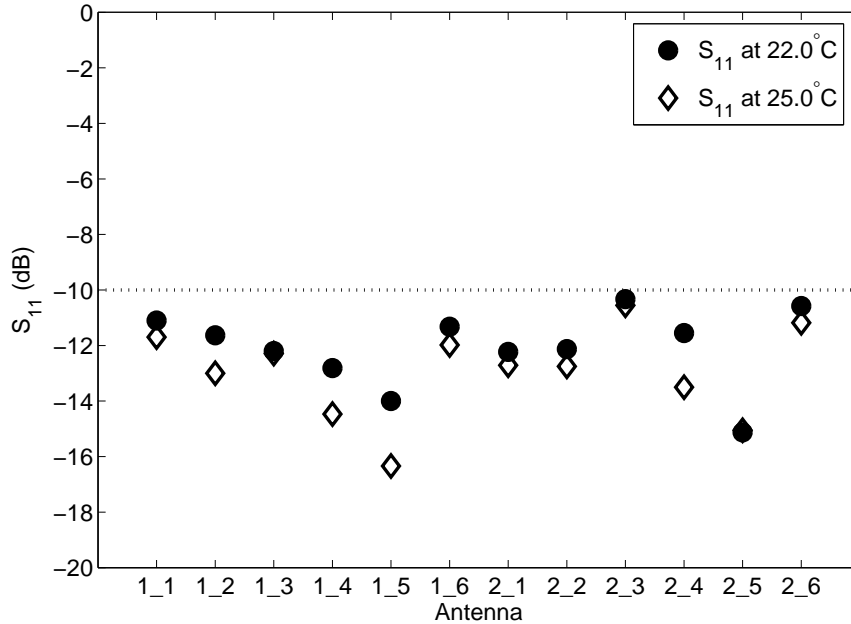
Figure 6.4: Reflection coefficients at 433.92 MHz for each antenna of both arrays, e.g. 1_2 is the second antenna of the first antenna ring.

pulse, the phases were influenced somewhat by the increase in power level, but these were automatically adjusted. The figure also shows that two amplifiers were leaking some power after power-off but this influence was relatively small (power-on: 300 W vs power-off: ~5 W leakage). We found an almost perfect correlation between the measured temperatures and a linear fit, for all spatial locations ($r^2 = 1.0$), so we concluded that the influence of heat conduction on the SAR measurements was negligible.

Comparing measurements and simulation

Figure 6.6 shows SAR values as function of the x-coordinate for TCP-based x-steering, i.e. for $x = $ -30 mm, $x = 0$ mm and $x = +30$ mm. Similarly, Figure 6.7 shows SAR values as function of the z-coordinate for TCP-based z-steering, i.e. for $z = $ -50 mm, $z = $ -25 mm and $z = 0$ mm. For all IR thermography tracks we averaged over 10 pixels (one pixel was 0.7x0.7 mm^2) to reduce noise. The tracks were normalized to their own maximum (IR thermography) or their own maximum of a spline-fit through the measurement points (T-probes and E-field sheet measurements). For central steering this maximum was typically around 0.6 W/kg (normalized to 1 W total input power). The desired focus point (TCP) is always indicated with the dashed line.

All measurements and predictions show that a central focus is obtained. As shown
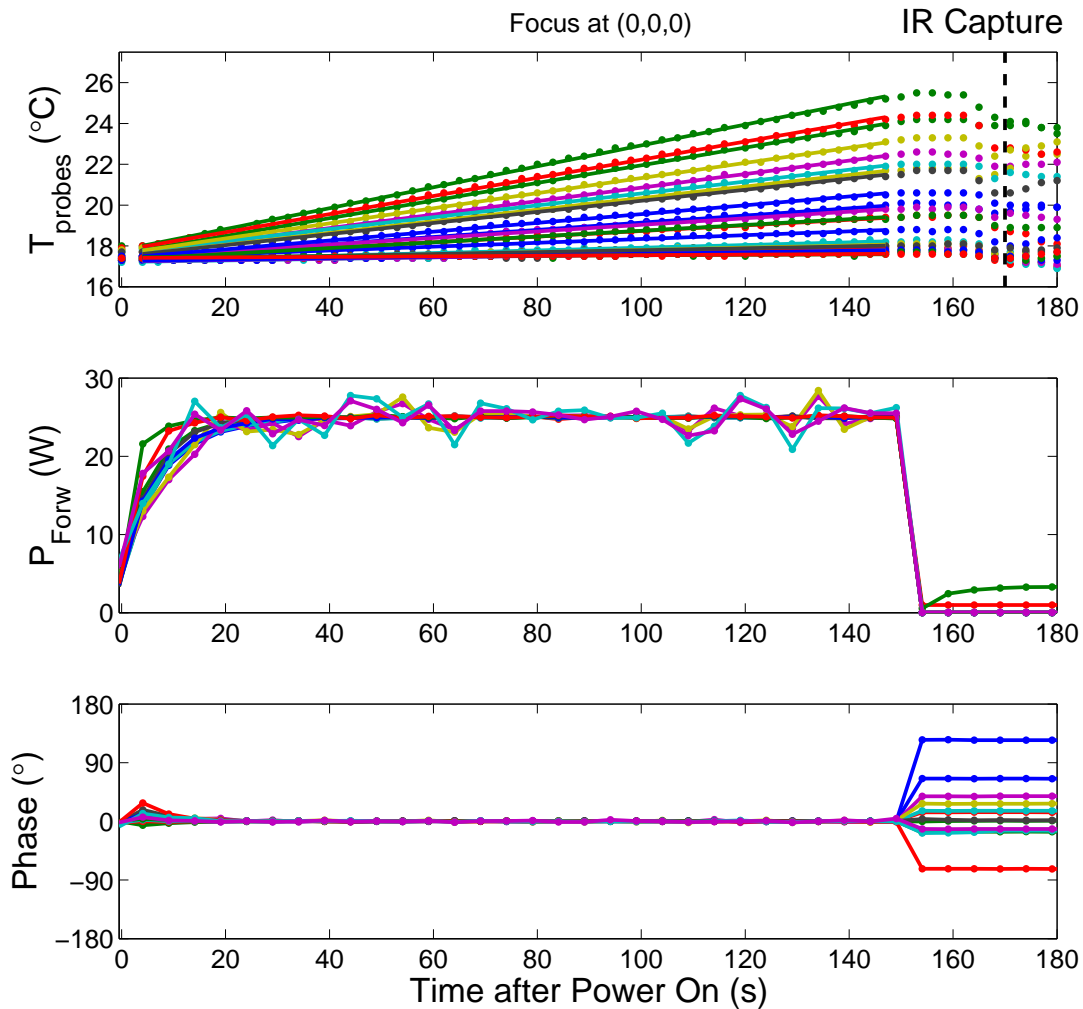
Figure 6.5: Temperature (T_{probes}) values and corresponding powers (P_{Forw}) and phases as function of time during an example powerpulse measurement. For the fiber probe temperature measurements (visualized in dots) we created linear fits (solid lines) and calculated the local SAR values from the slopes. IR pictures where captured before Power On and after Power Off (shown in the figure).

by these figures, this focus can be changed in the radial (x) and axial (z) directions. Comparing the results of the three measurement methods, we found a good qualitative agreement. Comparison of the simulations to these measurements reveals good agreement at central positions but discrepancies for more radial positions close to the PVC phantom border. The reason for this difference may lie in: 1) wrong dielectric properties of muscle phantom (lower conductivity) or 2) air-gaps at the
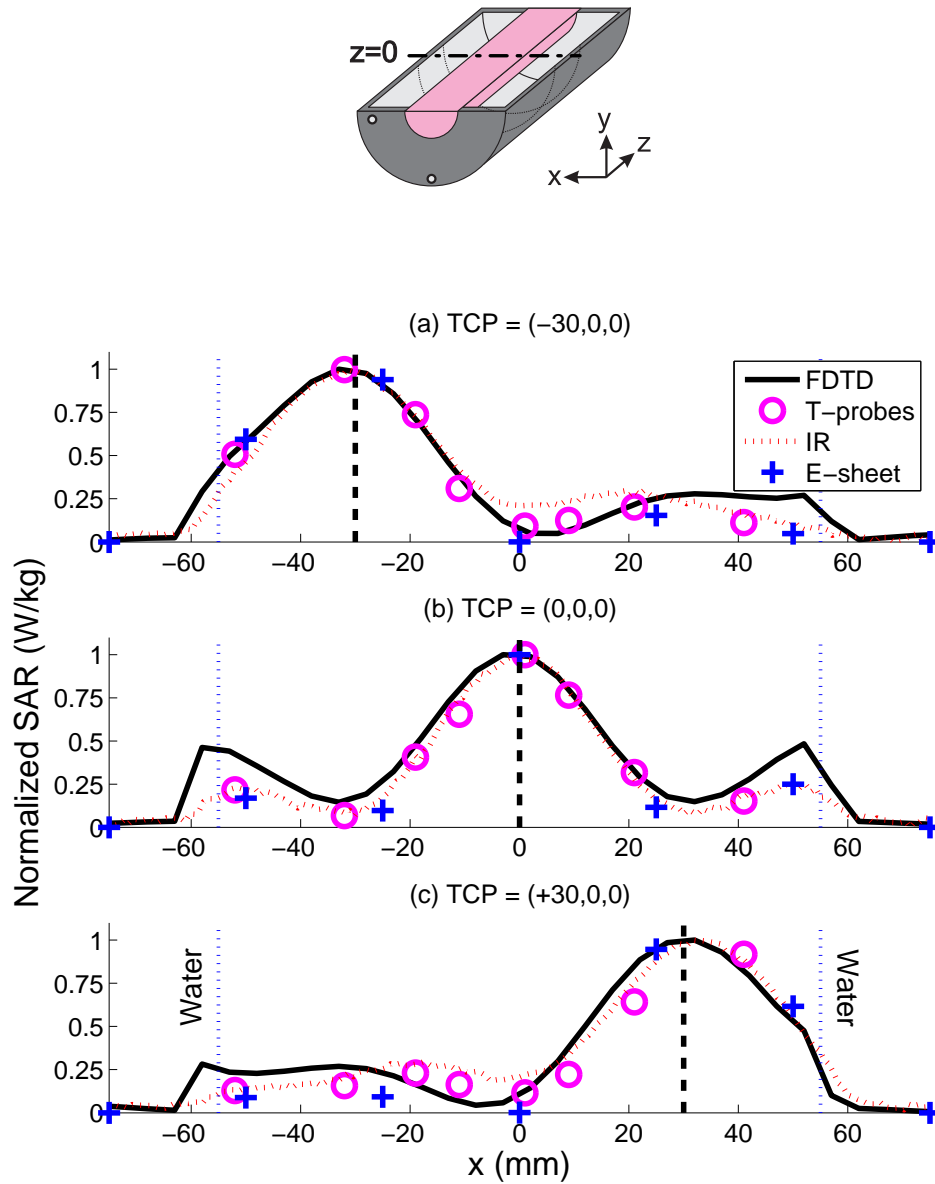
Figure 6.6: Simulated (FDTD) and measured (T-probes, IR and E-field sheet) SAR values at $y = 0$ mm and $z = 0$ mm for steering in the x-direction. The measurement values of all tracks are normalized to their own respective maximum value.
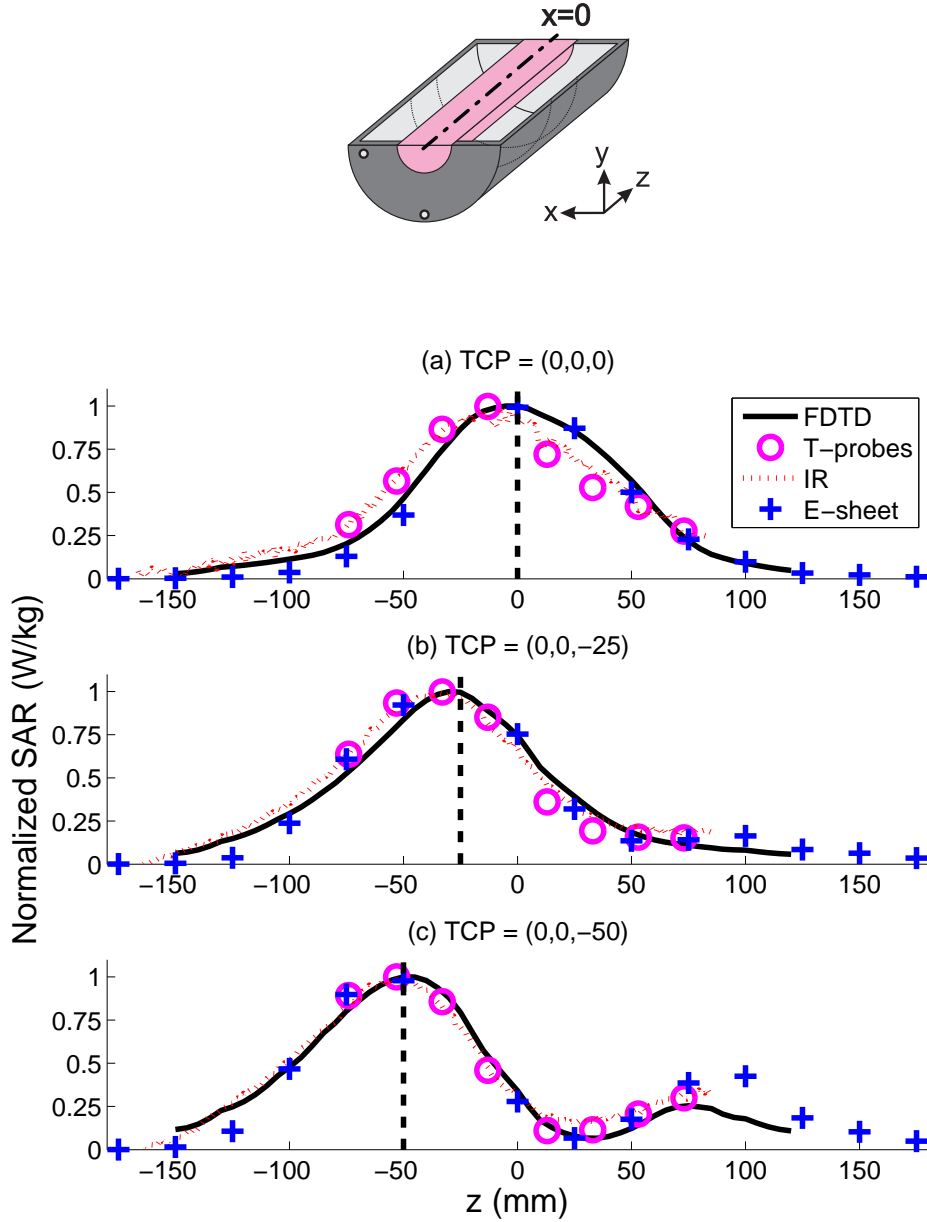
Figure 6.7: Simulated (FDTD) and measured (T-probes, IR and E-field sheet) SAR values at $x = 0$ mm and $y = 0$ mm for steering in the z-direction. The measurement values of all tracks are normalized to their own respective maximum value.

connection between both halves of the set-up. In the axial direction, there is an unexpected small asymmetry in the FDTD results for central settings (Figure 7a), this is probably caused by the asymmetry in the feeding of the antennas[76].

In radial direction, where the SAR patterns are the steepest, the IR thermography curves show a somewhat flattened profile compared to the FDTD tracks. This flattening is caused by thermal conduction during opening of the two halves after power application. After normalization this results in relatively higher values in the valleys of the curves because the maximum value is reduced. In axial direction this effect is less prominent because SAR curves are less steep. Further, the SAR values are decreased by the circulated water of the waterbolus of a stable temperature.

Determination of the focus-size

Table 6.2: SAR steering (TCP setting (mm) and location of SAR_{max} (mm)) and corresponding focus-size (length $L_{50\%}$ (mm) and width $W_{50\%}$ (mm) of the 50% iso-SAR contour) parameters for the simulated (FDTD) and measured (IR thermography) tracks.

TCP setting	Method	SAR_{max}	$L_{50\%}$	$W_{50\%}$
Central	FDTD	(0,–,-1)	103	35
(0,0,0)	IR	(0,–,-5)	112 (+9%)	34 (-3%)
X-steering	FDTD	(31,–,0)	96	39
(+30,0,0)	IR	(32,–,0)	103 (+7%)	37 (-5%)
Z-steering	FDTD	(0,–,-50)	82	37
(0,0,-50)	IR	(0,–,-51)	87 (+6%)	38 (+3%)

Table 6.2 provides a summary of the most important parameters from Figure 6.6 and Figure 6.7. This table shows the SAR steering and corresponding focus-size parameters for the simulated (FDTD) and measured (IR thermography) tracks. The simulated SAR distribution for central settings and the focus-size parameters ($L_{50\%}$, $W_{50\%}$) are visualized in Figure 6.3. For the experimental verification of the predicted focus-size we used IR measurements due to its superior resolution and because its values correlated well with the T-probe measurements, which we assume to be more accurate. Table 6.2 shows that, using the TCP based phases, the obtained SAR focus can be steered towards the desired location with a reasonable accuracy, i.e. ∼5 mm. Further, it indicates that the corresponding focus-lengths ($L_{50\%}$) are in the range of 87-112 mm and the focus-widths $W_{50\%}$ are around 35 mm.
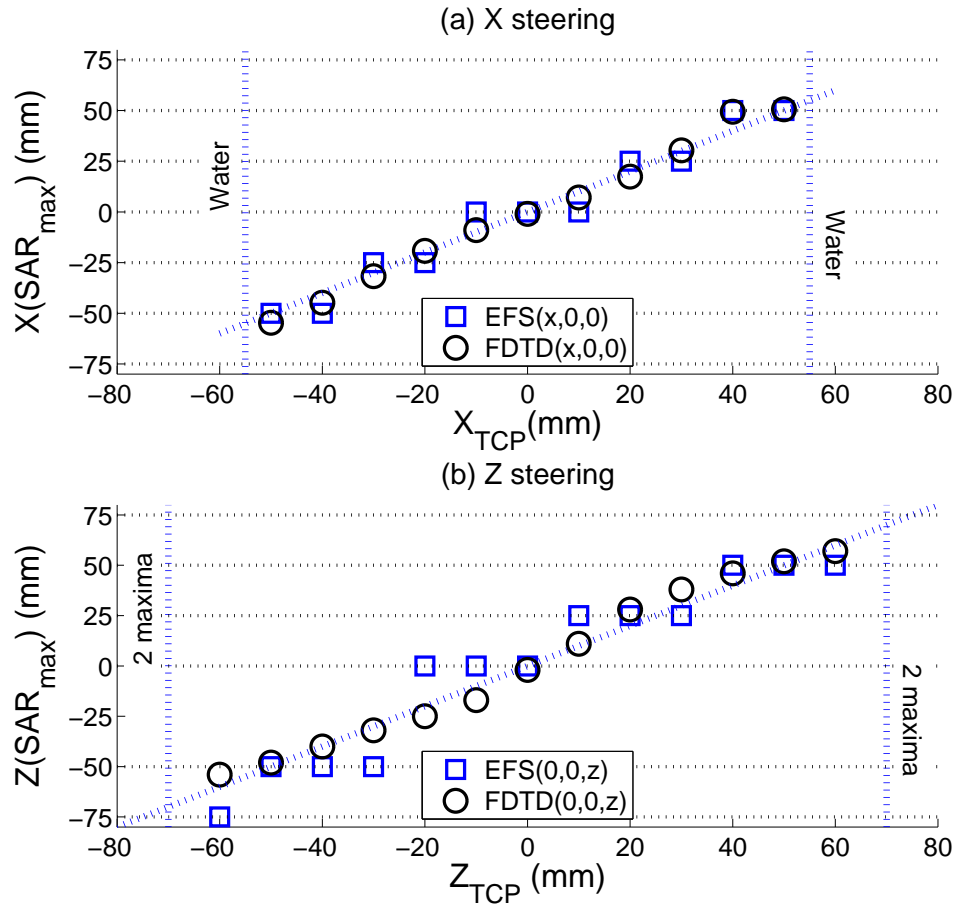
Figure 6.8: Measured maximum SAR point as function of TCP for SAR-steering in radial (a) and axial (b) directions. Locations of E-field sheet measurement points are indicated by the horizontal dotted lines and the unity curve by the diagonal dotted line. At z=-25 mm no E-fields were measured because of the design of the E-field sheets.

6.3.3 Dynamic SAR steering

We used measurements with the E-field sheet to investigate the dynamic steering possibilities of the focus since no cooling down period is required for this method. We measured the location of maximum SAR and correlated this position to the TCP settings, which is visualized in Figure 6.8 (a,b). In this figure we show the maximum SAR location for x and z-steering along several tracks. These curves show a staircase shape due to the spatial resolution of the E-field sheet and because the use of a spline-fit to find the location of the maximum was omitted. We indicated the location of the E-field sheet diodes by the horizontal dotted lines and the identity curve, indicating a perfect match, by the vertical dotted line. Both figures show a linear relation and

a high correlation between TCP location and location of maximum SAR, in both radial (x, and y due to symmetry) and axial (z) direction. This means that the focus can be accurately steered by using the TCP method to the desired location in the neck-equivalent muscle phantom. We further found that steering in the radial plane is possible in the entire phantom. In the z-direction, the focus can be steered up to 60 mm from the center. From this location a double focus distribution is obtained, i.e. the secondary focus becomes more than 50% of the maximum.

6.4 Discussion

6.4.1 Evaluation of the materials and methods

For this work we constructed a split-phantom set-up consisting of two semi-cylinders that are closed with polymer sheets. In this way the set-up provided the versatility that enabled measurements between two parts with several measurement devices and IR measurements by opening the set-up. The drawback of our approach is the possibility of air-gaps between the sheets which, especially for these high frequencies, can have a large effect on the local SAR and on the measurement accuracy. We have tried to decrease these influences by inserting some water between the sheets and some additional water pressure while the halves of the prototype are clamped together.

For the measurements we have used a muscle phantom recipe of Ito *et al.*[40]. Amounts of ingredients were used for muscle-equivalent properties ($\epsilon_r = 56$, $\sigma_{eff} = 0.8$ S/m) at 22°C. These properties, however, vary with temperature and are very sensitive to small variations in salinity. Due to the required interference of multiple sources, these SAR values depend upon the conductivity in a non-linear fashion. By carrying out simulations with different conductivity values, we found that the SAR tracks in the x-direction are strongly dependent on conductivity, i.e. the lateral normalized SAR values are decreased by 30% for a 20% decrease in conductivity. Therefore, in future measurements we expect to improve the predictability of the measurements by measuring the properties of the phantom before each measurement.

6.4.2 Evaluation of the results

Electromagnetic models are used more and more for HT treatment planning and there is a growing use of EM models to perform parameters studies for the optimization of HT applicators[50,64,86]. While the accuracy of EM modelling has increased dramatically and high resolution simulations have become possible, up to now this has not led to higher standards concerning model validations. Such a validation is a crucial step to assess dosimetry accuracy and will reduce the need for verification measurements for new applicators. For a superficial antenna, recently, a first attempt of such a quantitative validation by high resolution 3D measurements was presented

by De Bruijne *et al.*[15]. This validation, however, was for a single antenna set-up and should be confirmed for the SAR distributions with higher gradients that are typically obtained with array set-ups. For high accuracy SAR dosimetry validations of array set-ups, accurately on-site measured dielectric properties of all (phantom) materials are required. Further, an accurate measurement device is required, which in general is very expensive.

For our approach we used the availability of more accurate modeling for optimizing the entire HT applicator. To our knowledge, we were the first to use EM modeling to design an HT applicator from scratch by detailed parameter studies at frequencies above 400 MHz. In a previous publication we have explained our work dedicated to the design of an optimized antenna positioning. Further, we used EM modeling to fully optimize the reflection characteristics of a single element of the antenna array. In the present paper we have experimentally verified the feasibility of focussed heating in the neck, which has been predicted earlier[72,75], and as such to validate our approach. We further assessed the dimensions of the focus and verified the possibilities of dynamic steering. By comparing measurements to simulation we performed a qualitative verification of the predicted SAR patterns in a muscle phantom.

In this study we verified that a central focus can be obtained with two rings of six antennas each. For central settings, we determined the width of this focus as 34 mm (IR) and 35 mm (FDTD) and the length as 112 mm (IR) and 103 mm (FDTD). This difference might be due to thermal conduction, which results in an overestimation of the EFS by IR thermography. In the radial direction this size is usually $\lambda/3$[73,105], which means $\sim$31 mm in a muscle phantom, and correlates well with the values in this study. In axial direction this focus is determined by a combined effect of the distance between the antenna rings, the radius of the antenna rings, and the operating frequency[75], i.e. the wavelength in muscle. The obtained focus can be steered in radial directions towards every point in the muscle phantom. In the axial direction $(-z,z)$, extreme focus center point location is a 60 mm off-center position. For verification of the SAR profiles we used the split-phantom technique in combination with 1) glass-fiber thermometer probe measurements, 2) IR thermography using a high resolution IR camera, and 3) measurements using our Schottky diode E-field sheet. Local SAR values are determined for the first two (fiber-probes, IR) by using the power-pulse technique[32], which means that high power is required. The latter (E-field) measurements were carried out at low power. The fiber-probe measurements have the advantage of a high accuracy and they provide the possibility to monitor temperatures during heating. Further, they are non-metallic and very thin thus field disturbances are negligible. The disadvantage of this method is the required cooling time after measurement (1-2 hours) due to the high temperature gradients required. Further, multiple (multi-sensor) probes are required for a high resolution and positioning multiple probes in the split-phantom is cumbersome. IR thermography measurements with the most recent IR cameras have a high resolution, which enables to investigate, besides the size of the focus, also the shape of the focus. IR measurements share the disadvantage of long cooling times. Further, for

these measurements it is required to open up the set-up for taking an IR picture, i.e. measurements were taken typically 10s after power off. According to Samaras *et al.*[82], for effective field size (EFS) measurements, this is sufficiently short for an accurate measurement. Compared to flat-phantom EFS measurements, the distributions obtained in this publication show much higher SAR gradients and therefore heat conduction might have somewhat more influence. By comparing the thermography results to the fiber probe measurement we could show that the influence of heat conduction remains low. By using the Schottky-diode E-field sheet[46,104] we performed E-field measurements that can be performed at low power thus dynamic SAR steering with the prototype can be assessed. A major drawback of this equipment is its low resolution because it was designed for superficial hyperthermia applicator assessments in flat phantoms were the fields are more gradual. Further, in this split-phantom set-up, air-gaps may be present that considerable decrease the sensitivity of the diodes. The measured SAR values close to water from both power-pulse based methods further might have been hampered by the active water-cooling of the sides of the phantom. By the resemblance between the SAR derived from the E-field and temperature measurements, we conclude that this influence is low.

6.4.3   Quality assurance

Currently, no specific QA guidelines have been defined for our application or for newly developed applicators. Within the framework of ESHO, guidelines for ESHO protocols have been defined 1) for treatment of superficial tumours[32], i.e. locally advanced breast carcinoma, advanced neck nodes, malignant melanoma, and 2) for regional hyperthermia in the pelvic area by radiofrequency equipment[52]. In terms of (regular) assessment of the SAR pattern of an applicator, clearly different approaches are suggested. For superficial QA guidelines and assessment of applicator performance, the effective field size (EFS) and penetration depth (PD) are defined, which "should be determined by measuring the changes in temperature resulting from a brief pulse of high power"[32]. In these guidelines, the necessity for an additional characterization of the SAR pattern corresponding to a multi-element array of applicators is recognized. Further, it is mentioned that if "non-perturbing E-field probes, thermographic imaging or liquid-crystal sheet imaging" are used, they should be corroborated by measurements obtained using the power pulse technique. A requirement for using this technique is that 60s after power-on the EFS and PD should be determined. However, by finding perfect linear temperature curves, we showed that longer heating periods can be used. In the guidelines for regional hyperthermia[52], it is required for SAR distribution characterization of equipment to perform system performance regularly using the LED matrix/lamp phantom using different phase/amplitude settings, different phantom positions and different bolus configurations. The E-field Schottky-diode sheet system is compliant to all requirements but a higher resolution is required so the focus size and shape can be determined as well, i.e. $\sim \lambda/10$ instead of $\sim \lambda/4$ (at 433 MHz). Further, to obtain a more homogeneous

temperature distribution, an improvement would be to use a liquid phantom material. The required new E-field sheet system, however, requires additional research since it must be designed specifically.

6.5 Conclusions

In this paper we analyzed the ability of using a phased array hyperthermia applicator for focussed heating in the head and neck region. Firstly, we conclude that the early design of the patch antenna, in a well controlled water environment, provides an average efficiency of 94%, which is highly sufficient for our investigations. Secondly, we measured low cross-coupling between antennas in the array (maximum -22dB). Thirdly, we conclude that, using the analyzed set-up of two rings of six antennas, focussed heating in the head and neck is feasible. By IR thermography we measured a central 50% iso-SAR focus of 112 mm in axial and 34 mm in radial direction in a muscle phantom. This radial dimension is sufficiently small to allow targeted heating of advanced tumours and by de-focussing also good SAR coverage of larger tumours should be possible. The axial length of this focus is somewhat large for tumour-specific heating. However, this can result in some blood pre-heating because vessels are mainly oriented in this direction. The focus can be steered in axial (cranial-caudal) direction to maximum 6 cm from the center in the phantom. Combined with the focus size of 10 cm in axial direction, this indicates that 50% SAR coverage may be possible up to 11 cm from a central location. The actual extent of heating in a patient remains to be determined.

We found little differences between the predictions of the SAR distribution by the three investigated measurement methods. Therefore, as best system for regular quality assurance we suggest the Schottky-diode E-field sheet system. This device enables quick measurements and better control of the temperatures resulting in more predictable di-electric properties of the phantom materials. However, a modified design of the Schottky-diode E-field sheet system is required that provides a higher resolution.

Acknowledgements

CHAPTER 7

The HYPERcollar: the clinical applicator design

Abstract

The purpose of this work was to define all features, and show the potential, of the novel HYPERcollar applicator system for hyperthermia treatments in the head and neck (H&N) region. The HYPERcollar applicator consists of 1) an antenna ring, 2) a waterbolus system and 3) a positioning system. The specific absorption rate (SAR) profile of this applicator was investigated by performing infra-red (IR) measurements in a cylindrical phantom. Mandatory patient-specific treatment planning was performed as an object lesson to a patient with a laryngeal tumour and an artificial lymph node metastasis. The comfort tests with healthy volunteers have revealed that the applicator provides sufficient comfort to maintain in treatment position for an hour: the standard hyperthermia treatment duration in our center. We further established that a central focus in the neck can be obtained, with 50% iso-SAR lengths of 3.5 cm in transversal directions (x/y) and 9-11 cm in the axial direction (z). Using treatment planning by detailed electromagnetic simulations, we showed that the SAR pattern can be optimized to enable simultaneous encompassing a primary laryngeal tumour and a lymph node metastasis at the 25% iso-SAR level. The applicator enables a good control, and sufficient possibilities for optimization, of the SAR pattern. In an ongoing clinical feasibility study we will investigate the possibilities of heating various target regions in the neck with this apparatus.

7.1 Introduction

Clinical phase III trials have shown that the addition of hyperthermia (HT) to radio-therapy (RT) results in remarkably higher (complete) response rates, improved local control rates, better palliative effects and/or better overall survival rates. The possibilities of HT for improving treatment outcome without adding toxicity[20,79,90,94,95] are interesting to study in advanced H&N tumours as well.

Up to now, the application of HT in the H&N region was limited to superficial regions because of the lack of deep-heating equipment for this region[87]. In earlier investigations, phased-array approaches have been investigated to apply HT to superficial regions in the H&N area with planar or conformal arrays[45,56]. However, to the best of the authors' knowledge, no clinical phased-array based applicator for applying HT to deep-seated head and neck tumours exists. Therefore we conducted work to design and construct such an applicator for targeted heating of advanced carcinomas in the H&N region.

In earlier studies, we started with a cylindrically symmetrical set-up of dipole antennas in an infinite water environment and optimized the dimensions of this set-up specifically for targeted heating in the H&N region[72,73,75]. In those studies we se-

lected an array of twelve antennas operating at 433 MHz arranged in two rings as the optimum set-up. Simultaneously, we designed a patch antenna specific for the H&N applicator as a replacement for the dipoles of the theoretical set-ups[76]. Subsequently, we verified the SAR calculations by phantom measurements using a laboratory prototype consisting of twelve early versions of this patch antenna[74].

The good results in previous studies have led to the construction of a clinical applicator: the HYPERcollar. In the present publication we report on the HYPERcollar applicator system and its features. Further, we show the results of measurements for quality assurance purposes. Finally, as an object lesson, we illustrate the potential of the applicator by showing the mandatory patient-specific treatment planning process for an example larynx-patient, and discussing the predicted optimized SAR distribution.

7.2 Materials and methods

Three key elements have to be addressed in preparation of a semi-deep H&N HT treatment to ensure high quality. Firstly, equipment should be available that provides possibilities for obtaining good specific absorption rate (SAR) coverage of the tumour and enable SAR pattern adjustments. Secondly, these SAR patterns should be verified by phantom measurements. Thirdly, patient-specific treatment planning
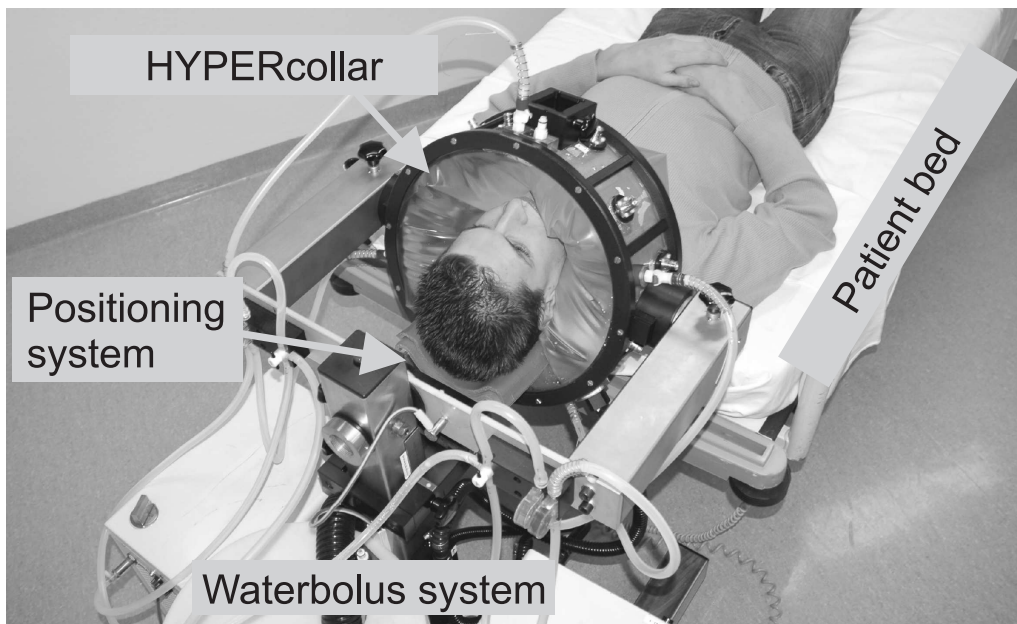
Figure 7.1: Picture of the HYPERcollar applicator system. Both patient bed and positioning system (neck support) are used to position the patient. The coaxial cables, that are normally connected to the applicator, are not shown for visibility.

is mandatory to optimize the SAR pattern and diminish the risk of thermally related toxicity. Therefore, in this section, we describe subsequently the HYPERcollar applicator design, and its characteristics, as well as the treatment planning system that is considered an integral element of the applicator.

7.2.1 Applicator system

Figure 7.1 shows a picture of the HYPERcollar applicator system. Basically, the system consists of a normal patient bed and an applicator that can be moved over the head of the patient. After proper positioning, the waterbolus of the applicator is inflated with demineralized water and the twelve coaxial cables of the power system are connected.

Power system

The power system delivers high-power radiofrequency (RF) signals with accurately controlled powers ($\pm 5\%$) and phases ($\pm 2°$) to the applicator. First, a Direct Digital Synthesis (DDS) system provides twelve coherent 433.92 MHz signals with independent phase shifts. These signals are amplified with PG70.150.2 power generators (SSB Electronic, Germany) up to 150 W. Circulators protect the amplifiers against reflected power and bi-directional couplers are used to measure both forward and reflected signals. Gains and phases are measured with twelve specially designed detectors[4], which use one of the DDS system signals as a reference. Low-loss (<0.1dB/m) coaxial cables are used to transfer the 433.92 MHz signal from the amplifiers to the C-connectors of the antennas.

HYPERcollar

The HYPERcollar consists of a transparent perspex cylinder (radius = 40 cm) covered with a fine conducting gauze forming the conducting backplanes required for the patch antennas. Twelve patch antennas in two rings[75] are mounted on the perspex cylinder. The distance between the center planes of the two antenna rings is 6 cm. The patch antennas consist of a brass patch (28.2 mm x 7 mm) oriented in alignment with the patient-axis (z-axis) and connected, close to the short side, to the extending conducting rod of a C-female receptacle connector. A low-dielectric support is placed between backplane and patch for better robustness. Details of the dimensions of the patch can be found in[76]. The entire applicator is attached to a movable trolley and can be rotated around the z-axis (patient-axis) and around the x-axis (left-right) for maximum positioning flexibility. An inflatable waterbolus is attached to the perspex cylinder for cooling of the skin and to enable an efficient transfer of the electromagnetic waves from the antennas into the patient.

Waterbolus system

Figure 7.2 schematically shows the waterbolus system and a top view of the HYPER-collar: with cross-sections through the patient and waterbolus. The demineralized water in the waterbolus is circulated and temperature controlled by two E4850 refrigerated recirculators (Bio-Rad, Microscience Division). In- and outflow points are located at every other quadrant in order to obtain maximum temperature homogeneity in the waterbolus. A special pump is used to fill the bolus around the patient in approximately 30s and the quick release valve can be used to empty the bolus in less than 5s. A small valve at the top of the applicator is used to remove the air during the filling procedure. By closing all valves, a closed water system is obtained. The recirculators can also be attached to the water vessel to heat or cool this water to the desired water temperature prior to the treatment.
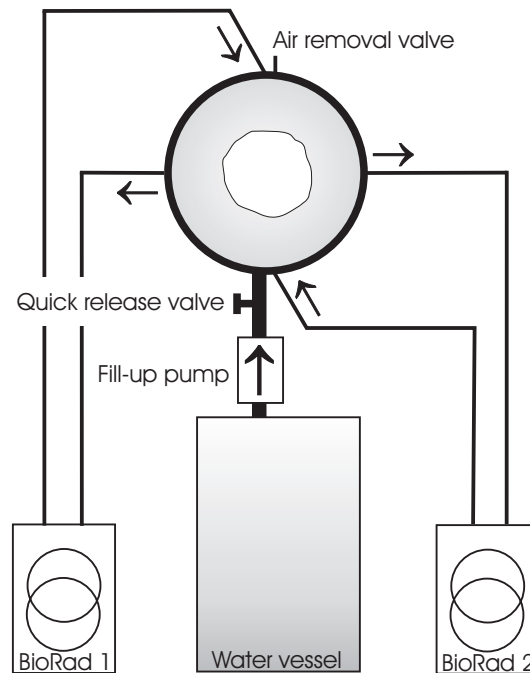
Figure 7.2: Schematic visualization of the waterbolus system. Direction of flow within the tubes is indicated by the arrows.

Positioning system

Positioning of the patient in treatment position is carried out as follows. The patient, who is laying on the patient-bed with the head over the edge of the bed, is positioned by moving the applicator as far as possible over the patient's head ($\sim$1 cm space between shoulders and applicator). Subsequently, the patient is moved to the desired position by altering the height of the patient bed and subsequently the height of the neck support. To check the position of the patient according to planned positions,

we verified the coordinates of the nose and jugular notch. Hereto we constructed a special device, including a water-gauge, that enables measurements using the origin of the applicator as a reference. After inflating the waterbolus, this positioning is verified in order to obtain the highest correspondence to the positions at which treatment planning was performed.

We assessed the level of comfort within the applicator in treatment position using five healthy volunteers, e.g. whether easily breathing remains possible. The volunteers were positioned within the applicator and subsequently the waterbolus was inflated with water. Volunteers remained in the applicator for approximately an hour.

7.2.2   Characterization measurements

Compared to the laboratory prototype set-up[74], the main differences are 1) the presence of a finite waterbolus, 2) a smaller distance between both antenna rings (6 cm), 3) a larger ring radius (40 cm) and 4) a new, more optimized, version of the patch antenna[76]. For characterization and quality assurance (QA) purposes we measured reflection and SAR patterns. The return loss P_r that is measured at the connectors of the HYPERcollar can be separated into the primary reflection of the antenna $P_{p.r.}$ and the combined secondary contributions $P_{s.c.}$ by cross coupling of the other antenna elements of the array, i.e. $P_r = P_{p.r.} + P_{s.c.}$, where $P_{s.c.}$ is the sum of the secondary contributions of the other eleven antennas. Dividing these contributions by the power that is directed towards each antenna, P_f, provides the respective reflection coefficients. Primary reflection characteristics were measured for various waterbolus temperatures to assess the temperature range in which operation is possible. The primary reflection coefficients were measured by attaching a network analyser (8751A, Agilent Technologies, USA) to the antennas and by using a centrally positioned cylindrical muscle equivalent phantom[74]. We further assessed the SAR pattern of the HYPERcollar applicator within this cylindrical phantom by infra-red (IR) thermography, as in[74]. In addition, we measured the (phase-dependent) return loss P_r for the phase settings corresponding to TCP steering in x (-60mm : 60mm), y (-60mm : 60mm) and z (-30mm : 30mm) direction, in steps of 10 mm.

7.2.3   Treatment planning

In future, we will perform treatment planning for each patient since in our opinion this is mandatory for obtaining good heating profiles and to diminish the possibility of thermally related toxicity. Therefore, we illustrate such treatment planning for an example patient with a laryngeal tumour. Further, we illustrate the potential of large target volume heating by adding an artificial lymph node metastasis and analyzing the SAR distributions within tumour and lymph node.
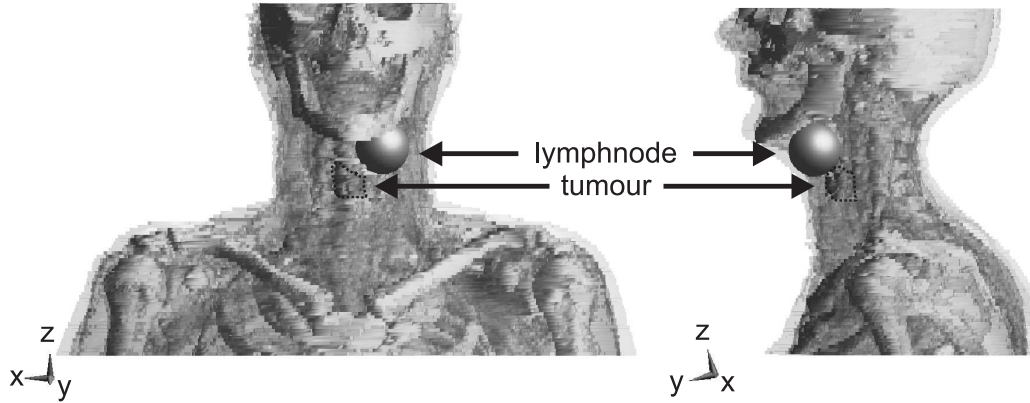
Figure 7.3: Transparent anatomy visualization in SEMCAD X. Bone tissue, the tumour and the artificial lymph node metastasis are non-transparently visualized.

Table 7.1: Tissue types and their dielectric properties at 433 MHz ($\mu_r = 1.0$).

Tissue type	ϵ_r [-]	σ_{eff} [S/m]	ρ [kg/m^3]
Air	1	0	0
Bone	13	0.09	1990
Fat	12	0.08	916
Muscle/Tongue	57	0.80	1041
BloodVessel	47	0.57	1060
BoneMarrow	6	0.03	1027
Brain	57	0.75	1039
Cartilage	45	0.60	1100
Esophagus	67	1.01	1040
SpinalCord	42	0.45	1043
ThyroidGland	61	0.89	1050
Tooth	13	0.09	2160
Tumour	59	0.89	1050

Patient model

The patient model was segmented from a CT-scan of a larynx patient that was made for radiotherapy treatment planning. Semi-automatic segmentation into different tissues was carried out by a medical doctor using a dedicated segmentation program[67] (Figure 7.3). The segmented tumour volume was 6.5 ml, which corresponds to the smallest target volume in[72]. To investigate the possibilities of heating both primary tumour and lymph node metastasis, we also defined an artificial tu-

mourous lymph node sphere (diameter = 4 cm, volume = 33.5 ml) and assigned properties of tumour to this volume. Because the CT-scan contained information of only 30 cm, we stretched the end slices of this model to increase the height of the model to the outside of the waterbolus. Tissue properties at 433 MHz (Table 7.1) for normal tissues were from Gabriel *et al.*[26]. The properties of tumour tissue were obtained by using the average di-electric value of a number of tumours as measured by Joines *et al.*[42].

Applicator modelling

We predicted the specific absorption rate (SAR) distributions in the clinical prototype applicator using SEMCAD X (Schmid & Partner Engineering AG, Switzerland). Settings for the FDTD modelling of the HYPERcollar were equal as in[74], in which we verified the accuracy of the model for a laboratory prototype. The grid was aligned to the antennas and automatically refined down to 0.5 mm at the antennas for maximum accuracy (Figure 7.4), which resulted in a total amount of 7.8 million voxels.

SAR optimization

Two methods of SAR optimization were applied and their suitability was compared. The TCP method provides a fast way of calculating the phases without the requirement of treatment planning. The second method ("Optimized SAR") requires full treatment planning but includes information of the actual geometry (applicator and patient) in the optimization.

TCP method   The first method of SAR optimization follows the method that is used in the BSD2000 Sigma-60 system[74]. For each antenna, we analytically calculated the required phase delays, using the difference in wave velocity in muscle and water, such that maximum interference occurs at the desired Target Center Point (TCP) in a cylindrical phantom. These phases are subsequently used in the set-up with patient anatomy and HYPERcollar. The amplitudes are always equal for all antennas.

Optimized SAR   For the second method, we optimized amplitudes and phases by using the procedure of Kohler *et al.*[49] to maximize optimization parameter I:

$$I = \frac{\sum_{i=1}^{N_i} S_i \cdot \sum_{t_i} SAR\{x(t_i), y(t_i), z(t_i)\}}{\sum_{j=1}^{N_j} S_j \cdot \sum_{n_j} SAR\{x(n_j), y(n_j), z(n_j)\}}, \tag{7.1}$$

in which t_i is the ith target region from a total of N_i target regions and n_j is the jth normal tissue region from N_j normal tissue regions. The total amount of SAR
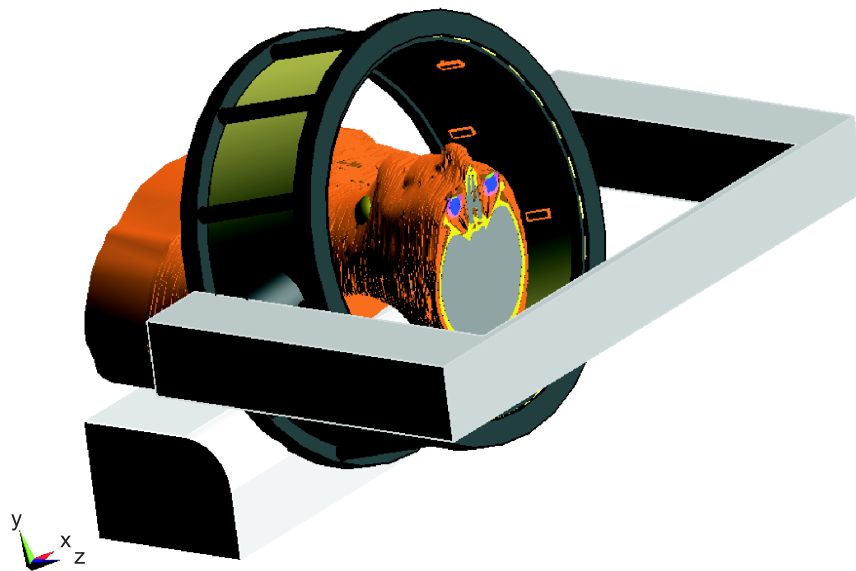
(a): Solid model
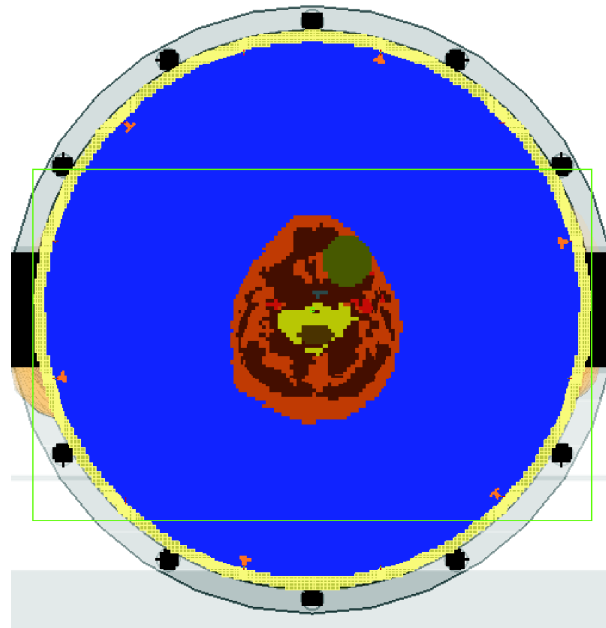
(b): Grid implementation

Figure 7.4: The HYPERcollar applicator and the patient within. The waterbolus and the upper head model extension are not visualized to show some patch antennas.

in a certain region can be increased or decreased respectively by increasing weight factors S_i and S_j.

7.3 Results

7.3.1 Comfort of the applicator

Comfort tests with healthy volunteers have revealed that the applicator provides sufficient comfort to maintain in treatment position for an hour: which will be the hyperthermia treatment duration for H&N patients in our center. We observed no breathing problems due to waterbolus pressure at the trachea, provided that the waterbolus was filled carefully. A special neck support has been constructed since the comfort tests revealed that such a support would provide more stability during filling of the waterbolus and would increase the reproducibility of the positioning.

7.3.2 Characterization measurements

Reflection characteristics
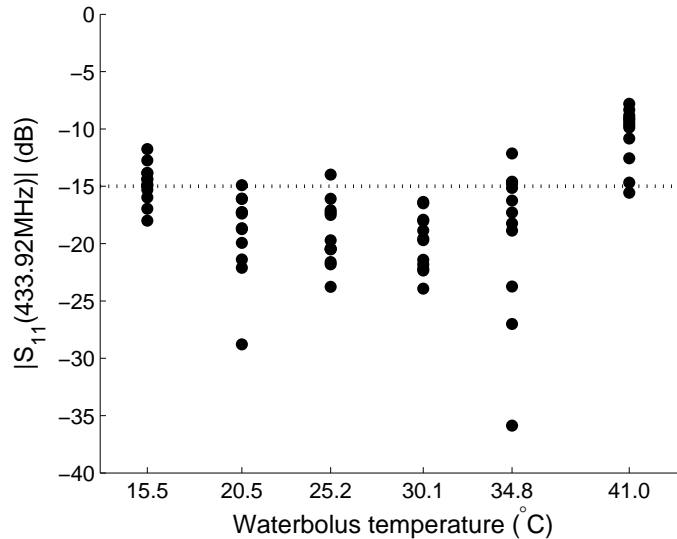
Figure 7.5: Primary reflection coefficient ($P_{p.r.}/P_f$ in dB) at 433.92 MHz for different waterbolus temperatures and all 12 antennas. A cylindrical muscle equivalent phantom was used to mimic the patient's neck.

In Paulides *et al.*[76] we have defined the expected clinically relevant range of waterbolus temperatures, i.e. between 20 and 30°C. Figure 7.5 provides the primary reflection coefficients measured using the NWA at each antenna, for waterbolus temperatures within and outside this range. The figure shows a temperature dependence, related to the change of the permittivity of the water underneath the patch, that is in agreement with the findings in the previous study[76]. The primary reflection of almost all antennas is below -15dB (3%) for temperatures between 20 and 30°C. Releasing this threshold to -10dB (10%), the applicable temperature range can even

Table 7.2: Statistics of the measured return loss P_r/P_f (%) at every antenna for TCP-steering settings.

	1_1	1_2	1_3	1_4	1_5	1_6	2_1	2_2	2_3	2_4	2_5	2_6	Mean
Mean	10	3	5	6	5	6	12	5	3	4	8	3	6
Max	31	15	19	24	28	18	41	19	11	28	20	21	23

be increased to between 15 and 35°C, while the average reflection coefficient remains under -14dB.

Table 7.2 summarizes the statistics of the measured return loss P_r/P_f for the different phase settings described in section 7.2.2. This table shows that, due to primary reflection and secondary contributions, on average 6% return loss can be expected during treatments, with peaks up to around 31%. The return loss values are found to be highest for the most ventral antennas (1_1 and 2_1). This is due to the waterbolus that bulges out more in dorsal ($-y$) locations than in ventral ($+y$) locations. Therefore, the water-air transitions are the closest to the antennas and air inclusions, due to the folds in the waterbolus, are the largest.

Measured SAR distribution

By IR measurements we have established that a central focus can be obtained in the cylindrical muscle equivalent phantom. Figure 7.6 shows the measured SAR pattern for central steering settings, i.e. TCP=(0,0,0). The figure shows a central focus very close (5 mm difference) to the desired focus position. The small asymmetry that can be observed in the x-direction falls within the assumed accuracy of the measurement.
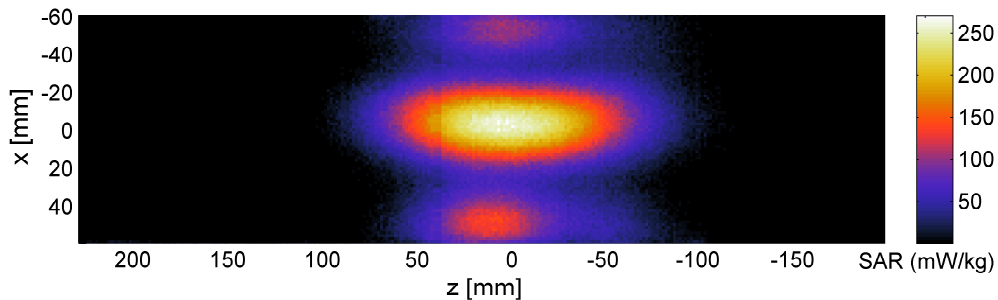
Figure 7.6: SAR distribution within the, 11.6 cm diameter, cylindrical muscle equivalent phantom for central phase steering ($\varphi_i = 0$, $i = 1 \ldots 12$) and a combined total input power of 1W.

Table 7.3: SAR steering (Direction and TCP setting (x,y,z)) and corresponding focus-size (length $L_{50\%}$ and width $W_{50\%}$ of the 50% iso-SAR contour) parameters for the IR thermography measurements. All dimensions are in mm.

Direction	TCP setting	$L_{50\%}$	$W_{50\%}$
Central	(0, 0, 0)	88	35
X-steering	(-30, 0, 0)	103	48
Z-steering	(0, 0,-30)	90	35

The length $L_{50\%}$ of the focus for central steering is around 90 mm and its width $W_{50\%}$ is 35 mm (Table 7.3). By TCP based phase adjustments, the focus can be steered to maximum 50 mm (x-direction), 50 mm (y-direction) and 30 mm (z-direction) from the origin (central steering) in the homogeneous muscle equivalent phantom. Table 7.3 shows that the dimensions of the focus change for steering in the x (and y) direction but remain equal for steering in the z-direction, i.e. the focus length varies between 88 and 103 mm and the focus width between 35 and 48 mm.

7.3.3   Predicted SAR in a patient model

SAR distributions were evaluated by using the 1g averaged Spatial Peak SAR [IEEE-1529] to remove high SAR values due to the staircase approximation of FDTD. For the SAR predictions corresponding to the different SAR steering settings we show the 25% iso-SAR volume and cumulative SAR-Volume histograms. Rather than normalizing the SAR distributions to the maximum value we calculated the SAR for 1 Watt total input power so absolute SAR values can be obtained by multiplication with the total input power of all combined antennas. Since we used a highly detailed description of the complete patch antennas, including all their dimensions, and we consider only the real radiated power, we consider these results to be predictive for the actual SAR.

25% iso-SAR volumes

The possibilities of TCP based phase-steering and optimized phase and amplitude settings for this patient are shown in Figure 7.7. The figure shows the 25% iso-SAR volume on top of the tumour, lymph node and bony structures. Figure 7.7a shows the iso-SAR volumes corresponding to TCP steering with the TCP in the middle between tumour and lymph node ("TCP @ tumour + lymph node"). This results in SAR coverage at the lymph node but the tumour is not covered. Therefore we adjusted the point of focus towards the center of the tumour. The corresponding SAR is shown in Figure 7.7b ("TCP @ tumour"). For these phase settings a much

TCP @ tumour + lymphnode

(a)

TCP @ tumour

(b)

Optimized settings

(c)

Optimized settings (S *tumour* = 10)

(d)
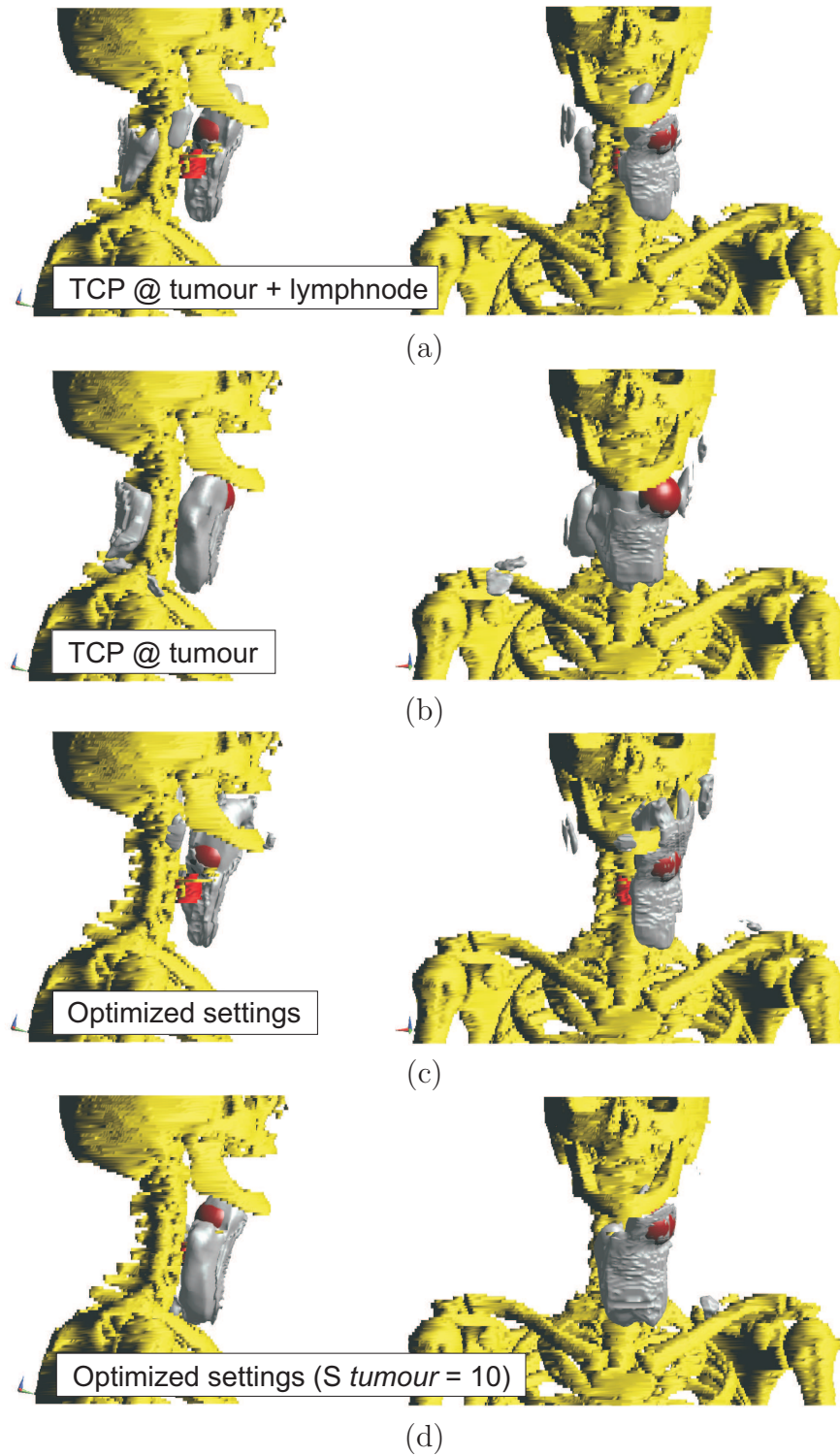
Figure 7.7: 25% iso-SAR volumes, shown in grey, for the four investigated settings. The figure further shows the bony structures (yellow) and the tumour (red) and artificial lymph node sphere (dark red)

better coverage of the tumour and an almost equal situation for the lymph node is obtained but at the cost of 1) a hotspot at the shoulder and 2) a large region of high SAR values at the back of the neck region. Figure 7.7c shows the iso-SAR volumes for optimized settings with equal selectivity values for all tissues ("Optimized settings"). The figures show selective SAR coverage of the lymph node and limited coverage of the more difficult to heat central tumour. Therefore we increased the selectivity value of the tumour (S_{tumour}) to 10 in order to obtain a better SAR coverage of both tumour and lymph node, which is shown in Figure 7.7d. This figure shows that the change in priority led to coverage of all of the tumour and almost all of the lymph node by the 25% iso-SAR volume.

Cumulative SAR-Volume histograms

To show the more subtle differences in the SAR patterns of all settings, we show the cumulative SAR histograms in Figure 7.8. Cumulative histograms specify the percentage of a certain volume that receives a specified SAR "dose". Histogram curves are shown for tumour, lymph node, central nerve system (CNS: myelum and brains), and total head volume. Figure 7.8 shows that the SAR level at the CNS is under the 25% iso-SAR value for all settings, and that high SAR values are obtained in the two target regions. Figure 7.8a and Figure 7.8b show the histograms corresponding to TCP steering. When the TCP is between lymph node and tumour, the SAR values in the lymph node are over 25% but the tumour is not covered. When the point of focus is adjusted to the tumour, the SAR values at the tumour are much higher but at the cost of lower SAR values in the lymph node. Figure 7.8c and Figure 7.8d show the histograms corresponding to optimized settings. Compared to TCP settings, these settings result in higher SAR values in the lymph node and, as a result, relatively lower SAR values in CNS. The SAR values in the lymph node volume, however, are much higher than the SAR values in tumour for equal selectivity settings ($S_{tumour} = S_{lymphnode} = 1$). The SAR coverage of the tumour can be effectively improved by a ten-fold increase of the tumour volume selectivity value, due to lower values in the lymph node and higher values in the tumour. Therefore a much more homogeneous SAR coverage of the entire target region is obtained with these settings, i.e. over 85% of all SAR values in both target regions are above the 25% iso-SAR value.

7.4   Discussion

Comfort tests with healthy volunteers have revealed that the HYPERcollar provides sufficient stability to remain in treatment position for an hour. Further, we observed no breathing problems due to waterbolus pressure at the trachea, provided that the waterbolus was filled carefully. However, we anticipate that comfort may be lower for patients with a combination of a short neck and high shoulders. Further, we still

(a) TCP @ tumour + lymph node

(b) TCP @ tumour

(c) Optimized settings
$S_{tumour} = 1$, $S_{lymphnode} = 1$

(d) Optimized settings
$S_{tumour} = 10$, $S_{lymphnode} = 1$
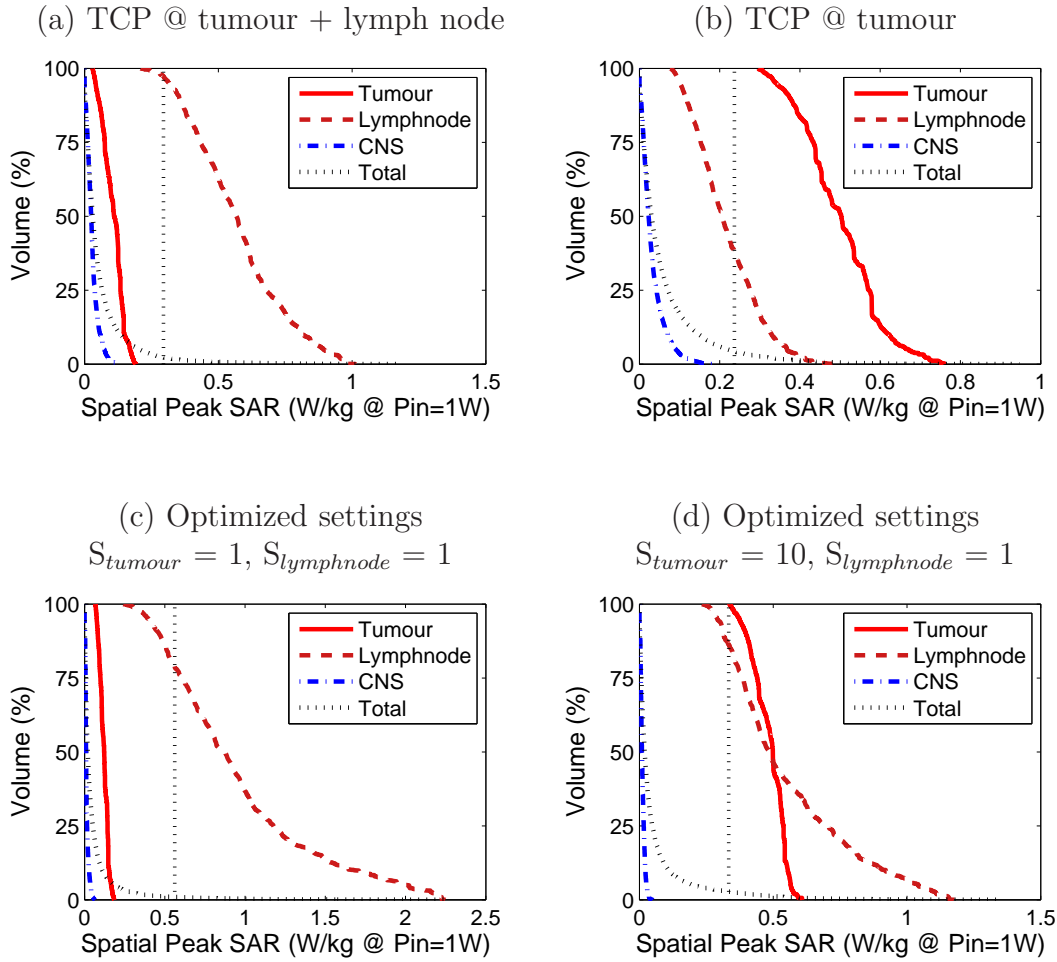
Figure 7.8: Cumulative SAR-Volume histograms for the four investigated settings using 1g-averaged Spatial Peak SAR values. The 25% iso-SAR value (25% of the maximum value in the entire patient model) is indicated by the straight dotted line

need to assess if completion of an entire session is possible for the patients that are generally older and may suffer from severely damaged skins. In a clinical feasibility study, we will investigate whether these items of concern lead to major problems. In that study we will also investigate whether heating or comfort problems can be solved by a changed applicator design or can be converted into exclusion criteria for selected groups of patients.

The primary reflection coefficients ($P_{p.r.}$) of, early versions of, the twelve patch antennas in the laboratory prototype were all beneath 10% (-10dB) for waterbolus temperatures at 23°C and 25°C[74]. The newly designed patch antenna[76] is found to perform better, with a maximum primary reflection of 16% (-12dB) for temperatures between 15°C and 35°C. However, when taking into account the contributions of other antennas, we find a total reflected power of maximum 31% and 6% on

average for measurements using a variety of phase settings and with the water temperature at 25°C. Since we expect that cross-coupling is approximately equal for different temperatures, we assume that the minor increase in primary reflection results in acceptable return loss values at waterbolus temperatures in the range of 15°C to 35°C. In the clinical applicator, we installed circulators that guide the remaining return loss towards a matched load and, since the amplifiers can deliver sufficient power, we expect no influence of these return losses on the treatment.

In an earlier study, using a laboratory prototype, we found a central 50% iso-SAR focus of 35 mm (±3 mm) in diameter and around 100 mm (±15 mm) in length[74]. However, based on a simultaneously performed parameter study[75], we decreased the distance between the two antenna rings from 8 cm to 6 cm and increased the antenna ring radius from 30 cm to 40 cm for the HYPERcollar applicator. As expected, the width of the 50% iso-SAR focus is equal for prototype and HYPERcollar. The length of this focus, however, shows a minor decrease to 90 mm while a small increase was expected. The decrease in focus length is caused by the finite length of waterbolus introducing water-air transitions that were not taken into account in the prototype set-up. We expect that the waterbolus will conform better to a patient anatomy, which has a larger average diameter and more concave shape, and waterbolus edges will therefore be further away from the region of interest. As a result, the influence of the waterbolus on the SAR pattern in a patient is expected to be lower than the influence on the phantom. Nevertheless, the waterbolus shape should resemble the actual shape as close as possible for obtaining a good match between the predictions and reality.

In this study we calculated the SAR for 1 Watt total input power so that absolute SAR values were obtained. These SAR values are considered predictive for the actual SAR since we accurately model the entire antenna. In an earlier study, we have shown that using such a model the impedance of the antenna can accurately be predicted using SEMCAD X[76]. Since the field pattern is generally a less sensitive parameter than the impedance for such a patch antenna set-up, we assume a high predictability also for the electric-field pattern. In that study[76], however, we modelled the complete connector and the transmission line while in the current study we used the commonly accepted approach to apply a voltage source at the gap between the conducting backplane and the rod of the patch antenna. By comparing these ways of modelling, we found no differences in electric field pattern and a scalar difference in power of around 15%.

The possibility of heating in the neck region has been investigated by performing treatment planning on an example patient with a laryngeal tumour and an artificial lymph node sphere. The tumour of 6.52ml corresponds to the smallest target volume in[72] and may be smaller than the general tumour size of patients suffering from advanced tumours. By adding a relatively large lymph node region at the periphery of the neck we obtained a more irregular target region that is therefore much more difficult to heat. It can be seen as an extreme case since SAR coverage was required for a maximum distance of 8.3 cm, while it was simultaneously attempted to achieve

a low SAR level in between at the healthy tissues. A high SAR at a large target volume means sufficient de-focussing possibilities and a low SAR in between the target volumes requires additional degrees of freedom. We found that selective focussing at the target area can be obtained in the transversal plane but in the direction of the patient axis (z-axis) this focus is somewhat large for target-specific heating. The tumour alignment in the transversal plane is more important since in this planes the critical tissues are nearby. Currently we are performing a clinical feasibility study in which we are investigating the feasibility of selectively heating a target region in the H&N region with the HYPERcollar applicator system.

When evaluating the obtained predictions, we faced the common problem of the inability to define the quality of a hyperthermia treatment[70]. For superficial hyperthermia the effective field size (EFS [the area enclosed by the 50% iso-SAR contour]) and penetration depth as defined in the ESHO quality guidelines[52] provide a general solution for single applicators and SAR distributions in semi-homogenous (e.g., layered) phantoms. As a prognostic factor for treatment planning in patient anatomies, Lee *et al.*[54] found for superficial hyperthermia treatment of 196 patients that 25% iso-SAR coverage was superior to 50% iso-SAR coverage. Therefore, we have focused on the 50% iso-SAR contour for phantom measurements while maximizing the 25% iso-SAR coverage at treatment planning.

Thermal predictions were not carried out since: 1) the blood perfusion rate of H&N tumours can vary up to 80-fold[106] and 2) large differences in blood perfusion rate have been measured for increasing temperatures (muscle: 0.45 - 40 kg/m^3/s)[53]. A separate analysis containing a thorough sensitivity analysis is required to shine some light on the predictive value of the obtained temperature distributions. Since our initial aim has always been to design an applicator that provides possibilities to obtain a good SAR coverage of the target volume, we have omitted thermal calculations.

7.5   Conclusions

The HYPERcollar, a newly constructed H&N HT applicator has been presented and its features has been explained. By tests with healthy volunteers we established that the applicator is sufficiently comfortable for a healthy person to be in treatment position for one hour.

From the characterization measurements we conclude that the reflections remain sufficiently low within a waterbolus temperature range of 15-35°C. By IR thermography we measured a central 50% iso-SAR focus of around 90 mm in axial and 35 mm in radial direction in a muscle equivalent phantom.

Treatment planning showed that the SAR pattern can be shaped such that simultaneous 25% iso-SAR coverage of a deep-seated tumour and a superficial lymph node is possible for a challenging case. Future research, applying heat sessions to patients, will be used to verify the possibilities of deep heating of arbitrarily shaped target regions in the H&N area.

Acknowledgements

CHAPTER 8

First result of the phase I study

8.1   Introduction

In the previous chapter we described the HYPERcollar design and showed its possibilities for heating a primary tumour and a large lymph node metastasis. The next step of the project and the first step of clinical evaluation is a Phase I study on whether the HYPERcollar applicator system can be used to adequately heat primary tumours or primary tumour plus lymph node metastases simultaneously. In this chapter we report on the first patient in the Phase I study: a patient with laryngeal cancer to whom we applied hyperthermia with the HYPERcollar. In this chapter we present the results of treatment planning, the HT session and the measured temperatures.

8.2   Materials and methods

8.2.1   Case description

The HYPERcollar was tested in a 82 year-old male patient with a squamous cell carcinoma of the larynx ($T_3N_0M_0$: a primary tumour without lymph node or distant metastasis). There were no contra-indications, i.e. there were no metallic implants and he was treated without concurrent chemotherapy because of his advanced age and general condition. He gave informed consent, i.e. after extensive information concerning the study he agreed to participate.

In 1972, he underwent lymphadenectomy (removal of a gland), for unretrievable reasons, in the left side of the neck and in 1973 a strumectomy (removal of the thyroid gland) was performed. In 1998 a T1a glottic laryngeal carcinoma was diagnosed for which he received a CO_2 laser treatment. Since then, he had a hoarse voice so that visual contact was required for communication. In 2007, he was diagnosed with a glottic laryngeal carcinoma for which he was treated with RT, 36 fractions of 2 Gy, 5 fractions weekly. He was in a relatively good physical shape but indicated to suffer from lumber pain since October 2006. The HT session was given after the 8th RT fraction. After the HT session, a spondylodiscitis Th12L1 was diagnosed causing the lumber pain in the back.

A CT scan was made for RT treatment planning of which the quality turned out to be poor, i.e. the patient was not lying straight and one shoulder was lifted a little towards the head. This CT also showed that the patient had a relatively short neck but a close-to-average diameter (11.7 cm).

8.2.2   Treatment planning

A standard H&N radiotherapy planning CT was used to differentiate between tissues. With this, a patient model ("segmentation") was constructed that is visualized in Figure 8.1. This procedure is semi-automatic, i.e. discrimination between areas

of exterior, fat, muscle and bone is automatic and tissues such as cartilage, white matter and gray matter are assigned manually. This segmentation, combined with a CAD implementation of the applicator, was imported in SEMCAD X (Figure 8.1). With this we calculated the electric fields in the patient for each antenna.
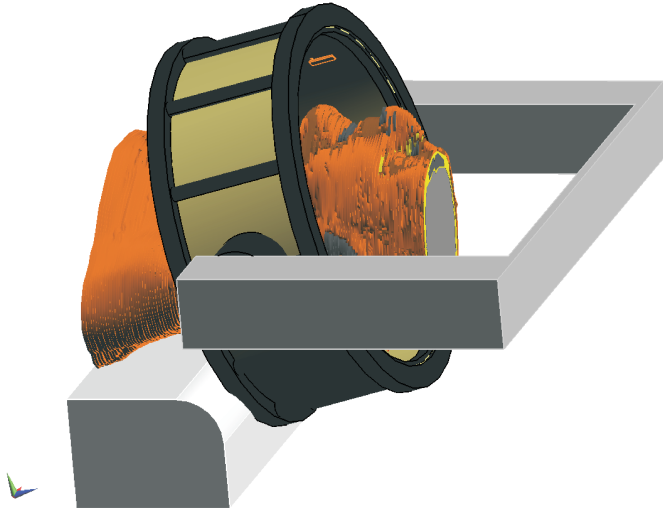
Figure 8.1: Visualization of the solid model in SEMCAD X of the patient within the HYPERcollar. The waterbolus is omitted in this visualization for a better visibility of the patient model and to show one out of the twelve patch antennas.

For obtaining the relative amplitude and phase settings to be used in the session we used two strategies. The first strategy is the commonly used target-center-point (TCP)-based steering, which is commonly used in hyperthermia, since it provides the possibility of dynamic steering during treatment. Secondly, we apply an automatic optimization routine (see page 106) that results in the theoretical optimal SAR pattern.

8.2.3 Procedure

Radiotherapy was applied to the primary tumour and lymph node stations according to standard procedures. Before the hyperthermia session, the skin showed no sign of radiation toxicity. The patient reported that his back pain had become serious; due to which he had difficulties to move. The patient was instructed to mention any pain or unpleasant feeling during the heat session, which might be the result of a hot spot. He was further assured that the treatment would be interrupted when he would request so.

Placement of thermometry catheters Immediately before the session, a closed-tip catheter was placed, through the nose, in the esophagus near the tumour. Sec-

ondly, such a catheter was placed interstitially under CT-control in muscle tissue with similar SAR as the spinal cord, i.e. "myelum indicative". After catheter placement, a CT scan was made to document the location of this catheter tract. Due to swallowing problems, the esophagus catheter was re-inserted after this CT was taken so locations had to be estimated. Four-point thermometry fibers, Takaoka FTP1 standard sensor probes (Takaoka Electric MFG Co. Ltd., Japan), were placed in these catheters. Figure 8.2 shows the locations of the thermometry points inside the solid model in SEMCAD. We excluded probe 4 from the analysis since it was not within tissue, i.e. in the analysis we found that it was located at the transition from skin to waterbolus.
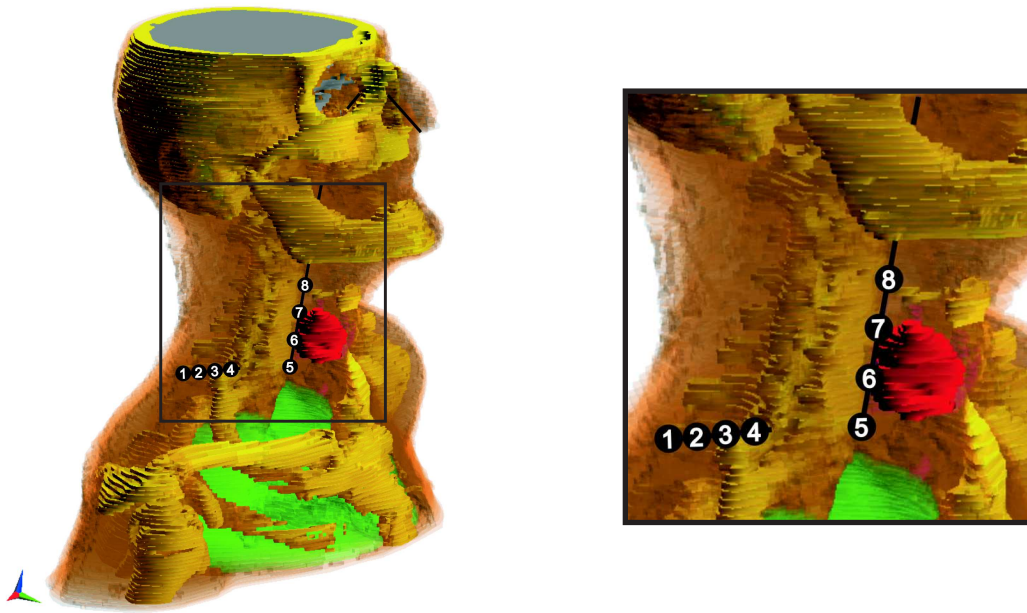
Figure 8.2: Locations of the interstitial catheter and esophagus catheter and respective measurement locations. Probes 1 and 2 provide myelum indicative temperatures, probes 6 and 7 are tumour indicative and 3, 5 and 8 are in healthy tissue.

Heat session In the hyperthermia treatment room, the patient was placed on the, comfortable, bed. Subsequently we positioned the patient as far as possible within the applicator in accordance to the planned position. The thermometry probes were placed within the closed-tip catheters, on the skin and at inflow and outflow of the waterbolus. The waterbolus was filled with demineralized water which was circulated at a temperature of 28°C.

During the heat session, according to our phase I protocol, total power was increased untill one of the constraints was reached:

- 43°C measured in a tumour indicative measurement point.

- 43°C measured in normal tissue.

- 40°C measured in a myelum indicative measurement point.

- A pain complaint by the patient. The relation of this complaint to the applied power is tested by immediately turning the power off and observing the development of the pain.

Heart rate was continuously monitored, during the session, by a pulse-oxymeter clip placed around a finger. Power and phase settings per separate antenna were controlled with the power system (Section 7.2.1).
In order to test two ways of steering we divided the heat session in two parts. For the first part we used TCP settings for the powers and phases and the second part the optimized power and phase settings. In the first part we gradually increased power in steps of 30 W until one of the limitations was reached. In the second part we used the last power settings of the first part and again continued increasing in steps of 30W.

In vivo measurement of the SAR We performed power-pulse measurements to assess the local SAR at the measurement locations, which at a later stage can be compared to the predicted SAR values. Hereto, the change in local temperature is measured while switching on high power or switching off the power at a steady-state temperature. The local SAR is calculated from the temperature rise or decay using:

$$\text{SAR} = c \cdot \frac{\Delta T}{\Delta t}, \tag{8.1}$$

where c is the specific heat capacity of the tissue (muscle tissue is assumed: 3.60 kJ kg^{-1} K^{-1}), ΔT is the local temperature rise [K] and Δt is the corresponding heating time [s].

8.2.4 Goals of the heating session

In the phase I study protocol, the following goals of the heating sessions were defined. The most important aim of the heating session was to achieve temperatures above 39°C at all measurement points in the gross tumour volume and as such demonstrate the possibility of deep heating with the HYPERcollar. Secondly, the level of comfort of the applicator was assessed by investigating whether a full session of an hour can be applied. The third aim was to encompass the gross tumour volume by the 25% iso-SAR volume as predicted by treatment planning. Fourthly, we investigated the

predictive value of HT treatment planning by comparing the SAR measurements to predicted SAR. Lastly, acute HT toxicity was assessed immediately after the session and on the next day.

8.3   Results

8.3.1   Evaluation of the heat session

Figure 8.3 shows the measured temperatures and total power as a function of time after the first power on. The treatment session was started with TCP based phase and equal amplitude settings. For the second part of the session (after the dash-dot line) we used phase and amplitude settings for which the optimum SAR distribution was calculated.

The session was started by gradually increasing power untill 340 W of total power, which was reached after around 15 minutes. At this time the patient complained about pressure at the location of the cricoid cartilage. Power was turned off to investigate the relation of the complaint to power. After some time, and after releasing some of the water from the waterbolus, the pressure sensation diminished. With the new waterbolus shape we could further increase power up to 400W. With this power, temperatures of 39°C and 39.4°C were reached at tumour indicative points. Myelum indicative temperatures remained under 39°C and normal tissue temperatures under 40°C.

After 26 minutes, the patient complained a second time of pressure at the cartilage. Therefore we decided to continue at optimized settings. Hereto we emptied and refilled the entire waterbolus and started using optimized settings (t = 37min). With these settings we could increase power till 350 W but at that point the maximum power of channel 1 (antenna 1_1) was reached. Therefore we stopped increasing the power and finished the session with this amount of power. After some time, temperatures in tumour indicative locations of 40°C and 40.6°C were obtained. The temperatures in myelum indicative points were under 38.6°C and normal tissue remained under 40.6°C and this temperature was reached only close to the tumour.

Tolerance and toxicity   The heating session was well tolerated by the patient and the session could be completed without major discomfort. Both after the session and the next day, we found no HT toxicity.

Performance of the antennas   By analyzing the measured forward and reflected power we found that the antenna performed well during the session, i.e. reflections were generally under 10%, although for some very short moments higher reflections were measured ($\sim$30%).
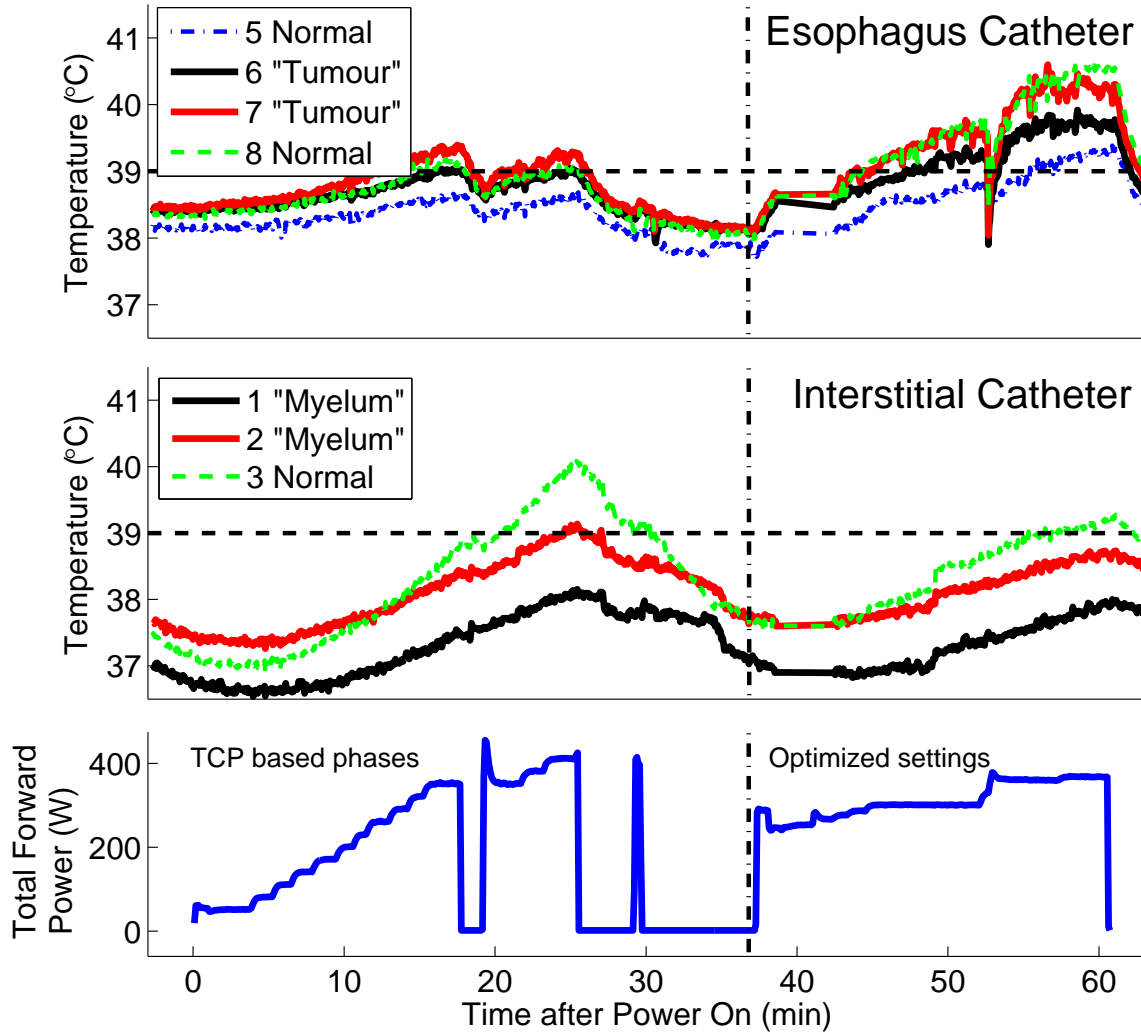
Figure 8.3: Temperature measured in the esophagus and interstitial catheters and corresponding total power level as function of time after the start of treatment. For the first part of the treatment we used TCP based phases and equal amplitude settings. For the second part of the treatment (after the dash-dot line) we applied optimized power and phase settings.

8.3.2   SAR analysis

Predicted SAR

SAR distributions were evaluated by using the 1g averaged Spatial Peak SAR [IEEE-1529] to remove high SAR values due to the staircase approximation of FDTD. Figure 8.5 shows the SAR distribution corresponding to optimized power and phase settings with specificity factors $S_{tumour} = 1$ and $S_{myelum,brain} = 10$. Figure 8.5 shows that the target region is well covered by the SAR focus, i.e. the tumour is not visible in Figure 8.5b since it is completely covered. Further, Figure 8.5b shows that a small region of high SAR is obtained at the ears as well. Figure 8.4 shows the cumulative SAR-Volume histogram. For this figure, instead of normalizing the SAR distributions to the maximum value, we calculated the SAR for 1 Watt total input power, so absolute SAR values can be obtained by multiplication with the total input power of all combined antennas. The figure shows that 90% of the tumour volume is above the 25% iso-SAR value. Further, the SAR values in the entire central nerve system (CNS: myelum and brains) are very low, even below the 5% of the maximum SAR value.
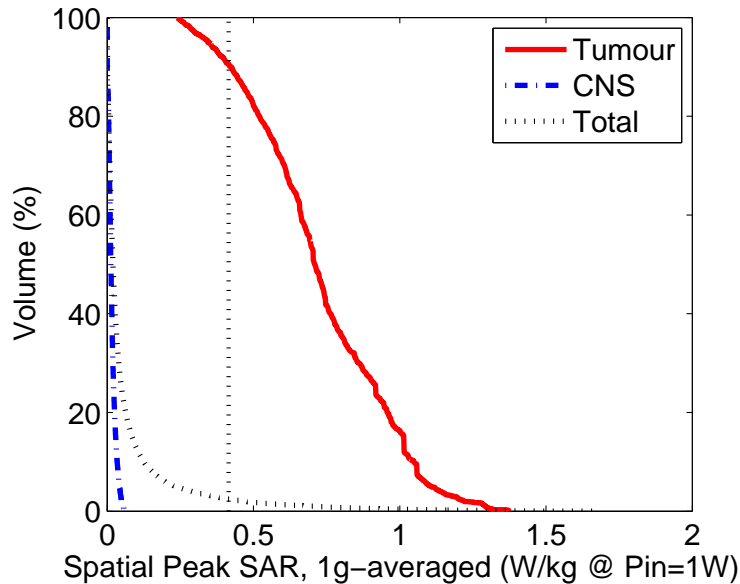
Figure 8.4: Cumulative SAR-Volume histogram for tumour tissue, CNS and the total head corresponding to optimized settings ($S_{tumour} = 1$, $S_{myelum,brain} = 10$).
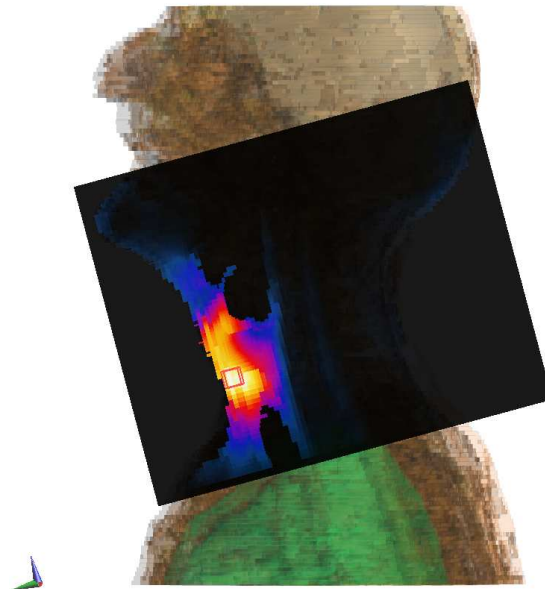
(a) Cross-section
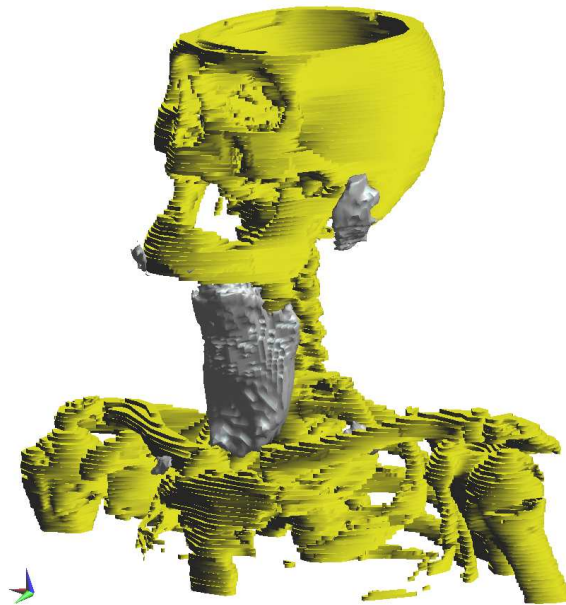
(b) 25% iso-SAR volume

Figure 8.5: Visualizations of the SAR distribution from treatment planning corresponding to optimized settings ($S_{tumour} = 1$, $S_{myelum,brain} = 10$). The square in the cross-section shows the location of maximum SAR and the size of the averaging volume to calculate Spatial Peak SAR.
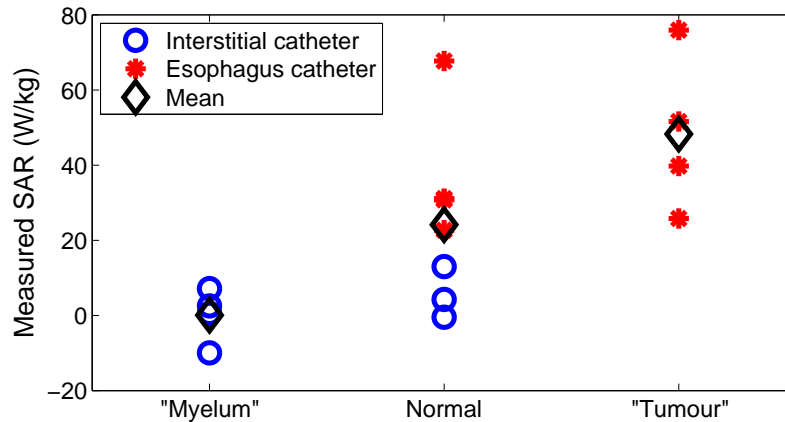
Figure 8.6: Measured SAR values at 17 (TCP phases) and 60 (Optimized set-
tings) minutes after power on (Figure 8.3) as a function of tissue
type. Measurement locations are clustered in myelum indicative, nor-
mal and tumour indicative tissue points.

Measured SAR

Figure 8.6 shows the SAR values that are calculated from the decrease in tem-
perature for TCP based phase settings at 17 minutes after start of the session, and
optimized settings at the last power off, 60 minutes after the start. This figure shows
that, on average, the highest SAR is measured at tumour indicative locations and
the lowest at myelum indicative locations. Further, all high values in normal tissue
are measured within the esophagus catheter: close to the tumour, whereas the low
values are measured in the interstitial catheter: close to myelum.

Comparison measured and predicted SAR

Figure 8.7 shows the simulated and measured SAR tracks for the measurement points
inside the interstitial and esophagus catheter. This figure shows that the correlation
between simulated and measured SAR values is much better for optimized settings
than for TCP based phase settings. The accuracy of the SAR measurements for TCP
phase settings is probably seriously affected by the non-equilibrium temperatures,
which obviously has the largest influence for the low SAR values within the inter-
stitial catheter. For the optimized settings, especially for the interstitial catheter,
the resemblance between measured and simulated SAR is quite good. Further, it
seems that all measured SAR values in the esophagus are too low. These low values
are probably caused by air flow cooling during breathing and swallowing and a bad
contact between probes and tissue. Also, the local specific heat capacity may be
different from the approximated value of muscle. Finally, there is a 3cm difference
between the measured and simulated location of the maximum SAR. The cause of
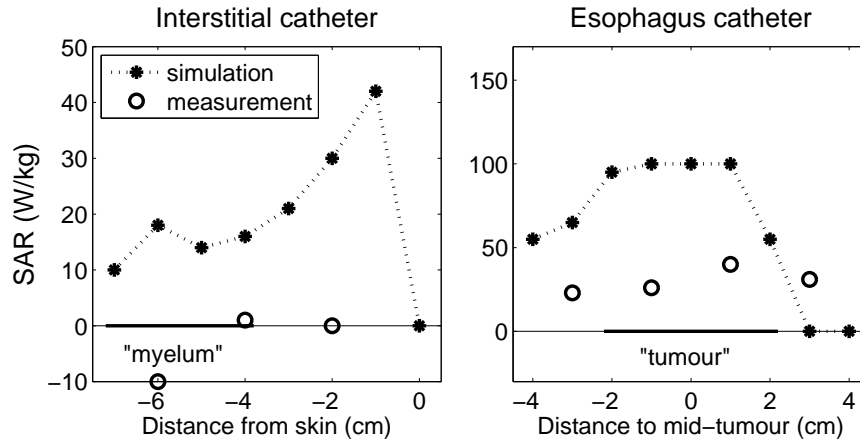
(a) TCP based phase settings
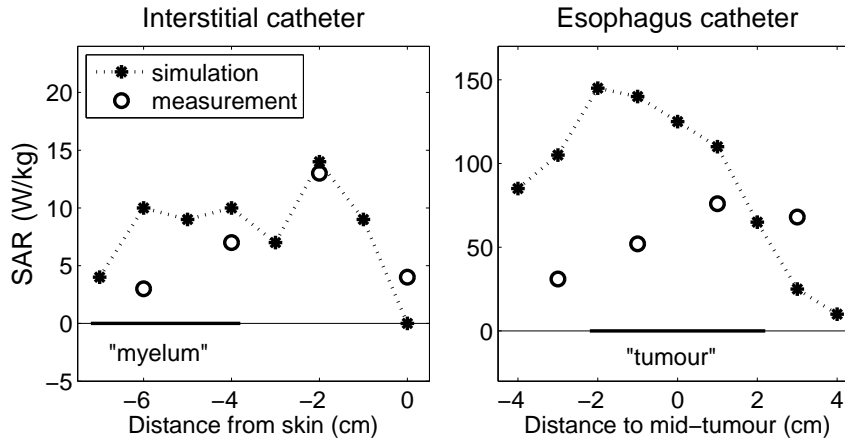
(b) Optimized settings

Figure 8.7: Comparison between simulated (1g averaged spatial peak SAR) and measured SAR tracks for the measurement points inside the interstitial and esophagus catheter. Tracks correspond to **TCP** based phase settings with **equal** power settings or **optimized** power and phase settings.

this difference remains to be determined but due to the lack of a CT including the intraluminal catheter it was very difficult to accurately assess the axial locations of the measurement probes. In future we expect to be able to circumvent the problems so the track can be determined more accurately from the CT.

8.4 Discussion

In this chapter we report on the first patient within our phase I study into the possibility of heating tumours in the head and neck region with the HYPERcollar.

The first goal of the phase I study is demonstration of the possibility of deep heating by measuring temperatures above 39°C. We measured temperatures up to 40.6°C at tumour indicative measurement points and all myelum indicative temperatures remained below 39°C, and below 38.6°C during application of the optimized settings. The high values close to the tumour were obtained for optimized settings at the end of the session and the limitation at that point was the maximum power output of one of the amplifiers. We expect to be able to circumvent this problem by ensuring that the power is distributed more over all antennas.

A difficulty in the temperature measurements, and therefore also SAR measurements, is knowledge of the exact measurement location that is important due to the large gradients in the SAR patterns corresponding to the high frequency: 433 MHz. This problem is the most relevant for the temperature measurement probes in the esophagus catheter since the interstitial catheter was inserted under CT guidance. For the esophagus catheter we have no exact information on its track and this catheter can move relatively freely within the esophagus. Therefore, the exact (x/y) positioning and axial location are difficult to reconstruct.

We used only temperature measurements at power off to determine the SAR since the measurements at power on were too much biased due to 1) a too small power increase, 2) a too slow power and phase control loop. Only for optimized settings we obtained an equilibrium so only for these measurements we obtained the highest possible accuracy. However, if we do compare the SAR measurements of TCP and Optimized settings we find the better performance for optimized settings, i.e. the SAR values close to the tumour are measured to be higher. The SAR values at myelum indicative points using TCP settings seem to be within the measurement accuracy, due to the non-equilibrium of the temperatures that decrease the accuracy of the measurements for these low values.

By treatment planning we could show that 90% of the tumour volume can be encompassed by the 25% iso-SAR contour for optimized settings. Verification of the validity of treatment planning in this patient was hampered by the low amount of measurements and their quality but the regions of the highest and lowest SAR values were well predicted.

With respect to the comfort assessment, we found no problems for the patient to finish the heating session. On one hand this patient was an ideal case since he was highly motivated to contribute to science, on the other hand though he suffered from pain in the back and therefore had difficulties with moving and there were problems with positioning on the CT table and HT bed. Nevertheless, lying on the bed with the neck in the applicator was comfortable. Therefore, we anticipate that for all patients the level of comfort will be sufficient.

8.5   Conclusion

In this chapter we have described the heating session of the first patient of the Phase I study. During the session, we measured temperatures between 39.6 and 40.6°C at tumour indicative locations and low temperatures (< 38.6°C) at myelum indicative locations. Therefore, we conclude that tumour selective heating was obtained in this patient by using the HYPERcollar. We found that the level of comfort was sufficient for this patient to endure the full treatment length: an hour. Further, by treatment planning we could show that 90% of the tumour volume could be covered by the 25% iso-SAR contour. Lastly, we found no evidence of hyperthermia related toxicity immediately after treatment and the next day. We conclude that, although we experienced problems since this was the first patient, we have succeeded in all goals of the phase I study in this session.

CHAPTER 9

General discussion and perspectives

9.1 General discussion and perspectives

9.1.1 Evaluation of the design approach

We have approached the design of a phased array H&N HT applicator by starting with a simple arrangement and stepwise increasing the complexity of the model. Hereto, we performed parameter studies to provide insight in the influence of all individual parameters on the SAR distribution. The parameters were clustered into three groups. From the inside to the outside of the phased array hyperthermia applicator these are: 1) anatomy, 2) antenna array and 3) waterbolus related parameters. The parameter studies effectively increased the knowledge on relevant parameters, which formed a good foundation for the choices that had to be made. Investigations into the waterbolus related effects have focussed on conceptual steps, as these effects depend heavily on practical constraints. An extensive analysis of these effects requires as starting point information on the actual waterbolus shape during HT sessions.

During the last decade, EM modelling has increased substantially in terms of accuracy as well as in possibilities for fast computations using large computational domains. Therefore, it has become possible to use the exact geometrical applicator descriptions making the current models as predictive as experimental measurements. As a result, time-intensive experimental verifications can be avoided and an applicator can be designed using virtual prototyping. In this research we performed extensive theoretical parameter studies. Using their results, we were able to converge much faster to a final design since they enabled limiting the amount of verification experiments that were required. We constructed only one laboratory prototype that we used to verify focussed heating and steering possibilities in the neck. By these measurements, we further showed that the FDTD model is very suitable to fast and accurately predict the EM distribution for harmonic signals. Further, by virtual prototyping we studied the benefits of new antenna concepts.

Our approach also differed from previous applicator design approaches in the fact that we aimed at a site-specifically designed applicator. Up to now, EM models were not sufficiently predictive so parameter studies were limitedly performed and hyperthermia applicators were generally firstly designed and secondly assessed for its applicable sites. Our approach, of using theoretical studies, enables a fast convergence towards the final design. However, the use of this site-specific design approach does require a better definition of the problem since the quality of the final design is highly dependent on the defined boundaries and demands for the applicable area. In a medical environment, most projects are multi-disciplinary and therefore their success is very dependent on the joint efforts of all people involved. A major challenge for a design and construction team is to involve medical partners, that will be the end-users, at an early stage so constructive discussions can be used to select the best approach. In our project, we found that it is very difficult for all project members to imagine relevant topics concerning the quality of the HT treatment during the

abstract first phase of the design process. In many cases, design demands became clear after the set-up was built but by then the project had advanced to a stage that major efforts were required to modify the design. The solution would be to strive for providing even more information to all partners. When informed well, every member of the team can exploit his/her specific knowledge in the discussions on the major choices which would surely enhance the final outcomes of the project.

9.1.2   Evaluation of the design

Theoretical investigations

Extensive parameter studies have been used to find the optimum set-up for heating in the neck. In Chapter 3 we established that, while the anatomy has a clear influence on the shape of SAR pattern, no major changes in focus location are introduced for central phase settings. Further, the SAR patterns within the cylindrical phantom are comparable to the absorption patterns predicted in 3D models. In Chapter 2 and 4 we found that the main parameter of interest for central heating in the neck is the operating frequency. Secondly, the number of antennas and antenna rings were found to be important as well for SAR focussing. The heating profiles and SAR steering possibilities of the theoretically designed array were experimentally verified, as described in Chapter 6, in order to assess the predictive value of the model and to validate our approach. By conducting IR thermography measurements on a laboratory prototype we measured a central 50% iso-SAR focus of around 90mm in length and 35mm in diameter in a muscle phantom. In Chapter 5 we designed a special patch antenna as a replacement for the dipoles used in the parameter studies. In the parameter studies, we separated waterbolus effects from array related influences on the SAR pattern. Of course, it is difficult to completely separate waterbolus related influences from array related influences, especially at bolus-air transitions[38][16]. However, waterbolus shapes are difficult to prescribe clinically and they highly depend on practical limitations. We chose to observe the shape that leads to the highest convenience for the patient and include this shape in the model. Chapter 7 shows that a good focus is obtained in the applicator with a certain bolus size. However, more research is needed into the actual effects that the finite-sized waterbolus has on the SAR pattern.

Antenna design

We have investigated the application of a probe-fed patch antenna design in a phased-array H&N hyperthermia applicator. This design has several advantages over the antennas currently used, i.e. waveguides and dipoles. The main advantage of the probe-fed patch design is the direct feeding with a coaxial cable, i.e. no matching circuit is required. This leads to easier, as well as more accurate, modelling and also to more robustness and a higher efficiency. By performing characterization mea-

surements we found that the reflections remain sufficiently low within a waterbolus temperature range of 15-35°C. During treatment sessions and measurements, however, we measured a much higher reflection due to cross-coupling, i.e. irradiation by the other antennas, but never above the tolerance limits of the power amplifier system.

9.1.3   Evaluation of the HYPERcollar applicator system

The head and neck region is characterized by many small in diameter structures and large cooling vessels. Applying a good HT treatment to this region is therefore a challenging task. In this project we have designed an applicator that has twelve antennas and, consequently, has 23 degrees of freedom (power and relative phase of all signals). Too many for intuitive settings and therefore highly detailed patient-specific treatment planning is mandatory to find the optimum settings for these channels. This need is even higher for dual or large target regions. Therefore we used SEMCAD X, a highly detailed treatment planning program, that enabled to accurately model the applicator and the patient's anatomy. By initial verification measurements we showed that the SAR pattern predictions correlate well with the measurements and that dynamic steering is adequately predicted. Treatment planning results further show that the antenna array design provides sufficient degrees of freedom: it is possible to optimize the SAR pattern such that heating the primary tumour alone but also simultaneous heating of primary tumour and a large lymphnode appears to be possible. In the transversal plane, selective focussing at the target area can be obtained but in the direction of the patient axis this focus is somewhat large for target-specific heating. This smaller dimension of the focus in the transversal plane is an important feature since, in this plane, the critical tissues are nearby and better selective heating is required.
By comfort tests with healthy volunteers we observed no breathing problems and for these volunteers it was feasible to remain in treatment position for an hour. By using a special filling pump the waterbolus can be filled in approximately one minute but special care has to be paid to the removal of the air. After filling the waterbolus, the valves are closed and a closed water system is obtained containing a much smaller volume of water. A limited water volume is relevant to shorten the time needed to change the watertemperature. Further, a closed water system requires only little pump strength for circulating the water so low-pressure pumps are sufficient, which improves the safety of the system.

Results of the first HT session

By application of a HT session to the first patient of the currently running phase I study we found that the level of comfort of the applicator was sufficient for this H&N patient. In this session we showed that in all tumour-indicative measurement points, in a catheter close to the tumour, effective temperatures could be obtained. Further

we managed to keep myelum indicative temperatures low. Heart-rate remained equal during the entire session and we observed no toxicity.

9.1.4 Future work and perspectives

Applicator improvements

A major item in the fast, accurate and comfortable application of head and neck hyperthermia is the controllable and reproducible positioning of the patient in treatment position. In the current design this item has received little attention and, at present, positioning is still cumbersome. In the future, improvement of the positioning process deserves attention because, amongst others, the level of comfort and required effort during positioning determines the stress of the treatment and the amount of personnel that is required.

As a starting point for the applicator design we aimed at selecting a single design for all locations in the neck. By using an optimizer to automatically optimize the SAR pattern we found that generally the powers of the antennas in the neck (in dorsal direction) are set to 0. These settings were probably obtained because the target regions that we studied were ventral to the myelum while the SAR in the myelum had to be minimized. In case target regions are always ventral to the myelum, more optimized antenna arrangements may be possible.

Although the waterbolus was as small as possible, still changing the waterbolus temperature is found to be relatively slow and needs good planning in advance. Additional research, using a thermal model, needs to be performed to investigate the effect of the waterbolus on the temperature pattern and to establish guidelines. Another difficulty forms the shape of the waterbolus which varies substantially and may influence the SAR pattern. The exact influence of this shape on the SAR pattern remains to be determined.

A last item that is indirectly related to the design of the applicator but very important for future work is the construction of a set-up for quality assurance (QA). In Chapter 6 we have chosen a set-up including the Schottky-diode E-field sheet system as most optimum for QA. This device enables quick measurements and can be performed at low power resulting in very small temperature variations and, as a result, in more predictable di-electric properties of the phantom materials. Future research into a modified design of the Schottky-diode E-field sheet system should provide a higher resolution and reduction of air-gaps and therefore a better knowledge of the SAR distributions that can be obtained with the HYPERcollar.

Thermometry during treatment

An important issue for a high quality treatment is knowledge of the applied dose. For a hyperthermia treatment, this actual dose remains difficult to define, and current research focussed on the influences of blood flow and increased oxygenation.

The process of finding the treatment determining parameters may well be boosted if 3D thermal data becomes available. Therefore, assessment of the 3D temperature distribution during treatment is one of the biggest challenges that remains to be solved. Up to now, most hyperthermia centers rely on a limited amount of temperature measurements within intraluminal or interstitial catheters. Probably the best way to obtain temperature data, however, is using non-invasive thermometry techniques (NIT)[103]. Therefore, extensive research is directed in the measurement of the 3D thermal distribution by MRI measurements. This technique is promising but requires the availability of high-cost MRI equipment. Two other NIT methods are ultra-sound (US) or microwave imaging (MWI). These techniques are not very well established and still require fundamental research. Another option is to further improve treatment planning and use patient-specific thermal models for predicting the temperature in the patient. This pathway however requires a lot of work on model validations and subjects like improving QA, improving patient positioning, acquisition of the electromagnetic and thermal model and knowledge of the variability of dielectric and thermal properties of tissues. If all these requirements are fulfilled, and one can assure SAR dose, then treatment determining parameters can be investigated in vivo, which probably will result in a major boost in the required knowledge for finding the ultimate goal of the treatment.

Clinical perspectives

Application of HT to other sites in the H&N Physically, the potential of the applicator for other sites is limited by the amount of penetration depth required for the specific site. The applicable areas are thus determined by the concave shape of the head and neck region, i.e. widening diameter towards shoulders and head. Further, a practical constraint is that during treatment the patient should be able to breath normally limiting the possibilities of using the HYPERcollar for treatment of sites higher in the head and neck region. The other sites at which adequate HT can be applied with the HYPERcollar remain to be determined. However, such research should be initiated by specific clinical demands.

Potential of HT for the larynx and hypopharynx region Treatment of advanced squamous cell carcinoma of the head and neck (HNSCC) still remains challenging. The currently standard radiochemotherapy treatment generally results in a 5-year survival rate of 20% to 65%[12], depending on the site, stage and treatment techniques used. The addition of chemotherapy to radiation is at the cost of major toxicity, i.e. approximately 80% of patients require a feeding tube during treatment[12]. Further, late toxicities related to radiation, such as loss of salivary function and soft tissue fibrosis, can lead to difficulties in speaking and eating[43]. These toxicities can be avoided by keeping the dose to the concerned tissues low[8,43]. There are two possible goals of adding HT to current treatment schedules, i.e. 1) increase of local tumour control by the addition of HT to current treatment modal-

ities or 2) decrease of toxicity due to the replacement of current modalities, or a part of them, by HT. Based on treatment planning results of ten H&N patients, we expect no elevation of the toxicity related to RT since the SAR levels predicted in the myelum are very low. Recently, a relationship between RT dose, received by the muscular components of the swallowing apparatus, and - dysphagia related - quality of life (QoL) was found for 81 patients with oropharyngeal cancer treated with IMRT / 3DCRT $\pm$ Chemotherapy[55]. A steep dose-effect relationship, with an increase of the probability of dysphagia of 19% with every additional 10 Gy, was established. The multivariate analysis shows a significant effect of dose. Experimental studies have shown that HT enhances RT by a factor between 1.2 and 5[98] and clinical studies in H&N cancer suggest a thermal enhancement ratio of 1.6[71]. An enhancement of RT toxicity to normal tissues generally is not observed. Therefore, one way to improve the QoL is to constrain the dose to be received by the swallowing muscles and supplement this dose reduction with HT.

Combining all possibilities, there is sufficient potential for the thorough exploration of the effect of adding HT to the currently available options for a multi-modality treatment of cancers in the head and neck region.

Summary

Treatment of advanced tumours in the head and neck (H&N) remains complex and the toxicity related to the currently standard treatment modalities remains a major issue. For many tumour sites, the addition of hyperthermia (HT) to radiotherapy has been shown to result in remarkably higher (complete) response rates, improved local control rates, better palliative effects and/or better overall survival rates. HT has a high potential to improve cancer treatment results in H&N patients as well while adding no toxicity. However, an appropriate applicator that can heat both superficially and deeply located target sites in the H&N region is currently not available.

This thesis describes the items that needed to be addressed to design and build such an applicator. Extensive theoretical parameters studies were performed 1) to show the feasibility of deep heating in the H&N using radiofrequency (RF) waves and 2) to guide the design of the applicator. These parameter studies were performed using electromagnetic (EM) simulation programs. These predictions were then verified by measurements and with their results we designed and build a clinical prototype. We performed treatment planning for several patients to establish the specific absorption rate (SAR) patterns that are achievable with this applicator. Lastly, the heating session of the first patient of the ongoing clinical feasibility study is evaluated.

After a general introduction in **Chapter 1**, the investigations into the ability to deposit RF-energy centrally in the neck are reported in **Chapter 2**. For this investigation we used a realistic model of the H&N anatomy, which is irradiated by a circumferential array of dipole antennas, and calculated the corresponding power absorption distributions. An optimal focussing ability of the set-ups, i.e. the ability to direct energy efficiently into the target region, was found for frequencies between 400 and 600 MHz. The optimum frequency is found to be highly dependent on the size of the target volume but relatively robust for different neck sizes. Finally it is found that this focussing ability at 433 MHz is enhanced significantly by increasing the number of antenna elements from four to six and eight, but this enhancement is limited for a further extension to sixteen antennas.

The objective of the work described in **_Chapter 3_** was to gain insight in the distortions on the local SAR distribution by various major anatomical structures in the neck. Calculations, based on a high resolution variable grid and a finite difference time domain (FDTD) algorithm, are conducted for a semi-3D generic phantom. This muscle-equivalent phantom was based on average dimensions obtained from CT-derived human data and simplified structures representing trachea, cartilage, spine and spinal cord. In addition, phantoms with dimensions equal to maximum and minimum values within the CT-derived data are also studied. By exposing these phantoms to a circular coherent array of eight dipoles, driven at 433 MHz using no phase delays, we found a centrally located region of high SAR within all neck phantoms. This focal region changes from a circular cross-section in the case of the muscle phantom to a donut shaped region when the anatomical structures are inserted. However, the location of the focus does not change. We conclude that the SAR obtained in homogeneous phantom measurements can be considered reasonable predictive for the SAR patterns in more complex geometries.

Chapter 4 describes the exploration of the options of a circular, multi-ring, array of antennas to deposit RF-energy centrally in the neck. We found that, for obtaining one single arrangement for all patients, an enlarged antenna ring radius is required, which leads to some decrease in efficiency of the set-up. By improving the orientation of the antenna array with respect to the patient we could reduce this effect. Increasing the number of antenna rings led to a better focussing of the power ($1 \rightarrow 2$ / $3 : \sim 17\%$). Increase of the distance between these antenna rings resulted in a smaller - more target region conformal - focus but also a decreased penetration of the waves to the center. From this study we selected an arrangement consisting of two rings of six antennas with a radius of 20cm and 6cm array spacing. This arrangement is considered a good choice providing the ability to heat the majority of patients.

The next step was the design of an antenna element to replace the dipole antennas of the parameter studies, which is described in **_Chapter 5_**. Hereto we used EM modelling for converging towards a resonant probe-fed patch antenna for the H&N applicator. The main advantage of this design, over the designs currently used in deep hyperthermia, is the direct feeding with a coaxial cable, i.e. no matching circuit is required. We presume that this direct feeding leads to easier and more accurate modelling, and also to greater robustness and higher efficiency. Further, the design is light and small ($\sim \lambda/3$). Theoretically, the electrical performance of the antenna was found to be satisfactory over a temperature range of 15-35°C, and stable for patient-antenna distances to as small as 4cm. As expected, the predictions further showed a very good match with the experimental verification measurements.

The purpose of the work described in ***Chapter 6*** was to experimentally verify the feasibility of focussed heating in the neck region by an array of two rings of six antennas as found in Chapter 4. SAR measurements were performed with a specially constructed laboratory prototype H&N applicator, including a neck mimicking cylindrical muscle phantom. Measurements were conducted by three different methods: i.e. electric-field Schottky-diode sheet measurements and, using the power-pulse technique, fiberoptic thermometry and infra-red (IR) thermography. Using phase-steering, we further showed that the antenna arrangement enables to adjust the SAR focus in radial (x/y) and axial (z) directions. A central 50% iso-SAR focus of 35 mm (±3 mm) in diameter and around 100 mm (±15 mm) in length were obtained using the laboratory prototype for all investigated settings. SAR distributions, as measured by all three experimental methods, are qualitatively well predicted by the simulations. For quality assurance (QA) measurements we conclude that the Schottky-diode sheet provides the best compromise between effort, speed and accuracy, though a more specific and improved design is warranted.

All previous investigations have resulted in the construction of the novel HYPERcollar applicator system for clinical treatments. By the work described in ***Chapter 7***, we aimed to show the features and potential of the applicator system for hyperthermia treatments in the H&N region. By infra-red (IR) thermography in a neck-equivalent cylindrical phantom, we measured that a central focus in the neck can be obtained, with 50% iso-SAR lengths of 35 mm in radial (x/y) directions and around 100 mm (±10 mm) in the axial direction (z). These dimensions are comparable to the focus obtained with the laboratory prototype. By comfort tests with five healthy volunteers we found that the applicator provides sufficient comfort to maintain in treatment position for an hour, which is the standard hyperthermia treatment duration in our center. Patient-specific treatment planning showed that the applicator provides sufficient degrees of freedom to enable encompassing simultaneously both a deep-seated primary laryngeal tumour and a superficial lymph node metastasis, at the 25% iso-SAR level. Therefore we conclude that heating of such a large and irregularly-shaped target region is feasible.

In ***Chapter 8*** we report on the first heating session of the phase I study. In this study we investigate the feasibility of deep heating in the H&N with the HYPERcollar. The first session was applied to an 82 year-old male patient with a squamous cell carcinoma of the larynx ($T_3N_0M_0$: a primary tumour without lymph node or distant metastasis). According to the phase I study protocol, the most important aim was to achieve temperatures above 39°C at all measurement points in the gross tumour volume. We found that tumour selective heating was obtained, i.e. we measured temperatures between 39.6 and 40.6°C at tumour indicative locations and lower temperatures at myelum indicative locations. Further, the level of comfort was sufficient for this patient to endure the full treatment hour. By treatment planning we could further show that the tumour volume was well covered by the 25% iso-SAR

contour and we found no evidence of hyperthermia related toxicity. Therefore, we concluded that all goals of the phase I study are met.

Samenvatting

De behandeling van gevorderde (grote) tumoren in het hoofd-hals (HH) gebied blijft lastig en de toxiciteit (bijwerkingen) bij de huidige standaardbehandelingen is nog steeds een belangrijk item. Voor veel tumor locaties is aangetoond dat de toevoeging van hyperthermie (HT) aan radiotherapie leidt tot opmerkelijk betere (complete) responses, verbeterde lokale controle, betere palliatieve effecten en/of betere overlevings cijfers. Er is een grote kans dat hyperthermie (HT) ook kan bijdragen aan een goede behandeling van kanker in het HH gebied. Voor het HH gebied echter bestaat er nog geen apparaat dat zowel oppervlakkige als diep-gelegen tumoren kan verwarmen.

Dit proefschrift beschrijft alles wat nodig was om te komen tot een dergelijk HH HT applicator. Uitgebreide theoretische parameter studies, met behulp van electro-magnetische (EM) simulatie paketten, zijn uitgevoerd om 1) de mogelijkheid aan te tonen om diep te verwarmen in het HH gebied met radiofrequente (RF) golven en 2) om de keuzes voor het ontwerp te onderbouwen. De simulaties zijn geverifieerd met metingen en daarna gebruikt om het klinische protoype te ontwerpen en bouwen. Met behulp van behandelplanningen voor meerdere patiënten zijn verder de mogelijke "specific absorption rate" (SAR) verdelingen vastgesteld voor deze applicator. Tot slot, is in de eerste patiënt van een fase I (haalbaarheids) studie de mogelijkheid om diep te verwarmen aangetoond.

Na een algemene introductie in **Hoofdstuk 1**, wordt het onderzoek naar de mogelijkheid om centraal in de hals te verwarmen beschreven in **Hoofdstuk 2**. Voor dit onderzoek is een realistisch model van de HH anatomie gebruikt, die door een circumferentiele array (reeks) van dipool antennes wordt bestraald, en zijn de bijbehorende vermogensabsorptie distributies berekend. Het doel was hierbij om de opstelling te vinden waarmee de energie het beste kan worden gefocusseerd, d.w.z. dat de energie efficiënt naar het doelgebied wordt geleid. De frequentie die leidt tot een optimale focussering ligt tussen 400 en 600 MHz. De exacte optimale frequentie is erg afhankelijk van de grootte van het doelvolume maar relatief robuust voor

andere hals diameters. Tot slot wordt de focussering van de energie verbeterd door het aantal antenne elementen te verhogen van vier naar zes of acht. Het voordeel van een verdere uitbreiding tot zestien antennes is echter beperkt.

De doelstelling van het werk dat in **Hoofdstuk 3** wordt beschreven is inzicht te krijgen in de vervormingen van de lokale SAR distributie door diverse belangrijke anatomische structuren in de hals. De berekeningen zijn uitgevoerd met een finite difference time domain (FDTD) gebaseerd programma, met een variabel grid en een hoge resolutie, voor een semi-3D generiek fantoom. Dit spier-equivalent fantoom was gebaseerd op gemiddelde afmetingen uit CT scans van HH patiënten en bestond uit vereenvoudigde structuren die trachea, kraakbeen, ruggemerg en ruggewervel vertegenwoordigden. Bovendien werden fantomen met afmetingen gelijk aan maximum en minimumwaarden bestudeerd. Door deze fantomen aan een circulaire coherente array van acht dipolen bloot te stellen, die golven van 433 MHz met gelijke fases uitzenden, werd een centraal gebied met hoge SAR waarden gevonden voor alle halsfantomen. Dit focus gebied verandert van een cirkelvorm in een donutvorm wanneer de anatomische structuren in het fantoom worden geplaatst. De positie van het focusgebied verandert echter niet, dus homogene fantoom metingen kunnen voorspelbaar worden geacht voor de meer complexe geometrieën.

Hoofdstuk 4 beschrijft het onderzoek naar de opties die een circumferentieel, multiring, array van antennes biedt om RF-energie centraal in de hals te focusseren. Voor het verkrijgen van één enkele opstelling voor alle patiënten is een vergrote straal van de antenne-ring vereist, welke tot een kleine daling van efficiëntie van de opstelling leidt. Door de orientatie van de antenne array, met betrekking tot de patiënt, te veranderen kan deze daling in efficiëntie verminderd worden. Het verhogen van het aantal antenneringen leidt tot een betere focussering van het vermogen ($1 \rightarrow 2 / 3 : \sim 17\%$). De vergroting van de afstand tussen deze antenneringen resulteert in een kleiner - meer doelgebied conform - focusgebied, maar ook een verminderde penetratie van de golven naar het centrum. Als gevolg van deze studie is een opstelling geselecteerd bestaande uit twee ringen van zes antennes, met een straal van 20cm en 6cm afstand tussen de twee antenne ringen. Deze opstelling biedt waarschijnlijk de mogelijkheid om de meerderheid van de tumoren te verwarmen.

De volgende stap was het ontwerp van een antenne element die de dipool antennes van de parameterstudies kon vervangen, wat wordt beschreven in **Hoofdstuk 5**. Hiervoor is EM modellering gebruikt om een resonante "patch" antenne voor de HH applicator te vinden. Het belangrijkste voordeel van dit ontwerp, vergeleken met de ontwerpen die momenteel in diepe HT worden gebruikt, is de directe voeding met een coaxiale kabel, d.w.z. er is geen aanpassingscircuit vereist. Waarschijnlijk leidt deze directe aansluiting aan de coax kabel tot een gemakkelijkere en nauwkeurigere modellering, en verder tot grotere robuustheid en hogere efficiëntie. Theoretisch, waren de elektrische eigenschappen van de antenne geschikt voor temperaturen tussen 15 en

35°C, en stabiel voor patiënt-antenne afstanden vanaf 4 cm. Zoals verwacht, toonden de voorspellingen een zeer goede gelijkenis met de experimentele controlemetingen.

Het doel van het werk dat in **Hoofdstuk 6** wordt beschreven, was het experimenteel verifiëren van de haalbaarheid van het gefocusseerd verwarmen in het halsgebied door een serie van twee ringen van zes antennes, zoals gevonden in Hoofdstuk 4. SAR metingen werden uitgevoerd met een speciaal geconstrueerd laboratorium prototype van de HH applicator, inclusief een cilindervormig spier equivalent fantoom van de hals. De metingen werden uitgevoerd met gebruik van drie verschillende meetmethodes: elektrische veld Schottky-diode sheet metingen en, gebruik makend van de "power-pulse" techniek, fiberoptische thermometrie en infrarode thermografie (IR). Door middel van fase-sturing, werd aangetoond dat het met de antenne-opstelling mogelijk is om het SAR focus in radiale (x/y) richtingen en in de richting van de patiënt-as (z) aan te passen. Een centraal 50% iso-SAR focus van 35 mm ($\pm$3 mm) diameter en ongeveer 100 mm ($\pm$15 mm) lengte werd gevonden in het laboratorium prototype voor alle onderzochte instellingen. De SAR distributies, zoals die met alle drie de experimentele methodes zijn gemeten, werden kwalitatief goed voorspeld door de simulaties. Vanuit deze metingen werd geconcludeerd dat het Schottky-diode sheet voor quality assurance (QA) metingen het beste compromis vormt tussen moeite, snelheid en nauwkeurigheid. Echter, een aangepast ontwerp van het sheet zou hiervoor nog moeten worden ontwikkeld.

Al het voorgaande onderzoek heeft geresulteerd in de bouw van het nieuwe HYPER-collar applicator systeem voor klinische behandelingen. In **Hoofdstuk 7** worden de mogelijkheden en potentie van het applicator systeem voor HT behandelingen in het HH gebied beschreven. Door middel van infrarode (IR) thermografie in een spier-equivalent cilindrisch fantoom, werd vastgesteld dat een centraal SAR focus in de hals kan worden verkregen, met 50% iso-SAR lengtes van 35 mm in de radiale richtingen (x/y) en ongeveer 100 mm ($\pm$10 mm) in de richting van de patiënt-as (z). Deze afmetingen zijn vergelijkbaar met het SAR focus dat met het laboratorium prototype werd verkregen. Comfort tests, bij vijf gezonde vrijwilligers, toonden aan dat de applicator voldoende comfort biedt aan de patiënt om een uur in behandelingspositie te blijven: de standaard duur van een HT behandeling in de Daniel den Hoed kliniek. De patiënt-specifieke behandelingsplanning geeft aan dat de applicator voldoende vrijheidsgraden biedt voor het simultaan omvatten, op het 25% iso-SAR niveau, van zowel een diepgelegen primaire larynx tumor als een oppervlakkige lymfeklier metastase. Daarom concluderen wij dat verwarmen van een dergelijk groot, en onregelmatig gevormd, doelgebied uitvoerbaar is met de HYPERcollar.

In **Hoofdstuk 8** wordt de eerste verwarmings sessie van de eerste patiënt in de fase I (haalbaarheids) studie beschreven. In deze studie onderzoeken wij de mogelijkheid om tumoren in het HH gebied met de HYPERcollar te verwarmen. Deze eerste sessie werd toegepast op een 82-jarige mannelijke patiënt met een squamous celcarcinoom

in het strottehoofd ($T_3N_0M_0$: een primaire tumor zonder lymfeklier of afstand metastase). In het fase I studieprotocol, is het belangrijkste doel om temperaturen boven 39°C te bereiken op alle meetpunten in het tumor volume. Tijdens de sessie vonden wij dat de tumor selectief verwarmd kan worden: temperaturen tussen 39.6 en 40.6°C werden gemeten bij alle tumor-indicatieve meetpunten en lagere temperaturen bij myelum-indicatieve meetpunten. Verder, vonden wij dat het niveau van comfort voor deze patiënt volstond om de volledige behandelingsduur van één uur te volbrengen. Door middel van behandelingsplanning werd verder aangetoond dat het tumorvolume voldoende door de 25% iso-SAR contour werd omvat en wij vonden geen aanwijzingen van HT-toxiciteit. Concluderend betekent voorgaande dat, hoewel er problemen waren, alle doelstellingen van de fase I studie zijn behaald voor deze patiënt.

List of publications

International journal publications

M.M. Paulides, S.H.J.A. Vossen, A.P.M. Zwamborn and G.C. Van Rhoon, "Theoretical investigation into the feasibility to deposit RF energy centrally in the head and neck region," *Int. J. Rad. Onc. Biol. Phys.*, vol. 63, p. 634-642, 2005.

M.M. Paulides, D.H.M. Wielheesen, J. Van der Zee and G.C. Van Rhoon, "Assessment of the local SAR distortion by major anatomical structures in a cylindrical neck phantom," *Int. J. Hyperthermia*, vol. 21, p. 125-140, 2005.

M.M. Paulides, J.F. Bakker, A.P.M. Zwamborn and G.C. Van Rhoon, "A head and neck hyperthermia applicator: theoretical antenna array design," *Int. J. Hyperthermia*, vol. 23, p. 59-67, 2007.

M.M. Paulides, J.F. Bakker, N. Chavannes and G.C. Van Rhoon, "A patch antenna design for a phased-array head and neck hyperthermia applicator," *IEEE Trans. Biom. Eng.*, In press.

M.M. Paulides, J.F. Bakker and G.C. Van Rhoon, "A head and neck hyperthermia applicator: experimental phantom verification and FDTD model," *Int. J. Rad. Onc. Biol. Phys.*, vol. 68, p. 612-620, 2007.

M.M. Paulides, J.F. Bakker, E. Neufeld, J. van der Zee, P.P. Jansen, P.C. Levendag and G.C. van Rhoon. "The HYPERcollar: a novel applicator for hyperthermia in the head and neck," *Int. J. Hyperthermia.*, (accepted).

E. Neufeld, M. Paulides, T. Samaras, N. Chavannes, G. van Rhoon, G. Szekely and N. Kuster. "Requirements, techniques and implementations for routine high resolution hyperthermia treatment planning in clinical applications," *Int. J. Hyperthermia.*, (submitted).

Publications at conferences

M.M. Paulides, S.H.J.A. Vossen, B.J.A.M. van Leersum, A.P.M. Zwamborn, J. Van der Zee and G.C. van Rhoon, "Hyperthermia treatment of head and neck tumours: an initial exploration", 21st Annual meeting of the European Society for Hyperthermic Oncology, 2003, Munchen, Germany.

M.M. Paulides, D.H.M. Wielheesen, M. de Bruijne, W.M. Lee, J. van der Zee and G.C. van Rhoon, "Heating the head and neck: SAR distortions by major anatomy structures", 9th International Congress on Hyperthermic Oncology, 2004, St. Louis, USA.

N. Siauve, L. Nicolas, C. Vollaire, N. Burais and M.M. Paulides, "Development of a treatment planning tool for hyperthermia treatment of cancerous tumours with electromagnetic fields", 3rd international workshop on biological effects of electromagnetic fields, 2004, Kipriotis Village Resort, Kos, Greece.

G.C. Van Rhoon, M. de Bruijne, M.M. Paulides, J. van der Zee and A.P.M. Zwamborn, "Improvement of the clinical application of superficial hyperthermia during the last two decades." *Radiother. & Oncol.* vol. 73, p. 251, 2004.

M.M. Paulides, S.H.J.A. Vossen, A.P.M. Zwamborn and G.C. van Rhoon, "Theoretical investigation into the feasibility to deposit RF energy centrally in the head and neck region", 22nd Annual meeting of the European Society for Hyperthermic Oncology, 2005, Graz, Austria.

N. Siauve, M.M. Paulides, L. Nicolas, B.J.A.M. van Leersum, G.C. van Rhoon, C. Vollaire and A. Nicolas, "Comparison of FDTD and FE Methods in Numerical Dosimetry for the Treatment of Cancerous Tumours with Electromagnetic Fields", The 15th Conference on the Computation of Electromagnetic Fields, Shenyang, 2005, Liaoning, China.

J.F. Bakker, M.M. Paulides, G.C. van Rhoon, H. Schippers and T.A. Ter Meer, "Development of a gain & phase detector for a hyperthermia applicator", Proceedings of joint 9th International Conference on Electromagnetics in Advanced Applications ICEAA '05 and 11th European Electromagnetic Structures Conference EESC '05, ISBN 88-8202-094-0, p. 209-212, 2005, Torino, Italy.

M.M. Paulides, J.F. Bakker and G.C. van Rhoon, "A patch antenna design for a phased-array applicator for hyperthermia treatment of head and neck tumours", Proceedings of the 3rd European Medical & Biological Conference, IFMBE European Conference on Biomedical Engineering (EMBEC), ISSN: 1727-1983, 2005, Prague, Czech Republic.

M.M. Paulides, J.F. Bakker and G.C. van Rhoon, "A head and neck hyperthermia applicator: theoretical antenna array design", 23nd Annual meeting of the European Society for Hyperthermic Oncology, 2006, Berlin, Germany.

V. Bhandari, M.M. Paulides, J. Van Der Zee and G.C. van Rhoon, "Development of hyperthermia treatment planning for head and neck malignancies", 28th Annual meeting of the International Clinical Hyperthermia Society (ICHS), 2007, Mumbai, India.

M.M. Paulides, J.F. Bakker, P.P. Jansen, P.C. Levendag, J. van der Zee and G.C. van Rhoon, "Innovations in technology to targeted heating in head and neck hyperthermia", 28th Annual meeting of the International Clinical Hyperthermia Society (ICHS), 2007, Mumbai, India.

M.M. Paulides, J.F. Bakker, P.P. Jansen, P.C. Levendag, J. van der Zee and GC van Rhoon, "A novel head and neck applicator for targeted hyperthermia", International meeting on innovative approaches in head and neck oncology (EHNS - ESTRO), 2007, Barcelona, Spain.

M.M. Paulides, J.F. Bakker and G.C. van Rhoon, "A patch antenna design for a head and neck hyperthermia applicator", The 23rd International Review of Progress in Applied Computational Electromagnetics (ACES), 2007, Verona, Italy.

M.M. Paulides, J.F. Bakker, P.P. Jansen, P.C. Levendag, J. van der Zee and GC van Rhoon, "The HYPERcollar: a novel head and neck applicator for targeted hyperthermia", 8th International meeting on progress in radio-oncology ICRO / OGRO, 2007, Salzburg, Austria.

J. van der Zee, M. de Bruijne, M.M. Paulides, M. Franckena, R. Canters and G.C. van Rhoon, "The use of hyperthermia treatment planning in clinical practice", 8th International meeting on progress in radio-oncology ICRO / OGRO, 2007, Salzburg, Austria.

M.M. Paulides, J.F. Bakker, P.P. Jansen, P.C. Levendag, J. van der Zee and G.C. van Rhoon, "Innovations in technology to target heating in head and neck hyperthermia", World Conference on Interventional Oncology and Society of Thermal Medicine, May 14-17, 2007, Washington DC, USA.

M.M. Paulides, J.F. Bakker, E. Neufeld, P.P. Jansen, P.C. Levendag, J. van der Zee and GC van Rhoon, "The HYPERcollar: a novel phased-array applicator for hyperthermia treatment in the neck", 24th Annual meeting of the European Society for Hyperthermic Oncology (ESHO), 2007, Prague, Czech Republic.

M.M. Paulides, J.F. Bakker, N. Chavannes and G.C. van Rhoon, "A patch antenna element for the HYPERcollar applicator: design and characterization", 24th Annual meeting of the European Society for Hyperthermic Oncology (ESHO), 2007, Prague, Czech Republic.

J.F. Bakker, M.M. Paulides and G.C. van Rhoon, "A phased array head and neck applicator: measurements of the SAR distributions in a cylindrical muscle phantom", 24th Annual meeting of the European Society for Hyperthermic Oncology (ESHO), 2007, Prague, Czech Republic.

Honors

Young Investigator Travel Award of the 9th International Congress on Hyperthermic Oncology (ICHO), 2004, St. Louis, USA.

ESHO-student Award of the 23rd Annual Meeting of the European Society for Hyperthermic Oncology (ESHO), 2006, Berlin, Germany.

Kim Award of the 24th Annual Meeting of the European Society for Hyperthermic Oncology (ESHO), 2007, Czech Republic.

Curriculum Vitae

Margarethus Marius Paulides was born in the Netherlands in 1979. After graduating highschool (HAVO) he started his study electrical engineering at the Hogeschool 's Hertogenbosch. After receiving his first year "Propadeuse" diploma he continued studying electrical engineering at Eindhoven University of Technology (EUT) where he received his M.Sc. degree in 2002. For this study he worked on a calibration procedure for an active-microwave imaging scanner at l'Ecole Supérieure d'Electricité (Supélec) situated near Paris (France). His graduation project was carried out at TNO-FEL, The Hague and was in association with the Hyperthermia Unit of the Erasmus MC. From 2003, he worked as AIO/Promovendus/OIO towards his PhD degree at the Hyperthermia Unit, Department of Radiotherapy, Erasmus MC - Daniel den Hoed Cancer Center, Rotterdam, the Netherlands. His work was within a Dutch Cancer Society project entitled: "Development, construction and clinical testing of a novel electromagnetic applicator for hyperthermia treatment of advanced head and neck carcinoma". His research interests are in the area of hyperthermia treatment planning, bioelectromagnetics, antenna design and applied clinical physics.

Dankwoord / Acknowledgements

Aan het einde van mijn promotie traject is de tijd gekomen om terug te kijken op wat geweest is maar zeker nog niet vergeten. Een promotie lijkt in vele opzichten op een moeilijke wedstrijd. Maar deze hoeft gelukkig niet alleen te worden gestreden. Er zijn vele mensen geweest die op hun eigen wijze een bijdrage geleverd hebben aan het tot stand komen van dit proefschrift. Al deze mensen ben ik veel dank verschuldigd en een aantal mensen daarvan wil ik in het bijzonder eruit lichten.

Hoe kun je een wedstrijd winnen zonder de goede materialen? Hiervoor zorgden de leden van de instrumentmakerij, en in het bijzonder Bert. De sfeer bij jullie is altijd goed en relaxed en verder sta ik nog steeds versteld van het vakwerk dat jullie afleveren bij de constructie van de HYPERcollar.

Further, I would like to express my sincere gratitude to Esra who was always willing to implement new features in SEMCAD at my demand. Also, I would like to thank all people of Speag and the IT'IS Foundation (Zurich, Switzerland) for their continuous help in many ways.

Het Nationaal Lucht- en Ruimtevaartlaboratorium (NLR) en de afdeling klinische instrumentatie van het UMC Utrecht wil ik bedanken voor hun bijdrage aan het versterkersysteem en de goede samenwerking.

Verder wil ik ook Anton Tijhuis en iedereen van de Technische Universiteit Eindhoven bedanken voor de inwijding in de elektrotechniek, specifiek de elektromagnetisme, en de hulp tijdens mijn promotie traject.

Een zware strijd kan niet worden gestreden vanuit een goede basis. De unit hyperthermie vormt deze basis door het verzorgen van de gezelligheid tussen het werk door. De koffietafel is de plaats waar lief en leed kunnen worden gedeeld en zelfs de meest baanbrekende ontdekkingen kunnen worden gerelativeerd. De boeiende mix van laboranten, artsen, technici en fysici zorgt voor een kakelbont geheel waar aan gezichtspunten geen gebrek is. Verder is hier ook het forum waar de ideeën uit de kliniek en de wetenschap samen kunnen worden gevoegd. Specifiek wil ik hier de leden van het hoofd-hals behandel team benoemen: Cobi en Laurens, voor al hun inspanningen voor het klinische deel van de hoofd-hals behandeling. Verder wil ik

Cobi danken voor alles wat je me geleerd hebt met betrekking tot alle klinische aspecten van een hyperthermie behandeling.

Alle mensen van mijn tweede basis tijdens het project, TNO te Den Haag, wil ik bedanken voor de interessante discussies en al jullie bijdragen. Hierbij wil ik specifiek Stefan en Chris noemen van wie ik heb geleerd dat wetenschap, naast inhoudelijk werk, toch ook mensenwerk is. Hans Strijbos wil ik specifiek noemen voor zijn hulp in het ontwerp van de "patch" antenne. Verder dacht je altijd mee zodat in een vroeg stadium de potentiële problemen konden worden voorzien.
Speciaal wil ik ook Peter Zwamborn bedanken voor je immer persoonlijke begeleiding als afstudeer-hoogleraar en promotor. Altijd wilde je tijd vrijmaken voor een hoogst nodig gesprek of "zo maar even bijpraten".

Peter Levendag wil ik bedanken voor je werk als mijn promotor en het vertrouwen dat je op cruciale momenten uitsprak in mij en het hoofd-hals project.

Een van de belangrijkste schakels binnen het project en mijn promotie was Gerard, de "niet-zo-stille" motor achter het project. Je tomeloze enthousiasme werkt echt aanstekelijk en aan ideeën is er nooit gebrek. Het "out-of-the-box" denken heb je tot een kunst verheven, net als het creatief inzetten van de financieën. Verder ben je ook altijd bezig om iedereen zichzelf te laten ontplooien en verlies je de menselijke kant van het verhaal nooit uit het oog. Gerard, ook zonder jou zou dit alles nooit voor elkaar gekomen zijn.

Projectwerk is teamwerk en het project had dus nooit kunnen slagen zonder de inzet van Jurriaan. Het is best bijzonder om een collega te vinden die zo ongeveer alle zwakke kanten die je hebt kan compenseren. Onze combinatie zorgde voor een groot synergistisch effect en dus een grote JER (Jurriaan Enhancement Ratio). Jur, ook jou wil ik hartelijk danken.

Het strijdperk van de wetenschap kan niet goed worden betreden zonder een goede voorbereiding. In dit verband wil ik vooral mijn ouders bedanken die altijd achter me gestaan hebben en zijn ingesprongen waar dat nodig was. Misschien was echter het belangrijkste nog wel dat jullie me een groot doorzettingsvermogen hebben meegegeven, door zelf hierin voor te gaan. Voor alle bemoeienissen en positieve kritiek: hartelijk dank.

Als laatste wil ik mijn liefste bedanken. Zij weet mij altijd met mijn voeten op de grond en mijn hoofd in de wolken te houden.

Bibliography

1. *Sigma eye applicator operator manual.* BSD Medical Corporation, 1995.

2. M Amichetti, M Romano, L Busana, A Bolner, G Fellin, G Pani, L Tomio, and R Valdagni. Hyperfractionated radiation in combination with local hyperthermia in the treatment of advanced squamous cell carcinoma of the head and neck: a phase I-II study. *Radiother Oncol*, 45:155–158, 1997.

3. Ansoft Designer. Ansoft Coorporation (http://www.ansoft.com).

4. JF Bakker, MM Paulides, GC Van Rhoon, H Schippers, and TA Ter Meer. Development of a gain & phase detector for a hyperthermia applicator. In *Proceedings of the joint 9th International Conference on Electromagnetics in Advanced Applications (ICEAA '05) and 11th European Electromagnetic Structures Conference (EESC '05)*, pages 209–212, Torino, Italy, 2005. ISBN 88-8202-094-0.

5. CA Balanis. *Antenna theory: Analysis and design.* John Wiley & Sons, Inc., New York, 2nd edition edition, 1997.

6. R Ben-Yosef and DS Kapp. Direct clinical comparison of ultrasound and radiative electromagnetic hyperthermia in the same tumours. *Int J Hyperthermia*, 11:1–10, 1995.

7. J Bernier, J Denekamp, A Rojas, E Minatel, J Horiot, H Hamers, P Antognoni, O Dahl, P Richaud, M Van Glabbeke, and M Pi. ARCON: Accelerated Radiotherapy with Carbogen and Nicotinamide in head and neck squamous cell carcinomas. the experience of the cooperative group of radiotherapy of the european organization for research and treatment of cancer (EORTC). *Radiother Oncol*, 55:111–119, 2000.

8. PM Braam. *Parotid gland sparing radiotherapy.* PhD thesis, Utrecht University, 2007.

9. CHM Clemens, SHJA Vossen, AB Woltering, and APM Zwamborn. Study of the possible effects on health of the use of portable terminals within the C2000 radio network. TNO-FEL internal report: FEL-02-C152, Reproduction Department of The Netherlands Organisation of Applied Scientific Research (TNO), 2003.

10. R Colombo, LF Da Pozzo, A Salonia, P Rigatti, Z Leib, J Baniel, E Caldarera, and M Pavone-Macaluso. Multicentric study comparing intravesical chemotherapy alone and with local microwave hyperthermia for prophylaxis of recurrence of superficial transitional cell carcinoma. *J Clin Oncol*, 21:4270–4276, 2003.

11. ESHO Taskgroup Committee. *Treatment planning and modelling in hyperthermia, a task group report of the European Society for Hyperthermic Oncology.* Tor Vergata, Rome, Italy, 1992.

12. BA Conley. Treatment of advanced head and neck cancer: what lessons have we learned? *J Clin Oncol*, 24:1023–1024, 2006. Editorial.

13. J Crezee, HP Kok, J Wiersma, G Van Stam, J Sijbrands, A Bel, and PMA Van Haaren. Improving locoregional hyperthermia equipment using 3D power control: from AMC-4 to AMC-8. In *Abstracts of the 22nd Annual Meeting of the ESHO, Graz, Austria (ESHO-05)*, pages 14–15, June 2005.

14. O Dahl, R Dalene, BC Schem, and O Mella. Status of clinical hyperthermia. *Acta Oncol*, 38:863–873, 1999.

15. M De Bruijne, T Samaras, E Neufeld, and GC Van Rhoon. Effectiveness of FDTD in Predicting SAR Distributions from the Lucite Cone Applicator. In *Abstracts of the 22nd Annual Meeting of the ESHO, Graz, Austria (ESHO-05)*, June 2005.

16. M De Bruijne, T Samaras, JF Bakker, and GC Van Rhoon. Effects of waterbolus size, shape and configuration on the SAR distribution pattern of the Lucite cone applicator. *Int J Hyperthermia*, 22:15–28, 2006.

17. MW Dewhirst, L Pronnitz, D Thrall, D Prescott, S Clegg, C Charles, J MacFall, G Rosner, T Samulski, E Gillette, and S LaRue. Hyperthermia treatment of malignant diseases: Current status and a view towards the future. *Semin Oncol*, 24:616–625, 1997.

18. MW Dewhirst, Z Vujaskovic, E Jones, and D Thrall. Re-setting the biological rationale for thermal therapy. *Int J Hyperthermia*, 21:779–790, 2005.

19. S Dische, M Saunders, A Barrett, A Harvey, D Gibson, and M Parmar. A randomised multicentre trial of CHART versus conventional radiotherapy in head and neck cancer. *Radiother Oncol*, 37:123–126, 1997.

20. S El-Sayed and N Nelson. Adjuvant and adjunctive chemotherapy in the management of squamous cell carcinoma of the head and neck region: A meta-analysis of prospective and randomized trials. *J Clin Oncol*, 14:838–847, 1996.

21. SB Field and C Franconi. *Physics and Technology of Hyperthermia.* Martinus Nijhoff Publishers, P.O. box 163, 330 AD Dordrecht, 1987. ISBN 90-247-3509-2. Chapter I-7.

22. SB Field and JW Hand. *An introduction to the practical aspects of clinical hyperthermia.* Taylor & Francis Ltd., 4 John st., London WC1N2ET, 1990.

23. CM Furse, DH Roper, DN Buechler, DA Christensen, and CH Durney. The Problem and Treatment of DC Offsets in FDTD Simulations. *IEEE Trans Ant Prop*, 48(8):1198–1201, 2000.

24. C Gabriel, S Gabriel, and E Corthout. The dielectric properties of biological tissues I: Literature survey. *Phys Med Biol*, 41:2231–2249, 1996.

25. S Gabriel, RW Lau, and C Gabriel. The dielectric properties of biological tissues II: Measurements in the frequency range 10 Hz to 20 GHz. *Phys Med Biol*, 41:2251–2269, 1996.

26. S Gabriel, RW Lau, and C Gabriel. The dielectric properties of biological tissues III: Parametric models for the dielectric spectrum of tissues. *Phys Med Biol*, 41:2271–2293, 1996.

27. R Garg, P Bhartia, I Bahl, and A Ittipiboon. *Microstrip antenna design handbook.* Artech House, 685 Canton Street, Norwood, MA 02062, 2001. ISBN 0-89006-513-6.

28. EA Gelvich, VN Mazokhin, and II Throshin. An attempt at quantitative specification of SAR distribution homogeneity. *Int J Hyperthermia*, 12:431–436, 1996.

29. EJ Gross, TC Ceetas, PR Stauffer, RL Liu, and ML Lumori. Experimental assessment of phased-array heating of neck tumours. *Int J Hyperthermia*, 6:454–474, 1990.

30. AW Guy, CK Chou, and KH Luk. 915-MHz phased-array system for treating tumours in cylindrical structures. *IEEE Trans Micr Theor Tech*, 34:502–507, 1986.

31. JW Hand and JR James. *Physical Techniques in Clinical Hyperthermia.* Research Studies Press LTD. 58B Station Road, Letchworth, Herts. SG6 3BE, England, 1986. ISBN 0-86380-037-8. Chapter 4.

32. JW Hand, JJW Lagendijk, Bach Andersen J, and JC Bolomey. Quality assurance guidelines for ESHO protocols. *Int J Hyperthermia*, 5:421–428, 1989.

33. J Haveman, J Van der Zee, J Wondergem, JF Hoogeveen, and MC Hulshof. Effects of hyperthermia on the peripheral nervous system: a review. *Int J Hyperthermia*, 20:371–392, 2004.

34. J Haveman, P Sminia, J Wondergem, J Van der Zee, and MC Hulshof. Effects of hyperthermia on the central nervous system: What was learned from animal studies? *Int J Hyperthermia*, 21:473–487, 2005.

35. FM Henke, WT Joines, and TV Samulski. Variations of focal regions versus number and positions of sources in two-dimensional media. *Int J Hyperthermia*, 17:382–400, 2001.

36. TW Hertel and GS Smith. On the convergence of common FDTD feed models for antennas. *IEEE Trans Ant Prop*, 51:1771–1779, 2003.

37. J-C Horiot, P Bontemps, W Van den Bogaert, R Le Fur, D Van den Weijngaert, M Bolla, J Bernier, A Lusinchi, M Stuschke, J Lopez-Torrecilla, AC Begg, M Pierart, and L Collette. Accelerated fractionation compared to conventional fractionation improves loco-regional control in radiotherapy of advanced head and neck cancers: Results of the EORTC 22851 randomized trial. *Radiother Oncol*, 44:111–121, 1997.

38. SN Hornsleth. *Radiofrequency regional hyperthermia*. PhD thesis, Aalborg University, Denmark, 1996.

39. NG Huilgol. A phase I study to study arsenic trioxide with radiation and hyperthermia in advanced head and neck cancer. *Int J Hyperthermia*, 22:391–397, 2006.

40. K Ito, K Furuya, Y Okano, and L Hamada. Development and Characteristics of a Biological Tissue-Equivalent Phantom for Microwaves. *Electronics and Communications in Japan*, 84:67–77, 2001.

41. S Jacobsen and F Melandsø. The concept of using multifrequency energy transmission to reduce hot-spots during deep-body hyperthermia. *Ann Biom Eng*, 30:1–10, 2002.

42. WT Joines, Y Zhang, C Li C, and RL Jirtle. The measured electrical properties of normal and malignant human tissues from 50 to 900 mhz. *Med Phys*, 21:547–550, 1994.

43. AS Jones, DE Phillips, and FJM Hilgers. *Diseases of head, neck, nose and throat*. Hodder Headline Group, 1998. ISBN 0-340-64610-1. Chapter 12: "radiotherapy in head and neck oncology".

44. E Jones, D Thrall, MW Dewhirst, and Z Vujaskovic. Prospective thermal dosimetry: the key to hyperthermia's future. *Int J Hyperthermia*, 22:247–253, 2006.

45. F Jouvie, JC Bolomey, and G Gaboriaud. Discussion of the capabilities of microwave phased arrays for hyperthermia treatment of neck tumours. *IEEE Trans Micr Theor Tech*, 34:495–501, 1986.

46. RSJP Kaatee and GC Van Rhoon. An electric field measurement system, using a two-dimensional array of diodes. *Int J Hyperthermia*, 15:441–454, 1999.

47. HH Kampinga. Cell biological effects of hyperthermia alone or combined with radiation or drugs: A short introduction to newcomers in the field. *Int J Hyperthermia*, 22:191196, 2006.

48. RWP King, BS Trembley, and JW Strohbein. The electromagnetic field of an insulated antenna in a conducting or dielectric medium. *IEEE Trans Micr Theor Tech*, 31:574–583, 1983.

49. T Kohler, P Maass, P Wust, and M Seebass. A fast algorithm to find optimal controls of multiantenna applicators in regional hyperthermia. *Phys Med Biol*, 46:2503–2514, 2001.

50. H Kroeze, JB Van de Kamer, AAC De Leeuw, and JJW Lagendijk. Regional hyperthermia applicator design using FDTD modelling. *Phys Med Biol*, 46: 1919–1935, 2001.

51. JJW Lagendijk. Hyperthermia treatment planning. *Phys Med Biol*, 45:61–76, 2000.

52. JJW Lagendijk, GC Van Rhoon, SN Hornsleth, P Wust, AC De Leeuw, CJ Schneider, JD Van Dijk, J Van Der Zee, R Van Heek-Romanowski, SA Rahman, and C Gromoll. Esho quality assurance guidelines for regional hyperthermia. *Int J Hyperthermia*, 14:125–133, 1998.

53. J Lang, B Erdmann, and M Seebass. Impact of nonlinear heat transfer on temperature control in regional hyperthermia. *IEEE Trans Biomed Eng*, 46: 11291138, 1999.

54. HK Lee, AG Antell, CA Perez, WL Straube, G Ramachandran, RJ Myerson, B Emami, EP Molmenti, A Buckner, and MA Lockett. Superficial hyperthermia and irradiation for recurrent breast carcinoma of the chest wall: prognostic factors in 196 tumours. *Int J Rad Oncol Biol Phys*, 40:365–375, 1998.

55. PC Levendag. Dysphagia disorders in patients with cancer of the oropharynx are significantly affected by the radiation therapy dose to the superior and middle constrictor muscle: a dose-effect relationship. *Radiother Oncol*, 2007.

56. RL Magin and AF Peterson. Noninvasive microwave phased arrays for local hyperthermia: a review. *Int J Hyperthermia*, 5:429–450, 1989.

57. VA Marcial and TF Pajak. Radiation therapy alone or in combination with surgery in head and neck cancer. *Cancer*, 55:2259–2265, 1989.

58. CD Mathers, C Boschi-Pinto, AD Lopez, and CJL Murray. Cancer Incidence, Mortality and Survival by site for 14 regions of the world. Global Programme on Evidence for Health Policy Discussion Paper No. 13, http://www.who.int/entity/healthinfo/paper13.pdf, World Health Organization, 2001.

59. C Michel, PY Cresson, L Dubois, M Chive, and J Pribetich. Design and modeling of microstrip-microslot applicators with several patches and apertures for microwave hyperthermia. *Micr Opt Tech Lett*, 14:121–126, 1997.

60. RR Million and NJ Cassisi. *Management of head and neck cancer: a multidisciplinary approach.* JB Lippincott, New York, 1994.

61. TB Möller and E Reif. *Pocket atlas of cross-sectional anatomy: CT and MRI.*, volume Volume 1: Head, Neck, Spine and Joints. Georg Thieme Verlag Stuttgart, New York, 1994.

62. G Mur. Absorbing boundary conditions for the finite-difference approximation of the time-domain electromagnetic field equations. *IEEE Trans Electromag Compat*, 23:377–382, 1981.

63. J Nadobny, H Fähling, MJ Hagmann, PF Turner, W Wlodarczyk, JM Gellermann, P Deuflhard, and P Wust. Experimental and Numerical Investigation of Feed-Point Parameters in a 3-D Hyperthermia Applicator Using Different FDTD Models of Feed Networks. *IEEE Trans Biom Eng*, 49:1348–1359, 2002.

64. J Nadobny, W Wlodarczyk, L Westhoff, J Gellermann, B Rau, G Monich, and P Wust. Development and evaluation of a three-dimensional hyperthermia applicator with WAter-COated Antennas (WACOA). *Int J Hyperthermia*, 30: 2052–2064, 2003.

65. National Cancer Institute. Cancer Facts, Head and Neck Cancer: Questions and Answers. http://www.cancer.gov/cancertopics/factsheet/Sites-Types/head-and-neck. 2005.

66. Nederlandse Kanker Registratie. http://www.ikcnet.nl. 2003.

67. E Neufeld, T Samaras, N Chavannes, G Szekely, and N Kuster. An improved blood flow model to simulate EM induced hyperthermia. In *Abstracts of the 23nd Annual Meeting of the ESHO, Berlin, Germany (ESHO-06)*, May 2005.

68. P Nilsson. *Physics and technique of microwave-induced hyperthermia in the treatment of malignant tumours.* PhD thesis, Lund University, 1984.

69. The Nello Carrara Institute of Applied Physics of the Consiglio Nazionale delle Ricerche (IFAC-CNR). Florence. Italy. http://niremf.ifac.cnr.it/tissprop/. 1997-2002.

70. JR Oleson. If we cant define the quality, can we assure it? *J Rad Oncol Biol Phys*, 16:879, 1989.

71. J Overgaard. The current and potential role of hyperthermia in radiotherapy. *Int J Rad Oncol Biol Phys*, 16:535–549, 1998.

72. MM Paulides, SHJA Vossen, APM Zwamborn, and GC Van Rhoon. Theoretical investigation into the feasibility to deposit RF energy centrally in the head and neck region. *Int Rad Onc Biol Phys*, 63:634–642, 2005.

73. MM Paulides, DHM Wielheesen, J Van der Zee, and GC Van Rhoon. Assessment of the local SAR distortion by major anatomical structures in a cylindrical neck phantom. *Int J Hyperthermia*, 21:382–400, 2005.

74. MM Paulides, JF Bakker, and GC Van Rhoon. A head and neck hyperthermia applicator: experimental phantom verification and FDTD model. *Int J Rad Oncol Biol Phys*, 68:612–620, 2007.

75. MM Paulides, JF Bakker, APM Zwamborn, and GC Van Rhoon. A head and neck hyperthermia applicator: theoretical antenna array design. *Int J Hyperthermia*, 23:59 – 67, 2007.

76. MM Paulides, JF Bakker, N Chavannes, and GC Van Rhoon. A patch antenna design for a phased-array head and neck hyperthermia applicator. *IEEE Trans Biom Eng*, In press.

77. KD Paulsen, S Geimer, J Tang, and WE Boyse. Optimisation of pelvic heating rate distributions with electromagnetic phased arrays. *Int J Hyperthermia*, 15: 157–186, 1999.

78. HH Pennes. Analysis of tissue and arterial blood temperature in the resting human forearm. *J Appl Phys*, 1:93–122, 1948.

79. JP Pignon, J Bourhis, and Designe L Domenge, C. Chemotherapy added to locoregional treatment for head and neck squamous-cel carcinoma: three meta-analyses of updated individual data. *Lancet*, 355:949–955, 2000.

80. PMJ Rietveld, JB Van de Kamer, J Van der Zee, and et al. Influence of variations in position, form, and contents of semi-simple phantoms in the BSD-2000 Sigma-60 applicator on SAR distributions. In *Abstracts of the International*

Congress of Hyperthermic Oncology (ICHO-2000), page 145, Kyongju, South Korea, April 26th-29th 2000.

81. T Samaras, PJM Rietveld, and GC Van Rhoon. Effectiveness of FDTD in Predicting SAR Distributions from the Lucite Cone Applicator. *IEEE Trans Micr Theor Tech*, 48:2059–2063, 2000.

82. T Samaras, GC Van Rhoon, and JN Sahalos. Theoretical investigation of measurement procedures for the quality assurance of superficial hyperthermia applicators. *Int J Hyperthermia*, 18:416–425, 2002.

83. M Seebass, R Beck, J Gellerman, J Nadobny, and P Wust. Electromagnetic phased arrays for regional hyperthermia: Optimal frequency and antenna arrangement. *Int J Hyperthermia*, 17:321–336, 2001.

84. SEMCAD: the Simulation platform for EMC, Antenna Design and Dosimetry. Schmid & Partner Engineering AG (http://www.semcad.com).

85. M Serin, HS Erkal, and A Cakmak. Radiation therapy, cisplatin, and hyperthermia in combination in management of patients with recurrent carcinomas of the head and neck with meta-static cervical lymph nodes. *Int J Hyperthermia*, 15:371–381, 1999.

86. N Siauve, L Nicolas, C Vollaire, and C Marchal. Optimization of the sources in local hyperthermia using a combined finite element-genetic algorithm method. *Int J Hyperthermia*, 20:815–833, 2004.

87. PR Stauffer. Evolving technology for thermal therapy of cancer. *Int J Hyperthermia*, 21:731–744, 2005. Review.

88. A Stogryn. Equations for Calculating the Dielectric Constant of Saline Water (Correspondence). *IEEE Trans Micr Theor Tech*, 19:733–376, 1971.

89. A Taflove and SC Hagness. *Computational Electrodynamics: The Finite-Difference Time-Domain Method.* Artech House, 685 Canton Street, Norwood, MA 02062, 3rd edition, 2005. ISBN 1-580-53832-0.

90. A Trotti. Toxicity in head and neck cancer: a review of trends and issues. *Int J Rad Oncol Biol Phys*, 47:1–12, 2000.

91. P Turner. Apparatus for creating hyperthermia in tissue. Technical report, US Patent No. 4,589,423, 1986.

92. PF Turner and T Schaeffermeyer. BSD-2000 approach for deep local and regional hyperthermia. *Strahlentherapie und Oncologie*, 165:738–741, 1989.

93. HR Underwood, AF Peterson, and RL Magin. Electric-Field Distribution Near Rectangular Microstrip Radiators for Hyperthermia Heating: Theory Versus Experiment in Water. *IEEE Trans Biom Eng*, 39:146–153, 1992.

94. R Valdagni and M Amichetti. Report of long-term follow-up in a randomized trial comparing radiation therapy and radiation therapy plus hyperthermia to metastatic lymph nodes in stage IV head and neck patients. *Int J Rad Oncol Biol Phys*, 28:163–169, 1993.

95. R Valdagni, F-F Liu, and S Kapp. Important prognostic factors influencing outcome of combined radiation and hyperthermia. *Int J Rad Oncol Biol Phys*, 15:959–972, 1988.

96. JB Van de Kamer, N Van Wieringen, AAC De Leeuw, and JJW Lagendijk. The significance of accurate dielectric tissue data for hyperthermia treatment planning. *Int J Hyperthermia*, 17:123–142, 2001.

97. W Van den Bogaert, E Van Schueren, J-C Horiot, M De Vilhena, S Schraub, V Svoboda, G Arcangeli, M De Pauw, and M Van Glabbeke. The EORTC randomized trial on three fractions per day and misonidazole (trial no. 22811) in advanced head and neck cancer; long-term results and side effects. *Radiother Oncol*, 35:91–99, 1995.

98. J Van der Zee. Heating the patient: a promising approach? *Ann Onc*, 13: 1173–1184, 2002.

99. J Van der Zee, D Gonzalez Gonzalez, GC Van Rhoon, JD Van Dijk, WL Van Putten, and AA Hart. Comparison of radiotherapy alone with radiotherapy plus hyperthermia in locally advanced pelvic tumours: a prospective, randomised, multicentre trial. Dutch Deep Hyperthermia Group. *Lancet*, 355: 1119–1125, 2000.

100. JD Van Dijk, C Schneider, R Van Os, LE Blank, and DG Gonzalez. Results of deep body hyperthermia with large waveguide radiators. *Adv Exp Med Biol*, 267:315–319, 1990.

101. GMJ Van Leeuwen, JJW Lagendijk, BJAM Van Leersum, APM Zwamborn, SN Hornsleth, and ANTJ Kotte. Calculation of change in brain temperatures due to exposure to a mobile phone. *Phys Med Biol*, 44:2367–2379, 1999.

102. GC Van Rhoon. *Radiofrequency hyperthermia systems: experimental and clinical assessment of the feasibility of radiofrequency hyperthermia systems for loco-regional deep heating.* PhD thesis, Delft University, 1994.

103. GC Van Rhoon and P Wust. Introduction: Non-invasive thermometry for thermotherapy. *Int J Hyperthermia*, 21:489–495, 2006.

104. GC Van Rhoon, A Ameziane, WM Lee, DJ Van der Heuvel, HJ Klinkhamer, C Barendrecht, K Volenec, and PJ Rietveld. Accuracy of electrical field measurement using the flexible Schottky diode sheet at 433 MHz. *Int J Hyperthermia*, 19:134–144, 2003.

105. GC Van Rhoon, DJ Van Der Heuvel, A Ameziane, PJ Rietveld, K Volenec, and J Van Der Zee. Characterization of the SAR-distribution of the Sigma-60 applicator for regional hyperthermia using a Schottky diode sheet. *Int J Hyperthermia*, 19:642–654, 2003.

106. P Vaupel and M Höckel. Blood supply, oxygenation status and metabolic micromilieu of breast cancers: Characterization and therapeutic relevance (review). *Int J Oncol*, 17:869–879, 2000.

107. P Wust, M Seebas, J Nadobny, P Deuflhard, G Mönich, and R Felix. Simulation studies promote technological development of radiofrequency phased array hyperthermia. *Int J Hyperthermia*, 12:477–498, 1996.

108. P Wust, M Seebas, JM Gellerman, P Deuflhard, and J Nadobny. Antenna arrays in the SIGMA-eye applicator: Interactions and tranforming networks. *Med Phys*, 28:1793–1805, 2001.